2014

Annual Report
Jahresbericht

Remote Sensing
Technology Institute

Department
Atmospheric Processors

DLR

Contents

1. Foreword

When, one year ago, we introduced the then current annual report, we briefly discussed how one era – ERS and ENVISAT – slowly fades away while a new one – the atmospheric Sentinels – appear at our doorstep. Therefore we considered the year 2013 as a transition phase. It did not last long. Now, one year later, preparation for the first Sentinel, the Sentinel 5 Precursor mission with its ambitious schedule, meanwhile keeps us very busy. In addition, it is required that we already negotiate with our partners and the space agencies our prominent role for Sentinel 4, a novel atmospheric sounding approach in the timeframe 2019+ with the sensor being lifted up to and then operated from geostationary orbit. The future atmospheric mission portfolio of European and national agencies has even more candidates where we are either already selected as a prime partner or intend to become one. According to current launch schedules, there will be six new atmospheric missions within the next six years. Participating in these will be a real challenge. However, any agreed commitments must not jeopardize our current ones. These include two GOME-2 sensors on MetOp platforms delivering continuously new data but also still improving algorithms and processors for the ground segments of the past GOME and SCIAMACHY instruments.

For us, a particular highlight of 2014 was DLR's biennial open day. We consider it important because it permits to present to the interested public our recent achievements. This avoids that our work occurs in a sort of "ivory tower" environment. Particularly Earth related science, be it basic or application oriented, often has a direct impact on everyone's everyday life. At the DLR open day this was well demonstrated. A record-breaking stampede of visitors attended DLR's premises in Oberpfaffenhofen, including the Earth Observation Center where we informed about the atmosphere – from its tropospheric bottom up to its thermospheric top (see panel right) – in general and had our most spectacular topics on display. It was rather encouraging to get individual feedbacks from numerous visitors and to see that what we do is considered important and interesting.

In the same sense we hope that our annual report for the year 2014 is also received well by the readership. We thank our staff for their efforts and achievements in the past year and their contributions to this report.

Prof. Dr. Thomas Trautmann
Dr. Manfred Gottwald
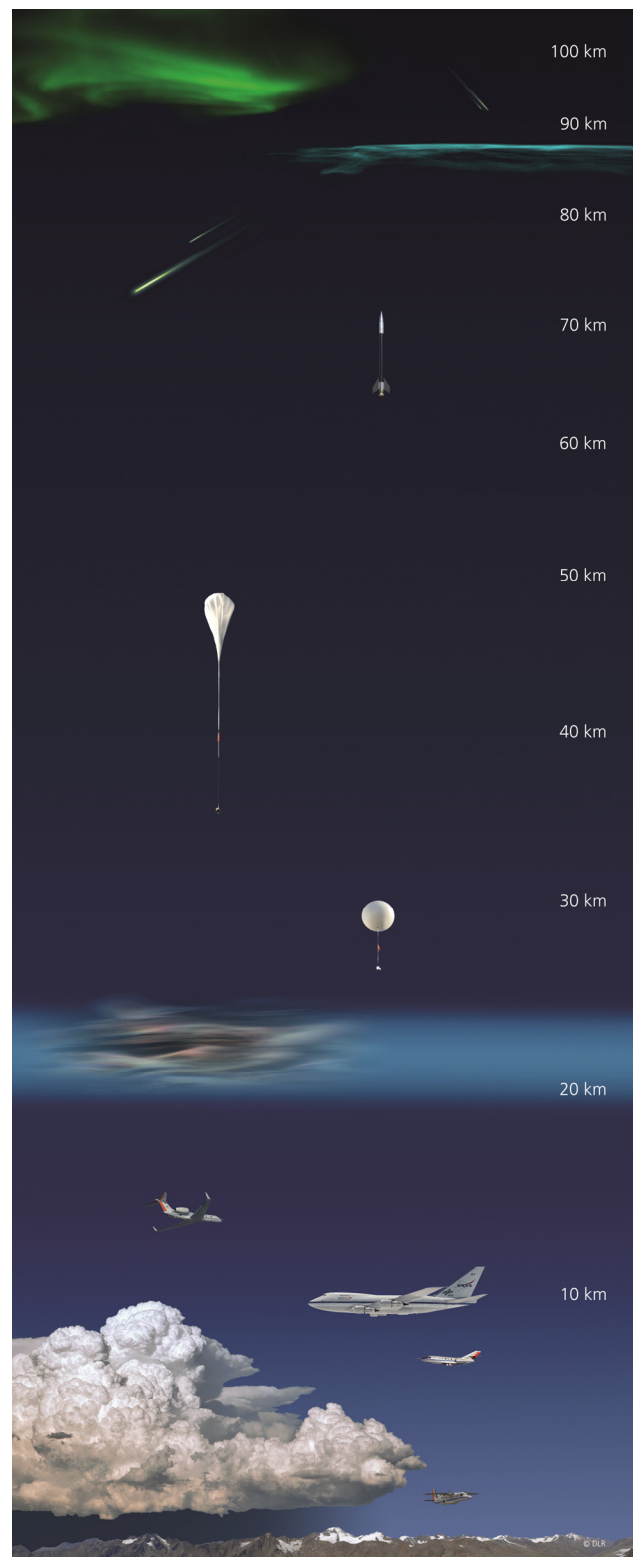
2. Atmospheric Remote Sensing – Missions and Sensors

2.1 SCIAMACHY Phase F Processor Development

G. Lichtenberg, B. Aberle, A. Doicu, S. Gimeno García, S. Hrechanyy, M. Meringer, F. Schreier, D. Scherbakov, S. Slijkhuis

The new data processors for the level 0-1b version 8 (instrument calibration) and the level 1b-2 version 6 (retrieval of atmospheric quantities) were finalised and underwent final tests in the previous year. The level 0-1b re-processing campaign was started in October, based on our newly coded level 0-1b processor. The corresponding level 2 reprocessing campaign is expected to start in early 2015. Apart from the quality checking and the delivery of the processors to ESA, the development of the next processor version was started by the agencies with a new 30 month contract.

Level 0-1 processing
Table 2-1 gives an overview of the new features of the level 0-1b version 8 processor and the planned updates for version 9.

Item	Description
Version 8	
Stray light channels 3-8	Extend matrix correction approach to channels 3-8.
Memory effect correction limb	Correct and improve the estimate of the previous signal for the first scan at a given tangent height.
PMD scaling nadir/limb	Improve scaling for low signal cases.
Hot pixel correction limb	Implement more robust hot pixel detection.
Polarization occultation off	Do not calculate polarization correction for occultation measurements. Since the available calibration data are invalid for this instrument mode, polarization values are no longer provided.
SAA check for etalon off	Normally no calibration values are calculated when measuring in the Southern Atlantic Anomaly. However, etalon calculation is not impacted by the SAA, since cosmics are filtered out before.
Dark selection for fit	Implement a selection option to specify which of the 5 dark states should be used for dark signal correction.
New key data polarization/radiance	New key data are used for calculation.
Scan mirror model	The scan mirror model from SRON is now used to correct degradation.
m-factor correction for pmd_int	Write the degradation corrected, integrated PMD values to the level 1b product.
Version 9 (planned)	
Update degradation correction	The correction will be updated using results from a re-analysis of on-ground calibration data.
Individual bad pixel mask	The bad pixel mask, which marks detector pixels that have a degraded performance, will now be based on thresholds for individual pixels instead of channel wide thresholds.
Improved dark correction	Using in-flight data of the whole mission, the dark correction will be improved.
Spectral calibration SWIR	Using a new method the spectral calibration of the SWIR channels 6-8 will be improved.
Polarization calibration	An improvement of the polarization correction will be investigated.
netCDF data format	The format of the level 1b data will be changed to the standard netCDF data format.

Table 2-1: Level 0-1b versions and updates.

Apart from the re-coding of the processor, the biggest change in level 1b processing was the introduction of the scan angle dependent degradation correction. In the previous version, the degradation was treated in level 2 under the assumption that the transmission loss does not depend on the incidence angles of the light on the scan mirrors of SCIAMACHY. Originally it was assumed that this first order correction would be sufficient for the level 2 retrievals. However, it turned out that the retrieval of aerosol parameters showed a systematic difference between ground pixels observed East and West from the central orbit track. In order to correct this so-called "scan angle dependence", SRON developed a model to calculate the decontamination layer effect on the transmission. This model was incorporated into the processor. Fig. 2-1 illustrates the effect of the degradation correction for solar measurements.
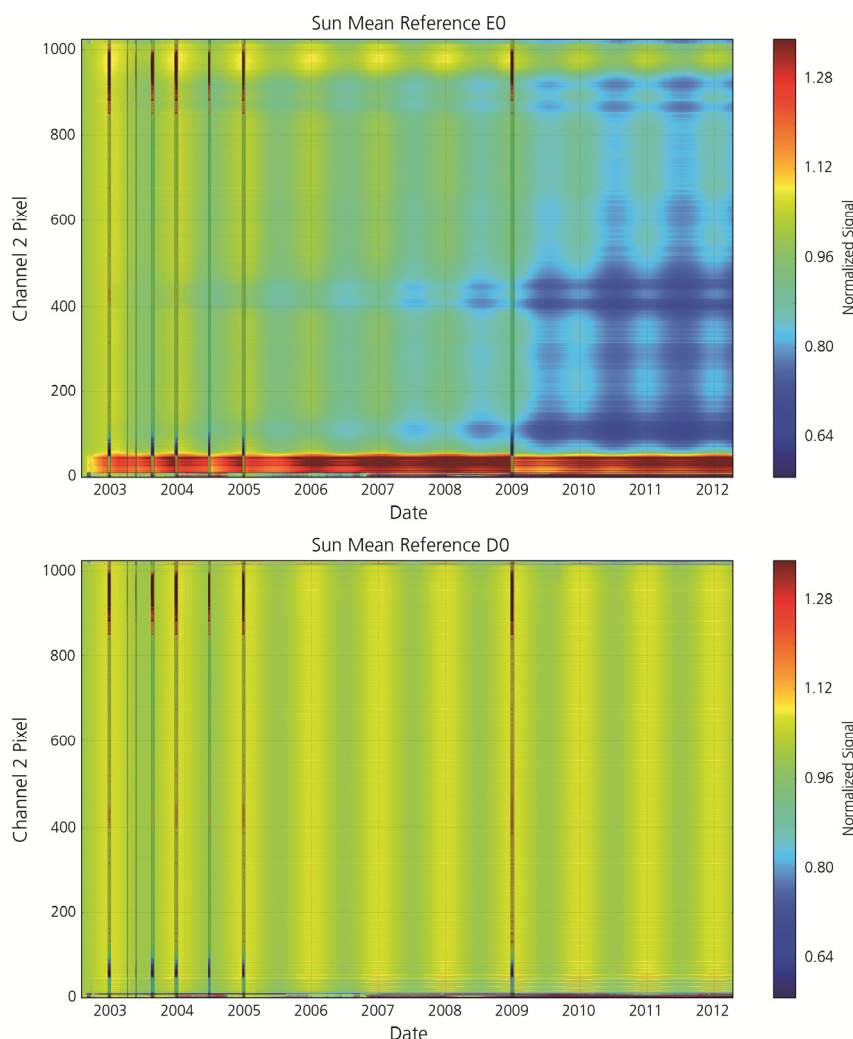
Fig. 2-1: Degradation correction in the new version of the level 0-1b processor. Shown is the signal normalized to the first measurement for each pixel (y-axis) in channel 2 over time (x-axis). Shaded regions mark decontaminations. The regular change over the year is caused by the varying sun distance. Top: Solar spectrum not corrected for degradation. Bottom: Fully calibrated, corrected spectrum.

Level 1b-2 processing

The new version 6 has four new products: Total columns of glyoxal (CHOCHO), formaldehyde (HCHO) and methane (CH_4). A first limb/nadir matching product, tropospheric NO_2 columns, has also been added to the processor (Fig. 2-2) The total column retrievals of sulphur dioxide (SO_2), chlorine dioxide (OClO), carbon monoxide (CO) and the limb retrievals of ozone (O_3) and cloud parameters have been further improved.

Although the phase F activities for the next processor versions concentrate mostly on level 1b improvements, there are also some enhancements planned for the level 2 processor as well, e.g., a new tropospheric bromine oxide (BrO) product and a better limb cloud identification. In addition, as for the

level 1b product, the level 2 product format will be changed to netCDF. This enables the user to use standard tools for reading and visualizing the data.

	(V 4)	V 5/5.02	V 6	V7 (planned)
Nadir				
O_3	improved	maintenance	maintenance	improved
NO_2	improved	maintenance	maintenance	maintenance
AAI	new algorithm	maintenance	improved	maintenance
CTH	maintenance	maintenance	maintenance	maintenance
CFR	maintenance	improved	improved	maintenance
SO_2	new (SCD)	improved (VCD)	improved	maintenance
BrO	new (SCD)	improved (VCD)	maintenance	maintenance
IO				TBD
OClO		new (SCD)	improved	maintenance
H_2O		new	maintenance	maintenance
CO		new	improved	maintenance
CHOCHO			new	maintenance
HCHO			new	maintenance
CH_4			new	maintenance
Limb				
O_3	improved	improved	improved	maintenance
NO_2	improved	maintenance	maintenance	maintenance
BrO		new	maintenance	maintenance
Cloud		new	improved	improved
Limb/Nadir				
Tropospheric NO_2			new	maintenance
Tropospheric BrO				new
Tropospheric O_3				TBD

Table 2-2: Product development for the last 3 versions and planned changes for the next version (TBD = *to be decided* based on maturity of algorithm). Version 4 was delivered, but never activated by ESA. Version 6 products will be delivered by ESA in 2015 after successful validation.
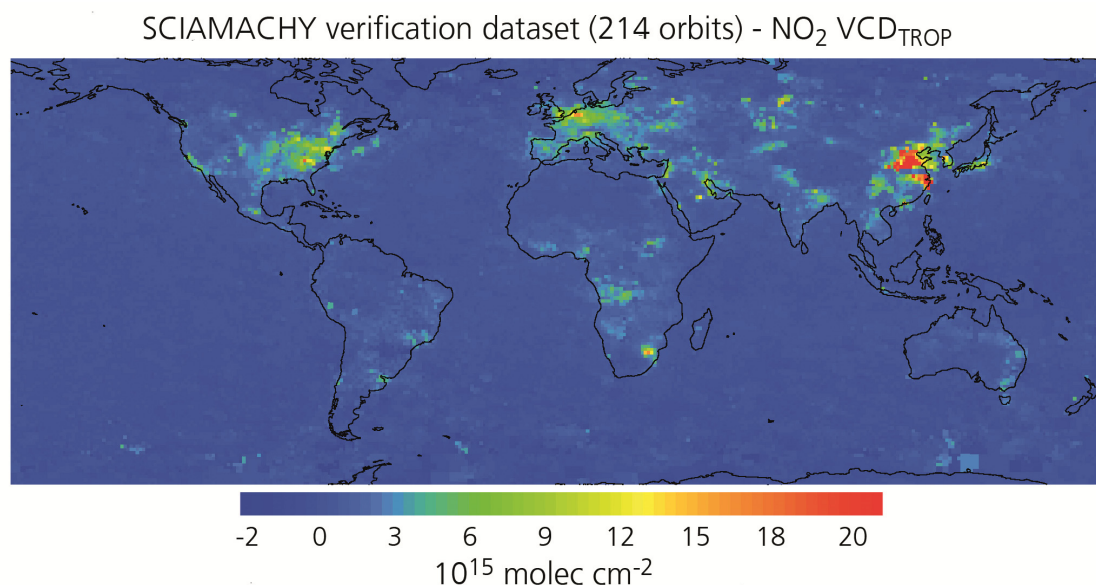

Fig. 2-2: The new tropospheric NO₂ product. Shown is the average over the verification data set of 214 orbits. Urban and industrial areas are clearly visible as significant NO₂ sources.

2.2 The SCIAMACHY Calibration Database

G. Lichtenberg, B. Aberle, A. Doicu, S. Gimeno García, S. Hrechanyy, M. Meringer, F. Schreier, D. Scherbakov, S. Slijkhuis

The level 0-1b processor for SCIAMACHY was completely re-coded during the last two years (see also chapter 2.1). This includes a complete revision of how the calibration data are handled. The modified processor is now embedded in a generic framework that is instrument agnostic and can also be used for sensors in future atmospheric sounding missions (see previous annual report for a description of its architecture).

The calibration data handling is complicated by the fact that usually calibration data are acquired at a much lower frequency than science data from the Earth's atmosphere. Additionally, individual calibration parameters are measured at different frequencies according to the calibration needs and instrumental capabilities. Calibration parameters captured at a certain point in time have to be applied to all Earth's atmosphere measurements falling between consecutive acquisition times of a given calibration parameter. Thus, all calibration data have to be saved together with timing information to be able to select the appropriate data for each measurement. In the previous processor versions this was achieved by handling simple files, i.e. calibration data were stored in several thousand files. This approach was error prone and did not allow to properly trace which calibration measurements were used for a particular Earth's atmosphere measurement. In the new processor architecture all calibration data are saved in a PostgreSQL database together with measurement time and orbit information. The measurement time of the used calibration is also transferred to the level 1b header and the user can immediately identify calibration measurements used for a given product.

The steps that are performed during the processing are (Fig. 2-3):

Step 1 – Preparation: The processor reads the configuration file and collects information about which calibration data are needed for which algorithm (not all data need all calibrations, e.g., solar measurements do not require polarization correction).

Step 2 – Writing: For each measurement in the level 0 file, the processor checks if it is a calibration measurement. If this is the case, the data are written to the database together with identifying information.

Step 3 – Application of calibration: If a given algorithm needs calibration data, it sends a request with a selection rule to the database. The database analyses the request and returns the calibration data according to the selection rule. Usually the most recent data are needed. These are identified by the measurement start time that is stored together with the calibration data in the database.

Since the database allows fast selection and reading of data, quality checks on the new calibration data can be quickly made and automatized. Before the delivery of the database, all entries are checked using the following tests:

- Does the database contain outdated entries, e.g., from previous (test) runs? This is checked by retrieving the creation times of all the entries.
- Are the values in the correct value range?
- Are the values updated with the correct frequency?

Fig. 2-4 illustrates an example, the fixed pattern noise (FPN) data, of the automatically generated plots that are used for checking the database content. The FPN is expected to be constant for the UV/VIS channels. For the SWIR channels changes are obvious that most likely can be attributed to detector degradation.

Apart from automatic checks needed for the operational data, the calibration data base also facilitates deeper analyses of the instrument performance. This can be used as a check for calibration algorithms or to develop improved calibration algorithms. An example for the check of the degradation correction is given in chapter 2-1 where sun mean references for the whole mission were retrieved from the database with and without degradation correction.
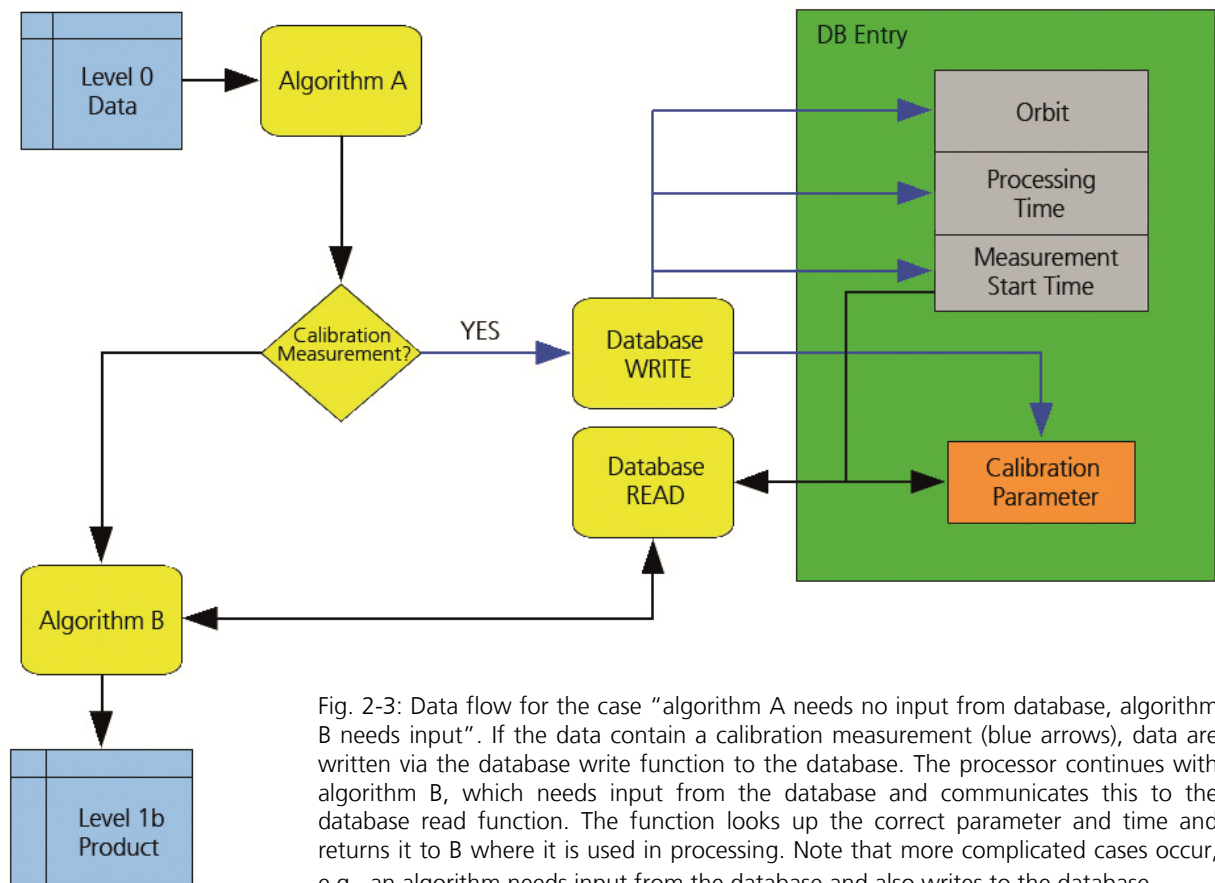
Fig. 2-3: Data flow for the case "algorithm A needs no input from database, algorithm B needs input". If the data contain a calibration measurement (blue arrows), data are written via the database write function to the database. The processor continues with algorithm B, which needs input from the database and communicates this to the database read function. The function looks up the correct parameter and time and returns it to B where it is used in processing. Note that more complicated cases occur, e.g., an algorithm needs input from the database and also writes to the database.
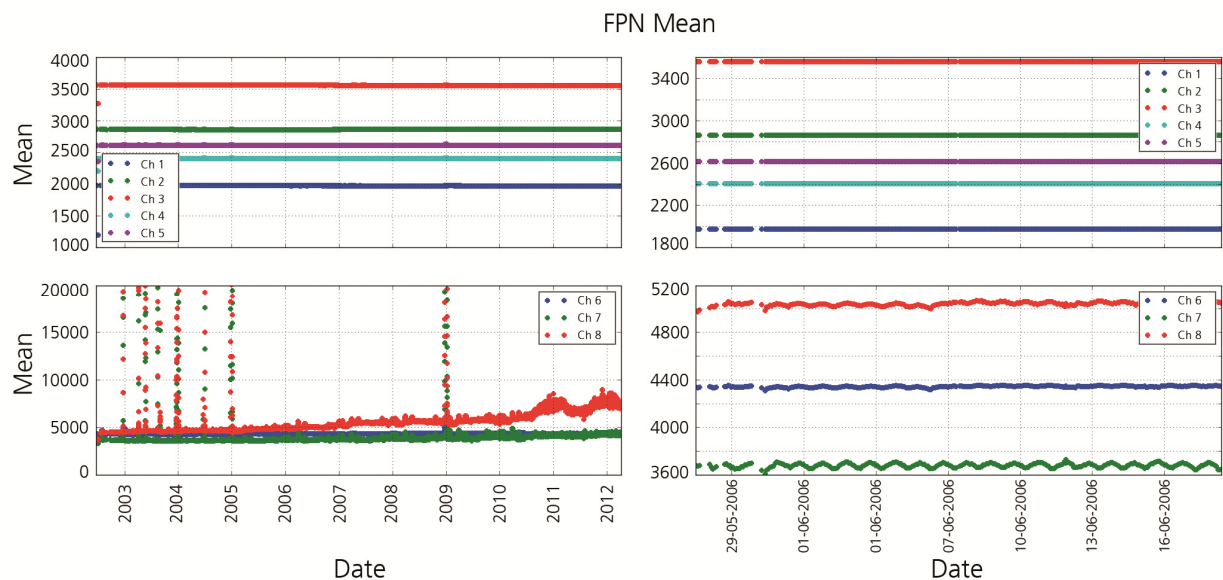
Fig. 2-4: Check of database entries. Plotted are channel averages. Outliers are caused by decontaminations. Top: UV/VIS channels. Bottom: SWIR channels. Left: Whole mission. Right: Zoom into two weeks in 2006 to check if the values change on smaller time scales.

2.3   SCIAMACHY Operations Support Phase F

M. Gottwald, E. Krieg (TwIG), K. Reissig (IBR), J. How (TwIG), S. Noël, K. Bramstedt, H. Bovensmann (all IUP-IFE)

With the end of the ENVISAT mission, caused by the fatal anomaly on 8 April 2012, also the highly successful SCIAMACHY mission, a joint German-Dutch-Belgian undertaking in the area of space-borne atmospheric sounding, had come to an end. SCIAMACHY had acquired measurement data between August 2002 and April 2012 for scientific purposes. This dataset will be subject to long-term data preservation. Since SCIAMACHY provided a wealth of operational measurement modes with the flexibility for modifying the instrument configuration whenever required, it is of paramount importance to also maintain the knowledge about instrument operations, i.e.

- mission planning
- instrument command & control
- instrument system performance

for the same duration. This ensures that interpretation of measurement data can always refer to the status of the sensor at the time of the data acquisitions. During the routine operations part of the in-orbit phase the SCIAMACHY Operations Support Team (SOST), formed by personnel from the German Remote Sensing Datacenter (DFD) – now Remote Sensing Technology Institute (IMF) – and the Institute of Environmental Physics / Institute of Remote Sensing (IUP-IFE) at the University of Bremen was responsible for ensuring safe instrument operations in accordance with the scientific requirements. This occurred in close cooperation with ESA.

In order to prepare all relevant instrument operations information for long-term storage, a phase F has been defined for SOST-DLR. It started in May 2014 and covers a period of two years. At the end of this phase it is intended to have

- improved specific aspects of instrument characterization
- consolidated the long-term instrument performance items (falling under SOST-DLR responsibility)
- archived operations information and telemetry
- archived s/w tools
- documented the archived items

All activities in the aforementioned areas have been harmonized with the needs of the phase F of the SCIAMACHY Quality Working Group (SQWG), which has the goal to prepare algorithms, processors and products for long-term data preservation.

Improvement of instrument characterization
For generating precise geolocation information, SCIAMACHY uses extra-mispointing angles which had been established by SOST in 2007. Particularly they allow to derive tangent height information with an accuracy of 200 m such that SCIAMACHY's limb measurements can be fully exploited. Various solar and lunar measurements, however, still indicate a small uncertainty in the pointing knowledge. In addition, the selected method for extracting the extra-mispointing angles could not investigate whether the mispointing is latitude dependent. Therefore, together with SQWG, we intend to tackle the ambitious goal to further improve on the pointing knowledge.

For the entire in-orbit phase SCIAMACHY observed moon occultations in the typically 1-week long monthly lunar windows whenever the moon was rising on the nightside of Earth. These measurements might provide additional information of the instrument's pointing characteristics. Since the moon rose between 10°S and 82°S geographic latitude, any latitude dependence could unveil. However, other than solar occultations, the analysis of lunar measurements is hampered by certain effects such as

- libration (causing different parts of the moon surface to be visible)
- variation of the distance Earth-moon
- variation of the lunar phase
- variation of the orientation of the lunar disk relative to the Earth's horizon

They all affect the amount of light the four quadrants of the Sun Follower detect when acquiring the moon in an occultation state, i.e. how both scanners were pointed to the moon's apparent center thus defining the instrument line-of-sight.

In a first step we have investigated how these effects varied over SCIAMACHY's in-orbit phase (Fig. 2-5 to 2-7). This will allow us to select the most suitable moon occultations, compare with 2D intensity maps of the lunar disk, e.g., as obtained by the USGS Robotic Lunar Observatory (ROLO) and, if possible, derive additional mispointing information.
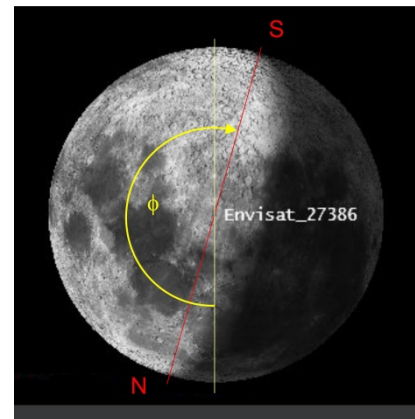
Fig. 2-5: Simulation of a moonrise as viewed by ENVISAT using the Agi Systems Toolkit (STK). The position angle φ is defined as indicated. It is used to describe the variable orientation of the lunar disk relative to the horizontally oriented Earth's limb.

Fig. 2-6: Moonrise as seen from SCIAMACHY for the start and stop of the April 2006 lunar window. The grey area at the bottom represents the Earth's horizon. Note the different moon phase and orientation of the lunar disk. The simulation has been performed with the Agi Systems Toolkit (STK).
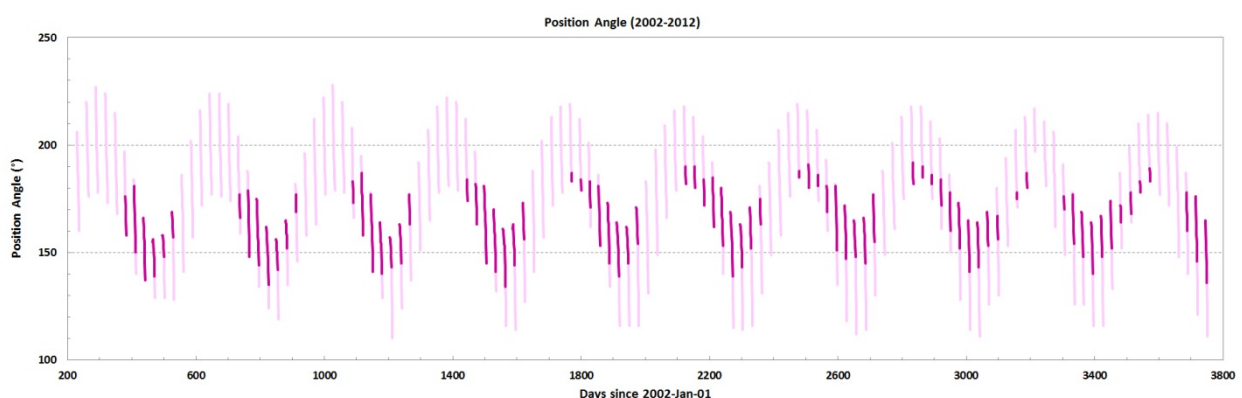
Fig. 2-7: Position angle φ between August 2002 and April 2012. The bold segments indicate SCIAMACHY's monthly lunar windows with moonrise occurring on the nightside of Earth.

Archiving operations information and telemetry

The original concept foresaw storing operations information and telemetry on individual servers for a certain time, including maintenance of the SOST webpages. However discussions in preparation of the phase F had shown that this approach could quickly separate measurement data and associated operations information. Therefore we proposed a new concept by using the new level 1b product

format which will be developed in the course of the SQWG phase F. This concept adds an operations section to the level 1b product. The operations section consist of

- reference orbit
- ENVISAT platform status (with relevance for SCIAMACHY)
- SCIAMACHY instrument status
- SCIAMACHY monitoring status
- SCIAMACHY instrument configuration (parameter tables)
- housekeeping (HK) telemetry

Since the level 1b products are orbit oriented, the operations information has to reflect the same structure. Thus it is required to collect all the items listed above in databases with absolute orbit numbers starting at 2204 (2 August 2002 – start of quasi-routine operations) and ending at 52868 (8 April 2012 – ENVISAT anomaly) as the main organizing parameter.

The first four bullets describe text information associated with specified keywords. It can be extracted from various tables on the SOST website. The 5th bullet deals with the configuration of the 13 measurement parameter tables. It has to be established for each orbit. We intend to use for each table the configuration from orbit 2204 as the starting point and develop from the corresponding Configurable Transfer Item (CTI) upload parameter files the sequence of different table contents as a function of absolute orbit number. Between orbits 2204 and 52868 a total of 3010 CTI uploads had occurred. HK telemetry files exist with a maximum duration of one orbital period. However it has turned out that the start of the files does not necessarily comply with the orbit start. Therefore individual orbits might be covered with more than a single file. The entire volume of the operations section does not exceed 4-5 MB, i.e. it only adds a small amount of data to the level 1b product with a total size of about 300 MB.

Currently we are assembling the operations information on an orbit-by-orbit basis for generating a comprehensive operations database. This will form the input for the operations section in the new level 1b product format.

3.   Atmospheric Remote Sensing – Methods

3.1   Operational O3M-SAF Trace Gas Column Products from GOME-2 on MetOp-A and -B

P. Valks, N. Hao, M. Grossi, P. Hedelt, M. Begoin, R. Lutz, S. Gimeno Garcia, D. Loyola

The operational GOME-2 trace gas column and cloud products from MetOp-A and MetOp-B are provided by us in the framework of EUMETSAT's Satellite Application Facility on Ozone and Atmospheric Chemistry Monitoring (O3M-SAF). The current GOME-2 trace gas products of the O3M-SAF include total ozone, total and tropospheric NO_2, SO_2, BrO, formaldehyde (HCHO) and water vapor. The O3M-SAF trace gas column products are generated operationally at DLR using the GOME Data Processor (GDP). In 2014, the new GDP version 4.8 has been developed (*Valks et al. 2014a*), including algorithm improvements for several trace gas column products (see below). The GOME-2 trace gas column data from MetOp-A and -B are used in the near realtime system of the Copernicus atmospheric service project MACC (Monitoring Atmospheric Composition and Climate). During the second Continuous Development and Operation Phase (CDOP-2) of the O3M-SAF (2012-2017), the focus lies on the development of new and better products, on new dissemination methods and on improved user services. New GOME-2 trace gas column products planned for the CDOP-2 are: total OClO, tropospheric ozone, BrO, glyoxal (CHOCHO) and climate products for NO_2 and water vapor.

Development of a new GDP version 4.8 for GOME-2 on MetOp-A and -B

A new GDP version 4.8 has been developed for the retrieval of the GOME-2 trace gas column products from MetOp-A and -B. The GDP 4.8 will be used for the operational near realtime (NRT) and off-line processing at DLR, as well as for the reprocessing of the GOME-2 trace gas column products for the complete MetOp-A and -B missions.

The GDP 4.8 includes improvements in the GOME-2 total ozone, SO_2, BrO, HCHO column algorithms, as well as in the retrieval of cloud properties using the OCRA and ROCINN algorithms. The algorithm developments for total ozone and SO_2 are described in chapters 3-2 and 3-3, while chapter 3-4 explains the improvements in the retrieval of the GOME-2 cloud fraction using the OCRA algorithm. Furthermore, new corrections for the GOME-2 instrument degradation in the O_2 A-band and a new inversion scheme (Tikhonov regularization) have been implemented in the ROCINN algorithm used for the retrieval of the cloud pressure and albedo.
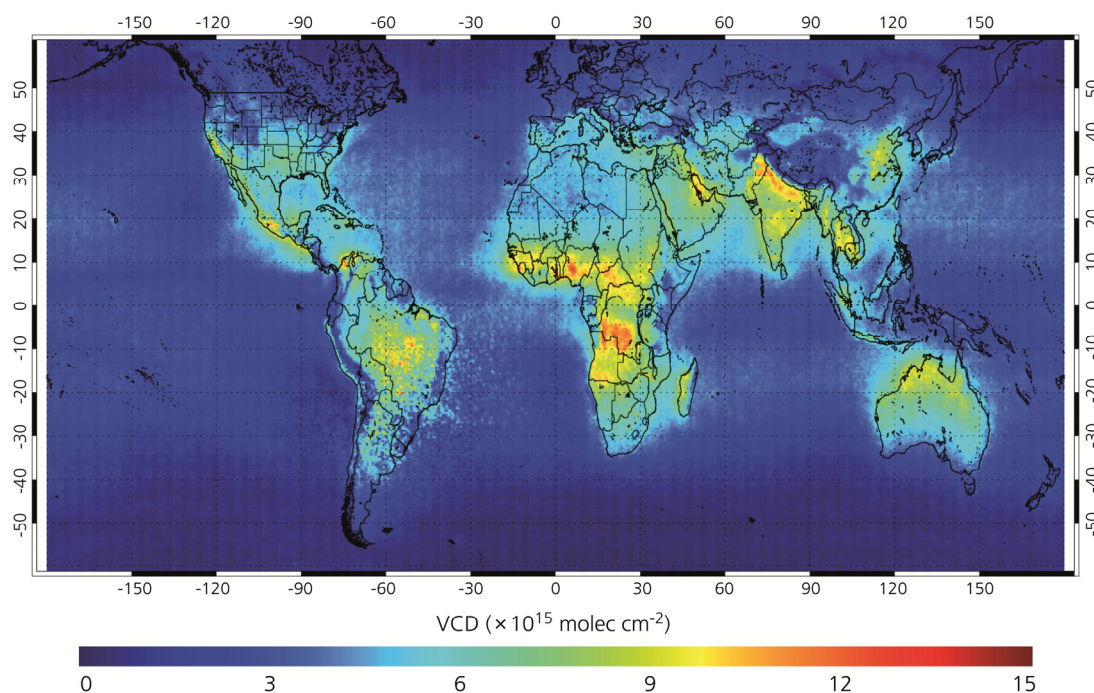

Fig. 3-1: Average tropospheric formaldehyde (HCHO) columns for 2013 as measured by GOME-2 on MetOp-B.

The HCHO column algorithm has been improved in the GDP 4.8 by implementing a two-step DOAS fit retrieval based on *De Smedt et al.* (*2012*), that effectively reduces the noise in the GOME-2 HCHO columns. Firstly, BrO slant columns are fitted in the large wavelength range 332-359 nm that includes five BrO absorption bands and minimizes the correlation with HCHO. Then HCHO columns are retrieved in the wavelength range 328.5-346 nm, using the BrO slant column values determined in the first step. Fig. 3-1 shows the average tropospheric HCHO columns from GOME-2 on MetOp-B for 2013, as retrieved with the GDP 4.8 algorithm. This figure displays the (sub)-tropical and mid-latitude regions with enhanced HCHO concentrations related to the release of hydrocarbons from forests, biomass burning, traffic and industrial emissions.

An Operational Readiness Review (ORR) for the GOME-2 trace gas column products based on the GDP 4.8 will be carried out in the first half of 2015.

GOME-2 tropospheric ozone product
The tropospheric ozone column (TOC) for the (sub)-tropical region is a new O3M-SAF product being developed within the CDOP-2. The retrieval algorithm for the tropical tropospheric ozone column is based on the convective-cloud-differential (CCD) method (*Valks et al. 2014b*), and uses both ozone column and cloud measurements from GOME-2 to derive a monthly mean TOC between 20°N and 20°S. Validation of the GOME-2 TOC with several tropical ozonesonde sites shows good agreement, with a high correlation between the GOME-2 and sonde measurements, and small biases within ~3 DU.
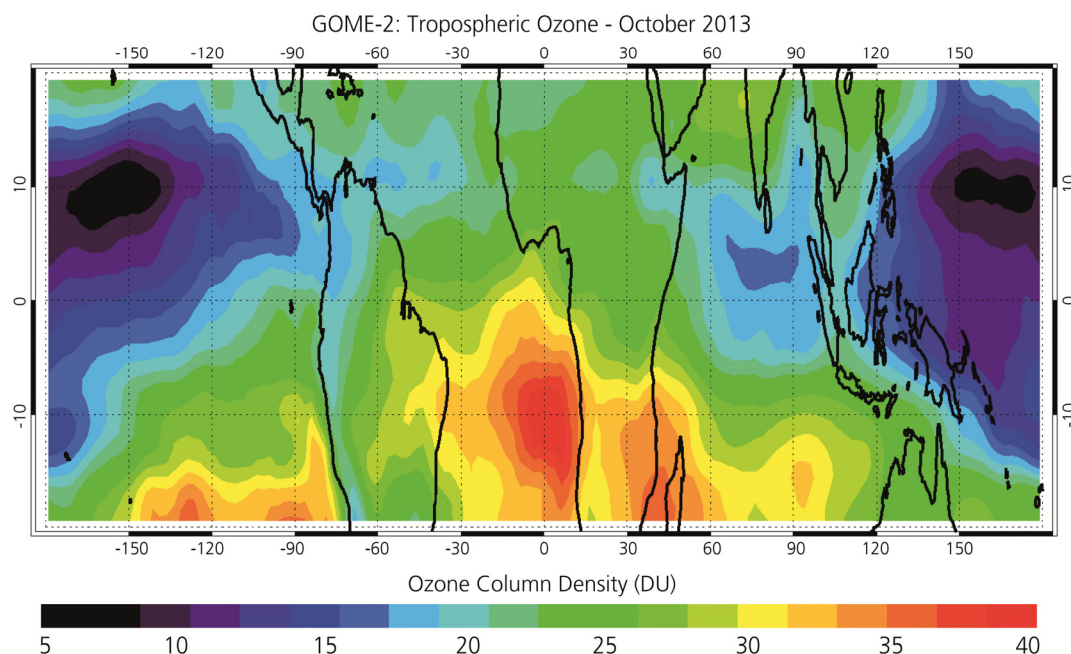
Fig. 3-2: Tropospheric ozone columns for October 2013, retrieved from GOME-2 data of both MetOp-A and MetOp-B.

Fig. 3-2 presents the tropospheric ozone columns for October 2013, as derived from GOME-2 data of MetOp-A and MetOp-B. Large tropospheric ozone columns are found over the southern Atlantic and southern Africa, while low tropospheric ozone concentrations are found over the tropical Pacific. The enhanced tropospheric ozone over the southern tropical Atlantic is mainly a result of dynamical processes, with permanent radiative subsidence over the quasi-stationary South Atlantic anticyclone area, allowing ozone production during downward transport. The Atlantic ozone maximum in September-November can be explained by a combination of lightning and soil NO_x sources, a maximum intensity of fires over Africa and South America, as well as a maximum in long-range transport. The low ozone values over the tropical Pacific can largely be attributed to convective lifting of low amounts of ozone clean air from the lower troposphere (including the pollution-free marine boundary) into the middle and upper troposphere.

The GOME-2 tropospheric ozone column product is expected to become operational in the first half of 2015.

References

De Smedt, I., Van Roozendael, M., Stavrakou, T., Müller, J.-F., Lerot, C., Theys, N., Valks, P., Hao, N., and van der A, R.: Improved retrieval of global tropospheric formaldehyde columns from GOME-2/MetOp-A addressing noise reduction and instrumental degradation issues. Atmos. Meas. Tech., 5, 2933-2949, DOI:10.5194/amt-5-2933-2012, 2012.

Valks, P., Loyola, D., Hao, N., Hedelt,P., Slijkhuis, S., Grossi, M., Begoin, M., Gimeno Garcia, S., Lutz, R.: Algorithm Theoretical Basis Document for GOME-2 Total Column Products of Ozone, Minor Trace Gases and Cloud Properties (GDP 4.8 for O3M-SAF OTO and NTO). DLR/GOME-2/ATBD/01, Iss./Rev.: 3/A, 2014a.

Valks, P., Hao,N., Gimeno Garcia,S., Loyola,D., Dameris,M., Jöckel, P., Delcloo, A.: Tropical tropospheric ozone column retrieval for GOME-2. Atmos. Meas. Tech. 7, 2513-2530, 2014b.

3.2   GOME-2 Total Ozone Columns from MetOp-A/MetOp-B and Assimilation in the MACC System

N. Hao, , P. Valks, D. Loyola, W. Zimmer, R.J.D. Spurr (RT Solutions), M.E. Koukouli, I. Zyrichidou, D.S. Balis (all Aristotle University of Thessaloniki), A. Inness (ECWMF), M. Van Roozendael, C. Lerot (both BIRA)

The Global Ozone Monitoring Experiment-2 (GOME-2) instruments were launched onboard the EUMETSAT MetOp-A (October 2006) and MetOp-B (September 2012), respectively. Operational total ozone columns are generated from the GOME-2 data at DLR's EOC using the UPAS (Universal Processor for UV/VIS Atmospheric Spectrometers) environment version 1.3.9, implementing the level-1-to-2 GDP 4.7 algorithm. On 15 July 2013, the operational dissemination of the GOME-2B near-real-time products including total ozone via EUMETCast started. GOME-2 level 2 near-real-time total column products from MetOp-A and MetOp-B are freely available in less than two hours after sensing on an operational 24/7 basis.

An important application of the GOME-2 total ozone record is its deployment within the MACC-II (Monitoring Atmospheric Composition and Climate - Interim Implementation) project (www.gmes-atmosphere.eu). MACC-II (and the predecessor project MACC, both in the following referred to as MACC) is the (pre)-operational atmospheric core service of the European Copernicus/GMES (Global Monitoring for Environment and Security) programme funded by the 7th Framework Programme of the European Union (*Hollingsworth et al. 2008*). The service combines a state-of-the-art transport and chemistry model with satellite data from various sensors to provide consistent analyses of 3-dimensional fields of atmospheric composition including ozone. The MACC system is run routinely every day to provide near-real time (NRT) 5-day forecasts of atmospheric composition and was used to produce a 10-year reanalysis of atmospheric composition data (*Inness et al. 2013*). GOME-2A and GOME-2B data have been assimilated in the MACC NRT analysis since October 2013 and May 2014.

Inter-comparison between GOME-2A and GOME-2B total ozone columns
A statistical analysis of GOME-2A and GOME-2B data has been performed with respect to time, latitude, and other parameters. It should be noted that all the data used for calculating the differences of total ozone column densities were collocated data. The difference of collocated ozone vertical column densities (based on daily gridded data) from GOME-2B and GOME-2A is calculated for seven different days during the period December 2012 to June 2013. A good agreement between GOME-2A and GOME-2B ozone columns is observed and the difference is within 1% for all latitudes. Fig. 3-3 presents the monthly mean time series of the ozone columns as a function of latitude. On average, GOME-2B produces 0.55±0.29% lower values than GOME-2A with larger differences (up to 1.5%) at high latitudes. Part of this difference is probably related to the different sampling of GOME-2A and GOME-2B over a single month (low statistics), and to partially corrected scan angle dependency.

Fig. 3-3: Time series of the zonally mean difference between GOME-2A and GOME-2B total ozone columns from December 2012 to November 2013.

We also studied the relative difference between the GOME-2A and GOME-2B total ozone columns as a function of total ozone columns and Sun Zenith Angle (SZA). The result shows that the differences do not depend on the total ozone column (GOME-2B underestimates total ozone by about 0.5% for all total column values). However, there is some SZA dependency in the bias between GOME-2A and GOME-2B total ozone. For low SZAs, the bias is small, but the difference between the GOME-2A and GOME-2B ozone columns increases with increasing SZA to about 0.5% at a SZA of ~40°, with no further SZA dependency for larger SZAs.
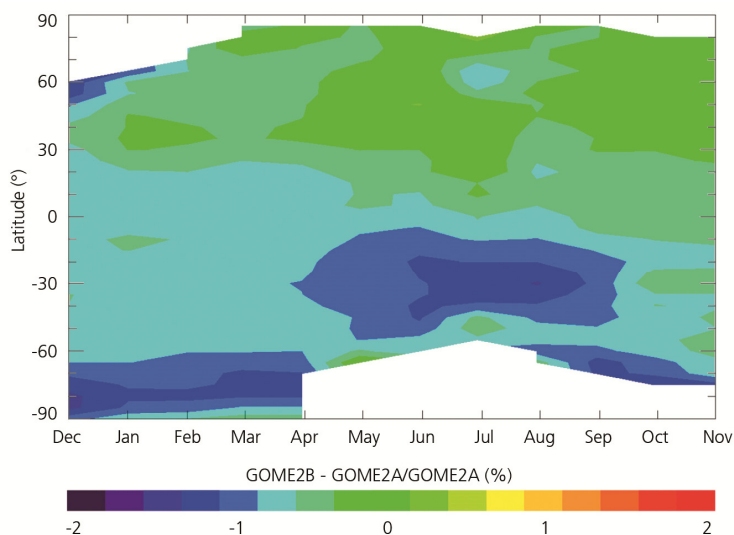
GOME-2A and GOME-2B measurements of the 2013 Antarctic ozone hole

Fig. 3-4 illustrates the total ozone column only from GOME-2A and GOME-2B, and GOME-2A & 2B for 18 October 2013, as retrieved with the GDP 4.7 algorithm described above. This figure demonstrates the capacity of the combined use of GOME-2A and GOME-2B instruments to provide homogeneous total ozone data with full daily global coverage, and shows important features such as the Antarctic ozone hole and characteristics of the polar vortex. The 2013 Antarctic ozone hole began to form in the middle of August, reaching a maximum of 24.0 million km^2 which is larger than the ozone holes in 2012 and 2010, but smaller than that for 2011, according to the WMO Antarctic Ozone Bulletin (to be found under www.wmo.int/pages/prog/arep/gaw/ozone).
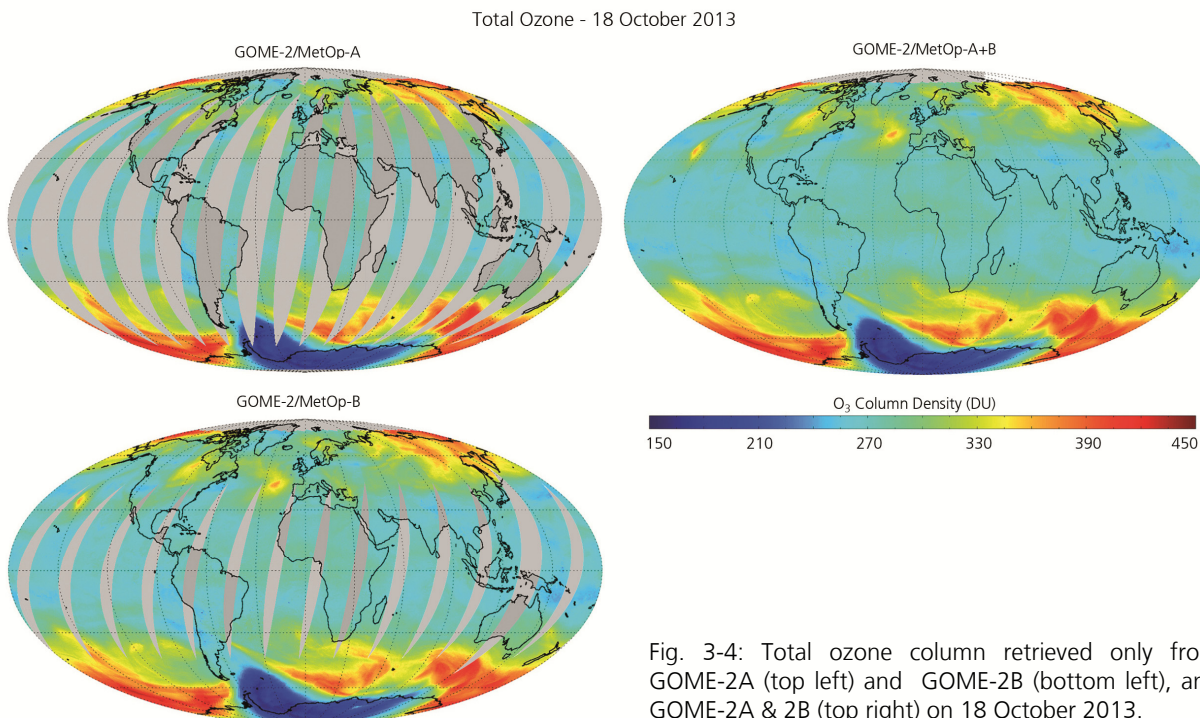
Fig. 3-4: Total ozone column retrieved only from GOME-2A (top left) and GOME-2B (bottom left), and GOME-2A & 2B (top right) on 18 October 2013.
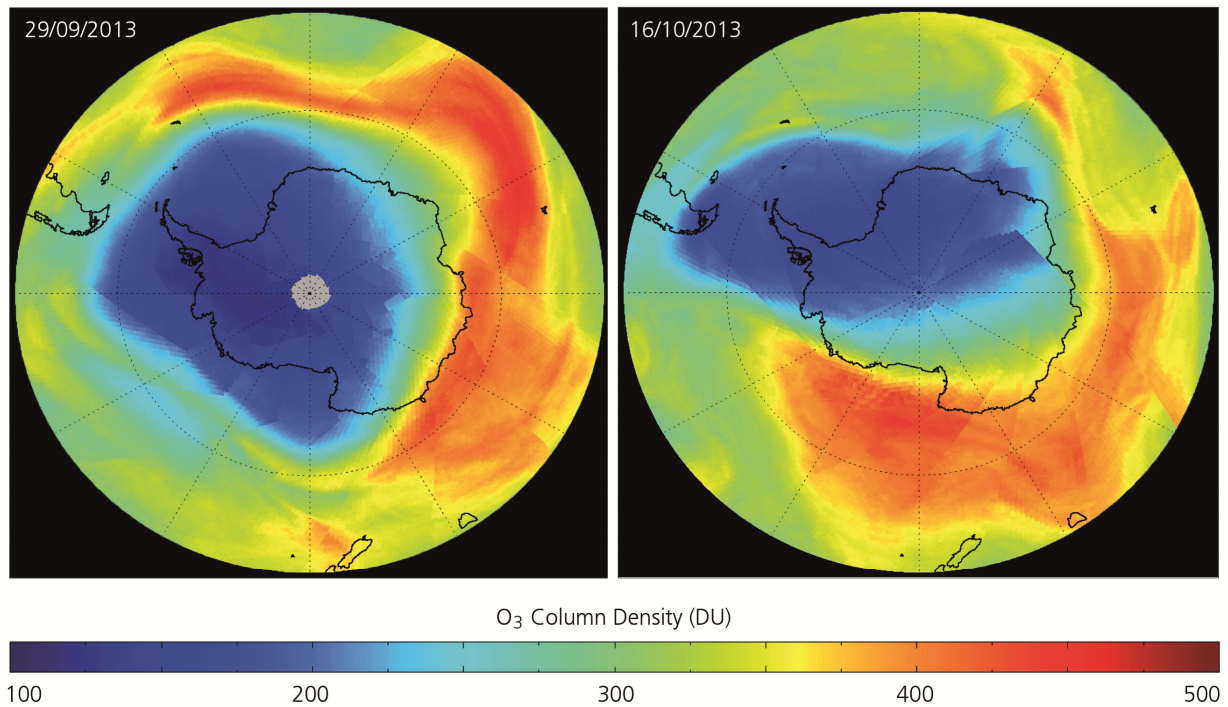
Fig. 3-5: Total ozone maps of the Antarctic ozone hole for two days based on data from GOME-2A and GOME-2B.

Fig. 3-5 presents the Antarctic ozone hole for 29 September and 16 October 2013 measured from GOME-2A and GOME-2B. The minimum total ozone columns measured by GOME-2 on 29 September reached around 116 DU. It is interesting to note that OMI/Aura also measured a minimum ozone of 116 DU on the same day. One can see from Fig. 3-5 that the edge of the ozone hole briefly touched the southern tip of the South America continent and affected inhabited places such as Ushuaia and Río Gallegos on 16 October 2013.

Initial ground-based validation

The publicly available Brewer and Dobson spectrophotometer archived total ozone column measurements used as ground-truth reside as part of the World Meteorological Organization (WMO)-Global Atmosphere Watch (GAW) network. Daily relative differences between ground-based total ozone measurements from Brewer and Dobson spectrophotometers, such as those archived at the World Ozone and Ultraviolet Radiation Data Centre (WOUDC) in Toronto, Canada (www.woudc.org), and GOME-2 are calculated using a 150 km search radius between the satellite centre-of-pixel and the geolocation of the ground-based station.
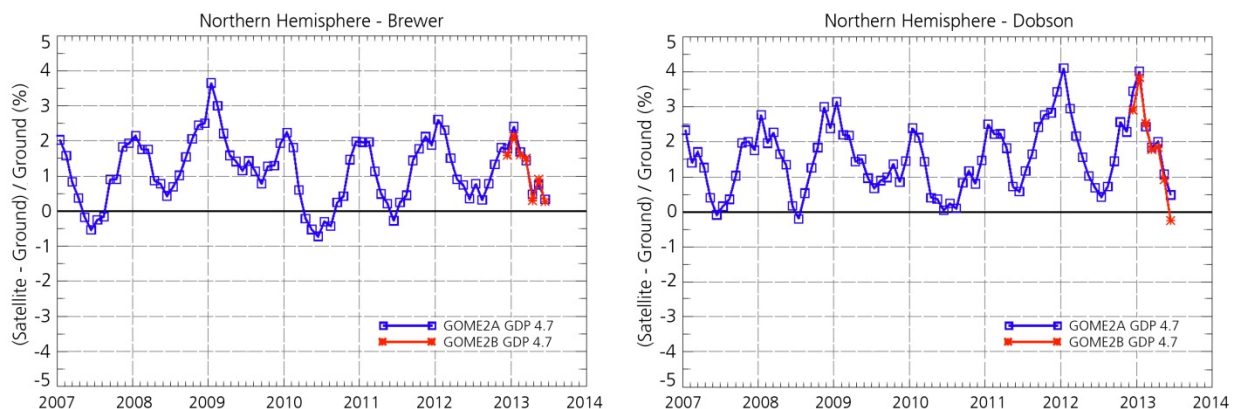
Fig. 3-6: Time series of the monthly mean percentage differences between GOME-2A GDP4.7 (blue line) and GOME-2B GDP4.7 (red line) against the Northern Hemisphere Brewer stations (left panel) and the Northern Hemisphere Dobson stations (right panel).
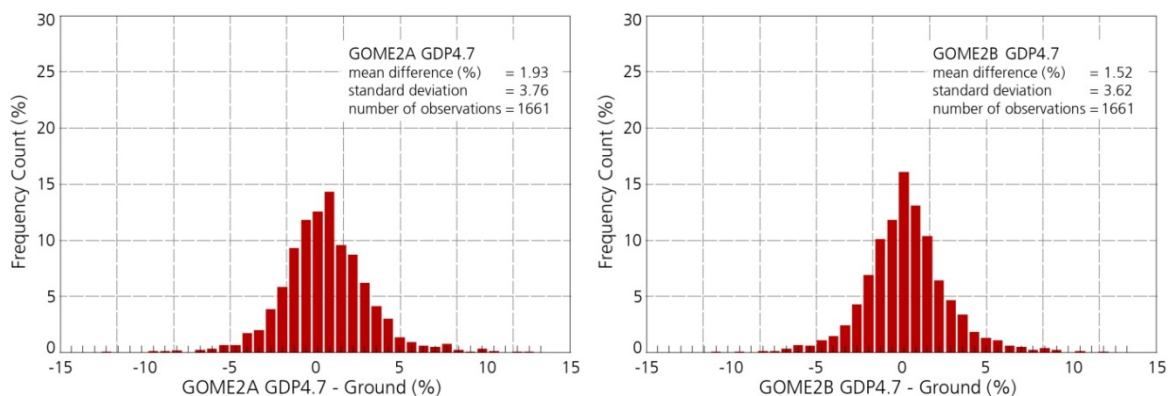
Fig. 3-7: Histogram representation of the daily relative differences between GOME-2A GDP 4.7 (left panel) and GOME-2B GDP 4.7 (right panel) against the global Dobson station network in the period December 2012 to June 2013.

In Fig. 3-6, the monthly mean relative differences for the Northern Hemisphere are presented for both the Brewer (left) and the Dobson (right) instruments. In order to show the stability and natural ozone variability during the GOME-2A mission, the time series begins in January 2007. Noteworthy in both panels, for both the GOME-2A and GOME-2B GDP 4.7 ozone record, is the positive offset between ground and satellite TOC, slightly larger for the Dobson case at 2±1% (right) than the Brewer case at 1±0.8% (left). Furthermore, a clear annual variability in the total ozone bias can be observed, which introduces a peak-to-peak difference of around 2-3% in relative terms. For the six common months of observations of the two GOME-2 instruments, the agreement is nearly identical. Some statistics of the differences between GOME-2A and GOME-2B using the Dobson network as background TOC truth are shown in the histogram of the daily percentage differences (Fig. 3-7). In the left panel, the GOME-2A differences present an almost Gaussian curve peaking around 1.9±3.8% with a small increased bump in the negative values. In the right panel, the GOME-2B differences are free from this bump and show a mean difference of 1.5±3.6% for the 1661 common points with the GOME-2A TOC dataset. These results are quite consistent with the 0.55±0.29% mean global difference between GOME-2A and GOME-2B discussed above. From the intercomparison exercise and the initial ground-based validation for the first six months of the GOME-2B life time, it can be concluded that the TOCs retrieved with the GDP4.7 algorithm for the two GOME-2 instruments are consistent. This is especially important for the tandem operation of the GOME-2A and GOME-2B instruments.

Application of GOME-2A total ozone columns in MACC

GOME-2 total ozone column data have been used in the MACC NRT system since 7 October 2013. Before this time the GOME-2 data were monitored passively and tested in offline assimilation experiments. "Monitoring" means that the data are included in the MACC system and first-guess and analysis departures of the data are calculated, but that the data are not used actively in the assimilation and have no impact on the ozone analysis. This procedure allows one to assess the quality of the data, the stability of the data provision, and to establish if there are biases between the data and the model, or between data from different instruments. If the quality of the monitored data is good and the data delivery is reliable, assimilation tests are performed in parallel to the operational MACC NRT analysis. If these assimilation tests are successful the data can be routinely assimilated in the MACC NRT analysis.

Fig. 3-8 shows this progression from monitoring to assimilation for GOME-2A TOC data. The top panel illustrates time series of first-guess and analysis departures for the period 1 February to 30 September 2013 from the MACC NRT analysis which included the GOME-2A TOC data passively at that time. The middle panel shows the same fields for an experiment in which the data were actively assimilated, and the bottom panel the number of data used in that experiment. In the top plot a change to smaller departures in July 2013 is obvious when the GOME-2 data processor was upgraded to version GDP4.7 and GOME-2A changed to half width swath mode. The version change led to decreased GOME-2 departures, because GDP4.7 data agree better with the MACC ozone field than GDP previous version. At the same time the number of observations that was monitored was reduced. This reduction was a result of a pre-screening that thins to 0.5° × 0.5° and is applied to the data in the MACC system to avoid oversampling and horizontally correlated observation errors. Because the data in half width swath mode are closer together, more data were now removed by the pre-screening. Apart from these

changes the GOME-2 departures were stable. The middle panel shows that when GOME-2 ozone data are assimilated departures and their standard deviation are reduced. The variational bias correction (*Dee 2004*, *Inness et al. 2013*) applied to the data (black curve) absorbs the changes seen in the passive monitoring plot and first-guess and analysis departures were stable as the data were assimilated successfully. After the version change in July 2013 the magnitude of the bias correction was reduced (to about -6 DU in the global mean) because the data now agreed better with the analysis. The magnitude of the bias correction after the version change is similar to that applied to OMI TOC data (not shown). The long term perspective of a succession of GOME-2 instruments made it desirable to include this instrument in the MACC NRT analysis.
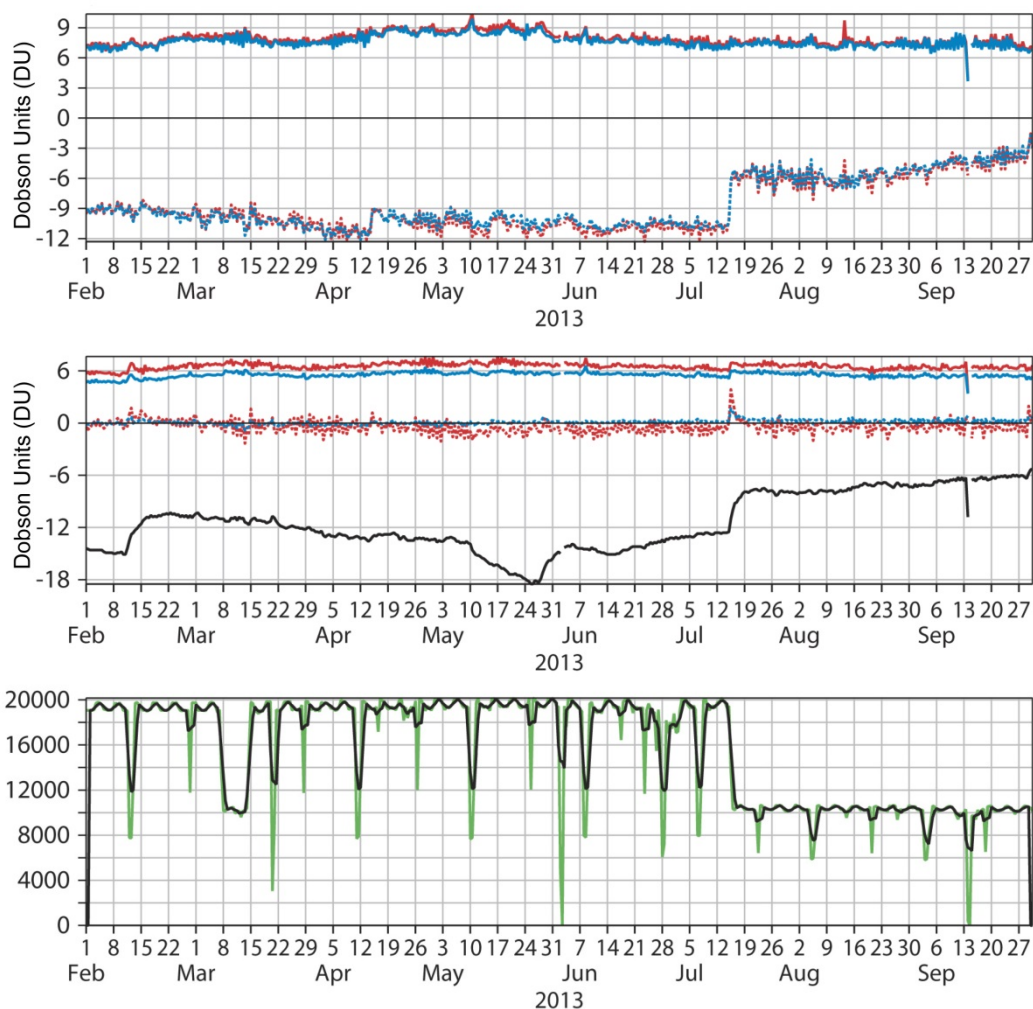
Fig. 3-8: Time series from 1 February to 30 September 2013 of first-guess (red) and analysis (blue) departures (dotted lines) and their standard deviations (solid lines) of GOME-2 total column ozone from the MACC NRT analysis which included the data passively, the middle plot shows the same for an experiment in which the GOME-2 TOC data were assimilated. The black line in the middle panel shows the bias correction applied to the data, and the bottom panel shows the number of observations used in this experiment.

References

Dee, D.P.: Variational bias correction of radiance data in the ECMWF system. In: Proceedings of the ECMWF workshop on assimilation of high spectral resolution sounders in NWP, Reading, UK, 28 June – 1 July 2004, 97-112, 2004.

Hollingsworth, A., Engelen, R. J., Textor, C. et al.: The GEMS Consortium: toward a monitoring and forecasting system for atmospheric composition: the GEMS project. Bull. Am. Meteorol. Soc., 89, 1147–1164, DOI:10.1175/2008BAMS2355.1, 2008.

Inness, A. et al.: The MACC reanalysis: an 8 yr data set of atmospheric composition. Atmos. Chem. Phys., 13, 4073-4109, DOI:10.5194/acp-13-4073-2013, 2013.

3.3 Improvement of Operational GOME-2 SO₂ Retrieval

P. Hedelt, P. Valks

The operational retrieval of atmospheric SO_2 is a challenging task because the spectral absorption bands of SO_2 partly overlap with O_3 absorption bands. Furthermore the possible source types are rather limited. They are either boundary-layer emissions from anthropogenic pollution or volcanic eruptions. Anthropogenic emissions mainly stem from coal-fired power plants or metal smelting. They occur in the boundary layer, i.e. they are localized below one kilometer above ground level. Thus cloud-free scenes or cases of cloud layers close to the surface are required for unambiguous detection. Volcanic emissions transport SO_2, depending on the type of eruption, to the lower troposphere (from degassing events), upper-troposphere (from moderate volcanic eruptions) and even to the lower-stratosphere (during explosive eruptions). At the time of the measurement the altitude of the SO_2 plume is mostly unknown. In addition, clouds play a dominant role for the detection of the SO_2 plume. Being located under or even within the cloud layer strongly hampers determination of the SO_2 column. The operational retrieval of SO_2 thus has to cope with the interferences of other trace gases and background noise. Two facts, however, facilitate the retrieval. Since the SO_2 sources are very rare and localized a background offset can easily be performed. Also the interference with O_3 in the operational fitting window between 315 and 326 nm can be reduced by taking into account the wavelength-dependency of the O_3 absorption (see *Pukíte et al. 2010*).

Presently the operational GOME-2 SO_2 product provides the end-users with three pre-selected total vertical SO_2 columns located at 2.5, 6 and 15 km altitude. These heights represent the above-mentioned emission scenarios. In 2014 a fourth vertical SO_2 column describing the anthropogenic emissions has been implemented into the operational processing algorithm UPAS. It is derived based on aircraft measurements from 2000 to 2005 (*Taubmann et al. 2006*), typical for most anthropogenic pollution scenarios in the U.S. and Europe. The modified SO_2 vertical column approach for GOME-2 now permits direct comparison with OMI SO_2 measurements, where this concept is already implemented.

During volcanic eruption events, satellite data is used to forecast the propagation of SO_2 several days ahead. The MACC project (Monitoring Atmospheric Composition and Climate) assimilates OMI satellite data to feed the forecast model using a single threshold criterion in order to select volcanic SO_2 vertical columns. So far this was not applicable to GOME-2 data because of the strong background noise sources. In 2014 a method was implemented in UPAS to automatically detect volcanic activity by identifying elevated SO_2 values from volcanic eruptions. It is based on the detection algorithm described in *Brenot et al. (2014)*, which is used by the SACS project (Support to Aviation Control Service) that aims at supporting the Volcanic Ash Advisory Centers (VAACs). The algorithm was adjusted to identify the entire volcanic SO_2 plume (see Fig. 3-9). This method not only takes into account different threshold values for the vertical SO_2 column depending on the proximity to known volcanoes, polluted areas of anthropogenic origin or even instrumental noise caused by the South Atlantic Anomaly, but also requires that a certain amount of neighboring pixels must fulfill these criteria. First tests by MACC on the Bardarbunga

GOME-2 (MetOp A&B): 20 September 2014
Bardarbunga (64.38°N, 17.32°W)

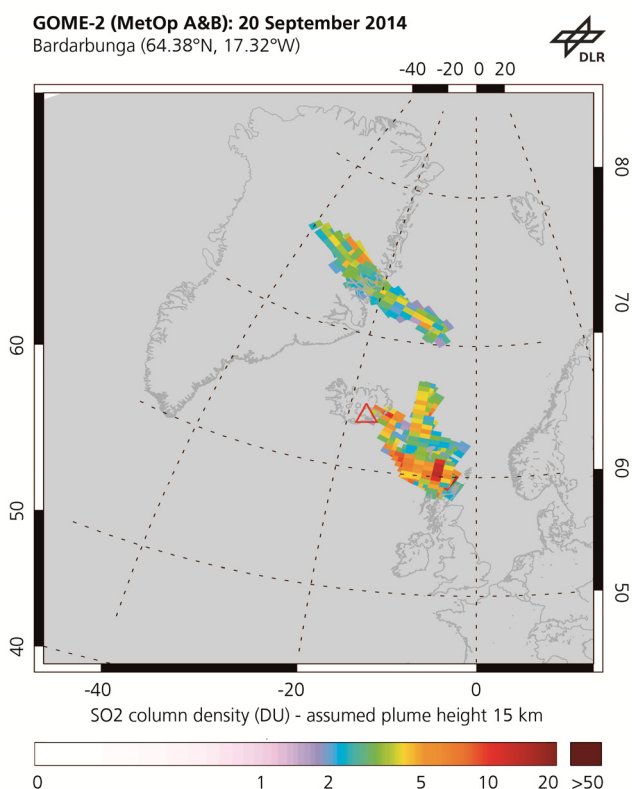SO2 column density (DU) - assumed plume height 15 km

Fig. 3-9: GOME-2 SO_2 measurement over Europe on 20 September 2014. Only data flagged by the newly implemented volcanic plume selection algorithm is plotted, clearly showing the location of the SO_2 clouds.

volcanic event (see chapter 4.2) have already shown the applicability of this new method and the improvement in the forecasts compared to the simple method when only OMI data are exploited. Fig. 3-9 illustrates Barbardunga's SO$_2$ plume detected by the volcanic activity algorithm, after assimilation by the MACC model (see Fig 3-10, colored dots in the left image) in order to forecast the distribution of SO$_2$ at 12:00 UTC. For the assimilation of OMI SO$_2$ data only a simple threshold of 5 DU is used, resulting in only one assimilated data point (see single dot in the center of the forecasted SO$_2$ cloud in the right image).
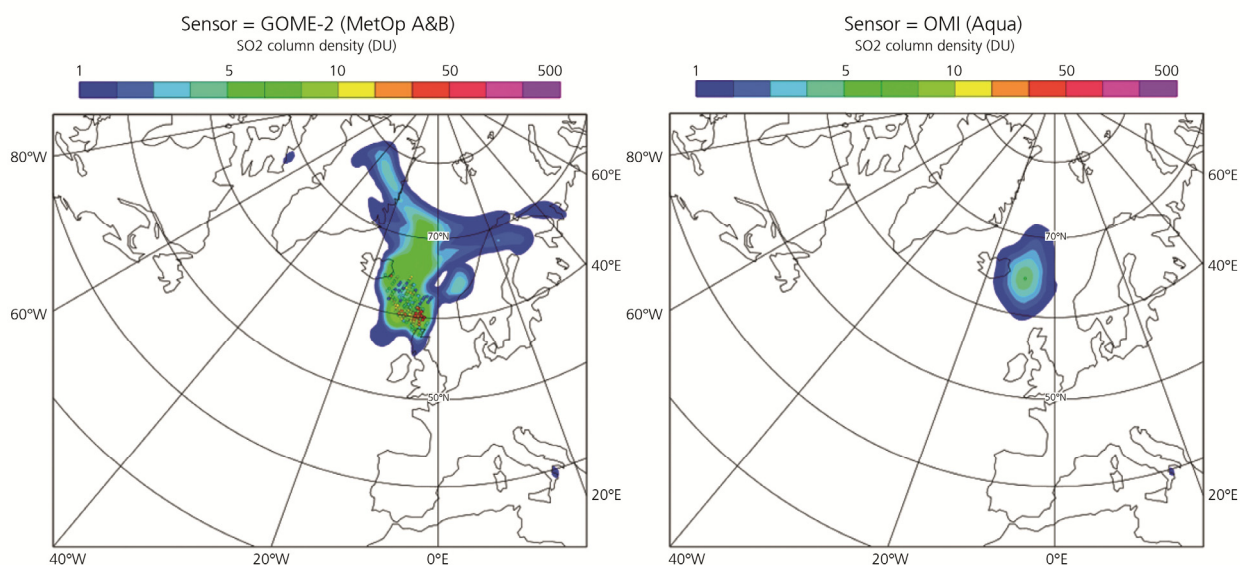
Fig. 3-10: MACC volcanic SO$_2$ forecast using assimilated GOME-2 data (left) and OMI data (right) on 20 September 2014. The colored dots show the assimilated data points from the two sensors (see also Fig. 3-9). Image: Antje Inness, MACC, ECMWF.

References

Brenot, H., Theys, N., Clarisse, L., van Geffen, J., van Gent, J., Van Roozendael, M., van der A, R., Hurtmans, D., Coheur, P.-F., Clerbaux, C., Valks, P., Hedelt, P., Prata, F., Rasson, O., Sievers, K., Zehner, C.: Support to Aviation Control Service (SACS): an online service for near-real-time satellite monitoring of volcanic plumes. Natural Hazards and Earth System Science, 14, 5, 2014, 1099-1123, 2014.

Puķīte, J., Kühl, S., Deutschmann, T., Platt, U., and Wagner, T.: Extending differential optical absorption spectroscopy for limb measurements in the UV. Atmos. Meas. Tech., 3, 631-653, 2010.

Taubman, B.F., Hains, J.C., Thompson, A.M., Marufu, L.T., Doddridge, B.G., Stehr, J.W., Piety, J.A., and Dickerson, R.R.: Aircraft vertical profiles of trace gas and aerosol pollution over the mid-Atlantic United States: Statistics and meteorological cluster analysis. J. Geophys. Res., 111, D10S07, 2006.

3.4   Cloud Fraction Determination for GOME-2A/B

R. Lutz, P. Valks, D. Loyola

Clouds can have a severe impact on trace gas retrievals. Therefore it is required to know whether clouds are present or not in a certain scene. The presence of clouds is usually expressed as *cloud fraction*. For the purpose of describing the cloudiness of the measured scenes, the Optical Cloud Recognition Algorithm (OCRA) had been developed (*Loyola 1998*). Contrary to cloud detection algorithms for sounders and imagers in the infrared wavelength range, OCRA is designed for sensors working in the visible part of the spectrum. For GOME-type sensors, it uses the information provided by the Polarization Measurement Devices (PMD), but its concept can be, and has already been, transferred to other sensors, e.g. OMI or the upcoming TROPOMI on Sentinel-5P.

For improving cloud detection for data from the GOME-2A/B instruments, we have updated and improved OCRA further. The basic idea behind OCRA is to split the measurement of a scene into contributions of clouds and a cloud-free background. The cloud-free background, i.e. the top-of-atmosphere reflectance in the absence of clouds, is calculated based on more than seven years of GOME-2A data. OCRA relies on the general assumption that clouds have a higher reflectivity than the surrounding ground in all optical wavelengths. In the optical part, the cloud reflectivity is almost wavelength-independent and therefore clouds appear "white" in normalized RGB color space. In the 7-year GOME-2A data set, for each predefined grid cell with a resolution of 0.2° × 0.2° in latitude and longitude, we search for the cases in the normalized RGB color space, which is furthest away from the "white" situation, i.e. the situation where we expect the least possible amount of cloud contamination. All these cloud-free situations of each grid cell are joined together to obtain global cloud-free maps for each month of the year. The comparison of a measured reflectance with the corresponding cloud-free reflectance can then be used to derive a radiometric cloud fraction for just that scene. With respect to earlier versions, OCRA now also includes degradation corrections for the reflectances as well as corrections for dependencies addressing the viewing zenith angle, latitudes and seasons.
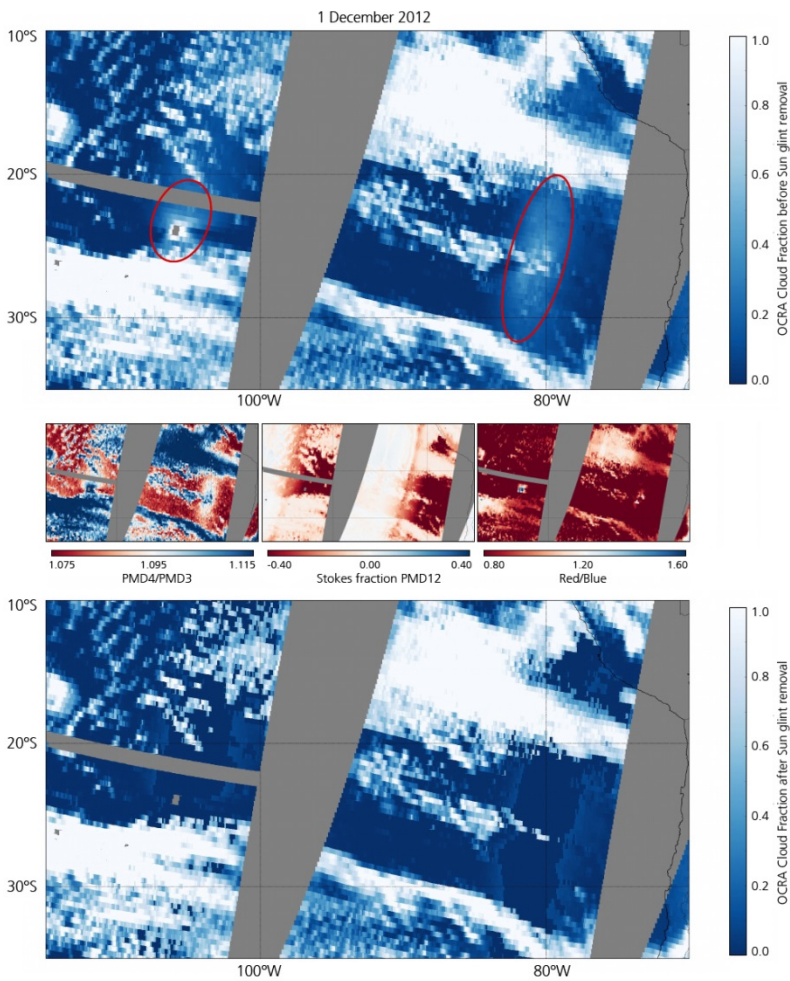
Fig. 3-11: Cloud fraction before Sun glint removal with the glint highlighted by the ellipses (top), properties to discriminate Sun glint from the clouds (middle) and cloud fraction after Sun glint removal (bottom).

Another feature which has to be dealt with is the *Sun glint*. Sun glint is the direct reflection of the Sun beam off the ocean surface into the detector and can only occur under certain geometrical conditions (interplay of solar- and satellite zenith angles and relative azimuth angle) and over cloud-free water surface. Sun glint will cause an enhanced reflectance signal which might be misinterpreted by OCRA as

a cloud. An approach to identify and correct for Sun glint with OCRA is outlined in *Loyola et al.* (*2011*). We extended the Sun glint identification and removal within the OCRA algorithm by incorporating several distinction criteria such as color indices, i.e. color ratios in different wavelength bands, and the Stokes fraction. These properties, in concert with carefully determined empirical thresholds help to distinguish if a signal determined by OCRA as a "cloud" is indeed due to a real cloud or if it is just mimicked as cloud due to the presence of Sun glint. Fig. 3-11 illustrates a scene where Sun glint is present (top) and OCRA's ability to identify this scene (middle) and to remove it without altering the real cloud fraction (bottom).

References

Loyola, D.: A new cloud recognition algorithm for optical sensors. Geoscience and Remote Sensing Symposium Proceedings, IGARSS '98, 1998 IEEE International, 2, 572-574, 1998.

Loyola, D., Koukouli, M.E., Valks, P., Balis, D.S., Hao, N., Van Roozendael, M., Spurr, R.J.D., Zimmer, W., Kiemle, S., Lerot, C., Lambert, J.-C.: The GOME-2 total column ozone product: Retrieval algorithm and ground-based validation. J. Geophys. Res., 116, D07302, 2011.

3.5 Effects of Cloud Variability on TROPOMI Molecular and Cloud Property Products

S. Gimeno García, D. Loyola, F. Schreier, T. Trautmann, R. Heinze (Leibniz University Hannover),

In order to guarantee high signal-to-noise ratios, the design of spectrometers aboard spaceborne platforms is a tradeoff between spectral and spatial resolution. Since molecular absorption is highly spectrally dependent, atmospheric composition instruments favor spectral over spatial resolution. The TROPOMI instrument aboard Sentinel 5 Precursor (S5P) will have a spatial resolution of about 7×7 km^2 at nadir, which clearly outperforms the resolution of previous atmospheric missions (320×40 km^2 for GOME/ERS-2, $\sim 120 \times 30$ km^2 for SCIAMACHY/ENVISAT and 80×40 km^2 for GOME-2/Metop-A,B). However, inside a TROPOMI ground pixel it will still be very likely to find a considerable amount of unresolved variability, e.g. observations where convective broken clouds are present, or inhomogeneous surface coverage.

In the atmospheric gas retrieval community it is common practice to use one-dimensional (1D) radiative transfer (RT) models to interpret the radiances measured by space-borne spectrometers. These models do not account for the horizontal optical variability enclosed within the large spatial pixel, nor for the horizontal photon transport. However, in nature the interaction of solar light with the Earth atmosphere and surface occurs in a double three-dimensional (3D) manner: the medium properties have 3D variability and the light transport is also 3D. Since 1D RT models used in the atmospheric retrievals do not account for 3D effects, these unaccounted features will impact the modelled radiances and, consequently, the retrieved atmospheric products; the question is by how much.

We performed a sensitivity study of measured reflectivities as a function of the unresolved cloud variability. For this purpose, we simulated virtual measurements of a TROPOMI-like instrument in cloudy scenes at different spatial resolutions by means of the three-dimensional (3D) radiative transfer model MoCaRT (Monte Carlo Radiative Transfer; *Gimeno Garcia et al. 2012*). The reference inside-pixel cloud liquid water content (LWC) was provided by the PArallelized Large-Eddy-Simulation Model (PALM) at a spatial resolution of $10 \times 10 \times 10$ m^3 in a 6.4×6.4 km^2 horizontal domain (*Heinze et al. 2012, Riechelmann et al. 2012*). The Monte Carlo RT simulations were carried out at high spectral resolution and convolved with an instrumental response function according to the actual specifications of TROPOMI (*Veefkind et al. 2012*): a full width at half maximum FWHM of 0.38 nm at the O_2 A-band spectral window. The O_2 molecular cross sections were line-by-line calculated with the GARLIC code.

Fig. 3-12 shows spectra calculated at the spatial resolutions of 20×20m^2, 40×40m^2, 80×80m^2, 160×160m^2, 320×320m^2, 640×640m^2, 1280×1280m^2 and 6400×6400m^2. It can be noticed that when the cloud microphysical and optical properties are not fully resolved but averaged horizontally, the radiances get biased to higher values: the lower the horizontal resolution, the higher the radiances as a consequence of the concave tendency of the reflectance on optical thickness. Moreover, the effect of the horizontal resolution on the simulated spectra has also a spectral dependency, being larger in the

23

deep absorption regions (see lower row of Fig. 3-12). The spectral dependency is also affected by the solar illumination, which renders a possible parameterization of 3D effects even more challenging.

In a second step, we investigated the variability and 3D RT effects on the retrieved cloud products by ingesting the 3D simulated spectra (around the O_2 A-band) to the ROCINN (*Loyola et al. 2007*) cloud algorithm. Figure 3-13 illustrates the impact of the horizontal resolution (at which the cloud properties are defined in the RT model). During the inversion process an overall good convergence was found independently of spatial resolution. The retrieved cloud albedo increases for decreasing spatial resolution, since the LWC-averaged scenes are brighter. The retrieved cloud (top) height is well below the geometrical cloud top height (1890 m) and, for high solar inclination (SZA=60°), it is even below the cloud bottom height.
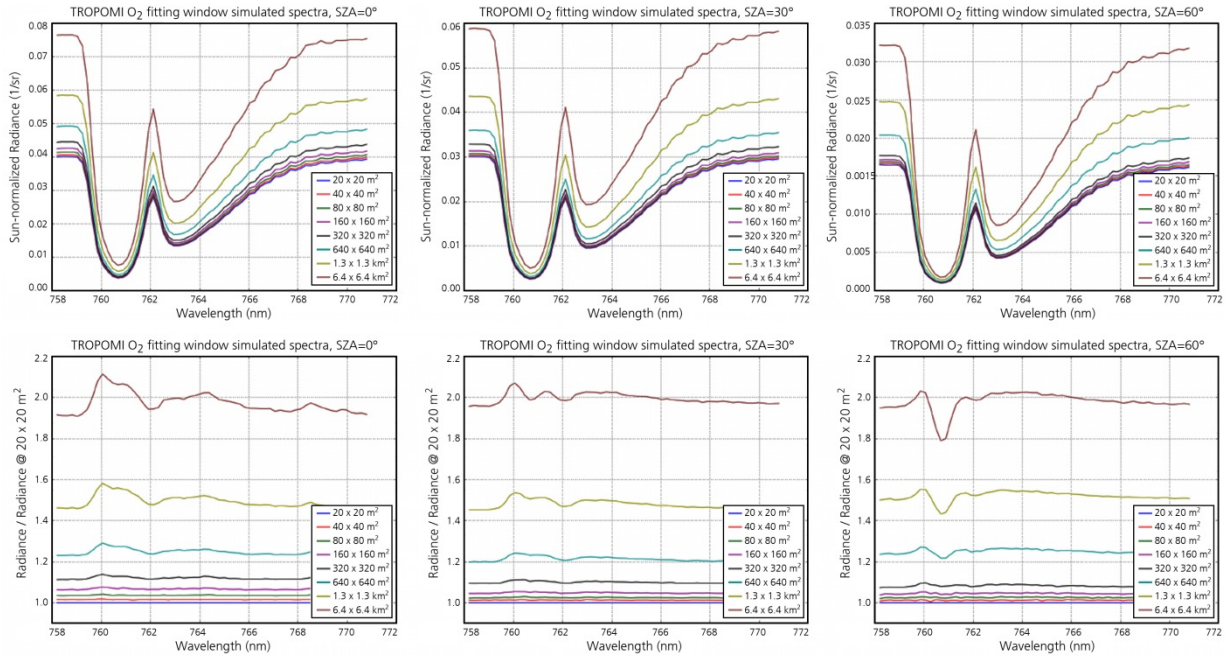
Fig. 3-12: MoCaRT simulated TROPOMI spectra. From left to right, the columns refer to sun zenith angles (SZA) of 0°, 30° and 60°. The different curves of the plots in the upper row represent the spectra calculated at different spatial resolutions. The lower row shows the ratio of the spectra at different spatial resolutions with respect to the spectra obtained at the highest resolution of the series, i.e. 20 × 20 m².
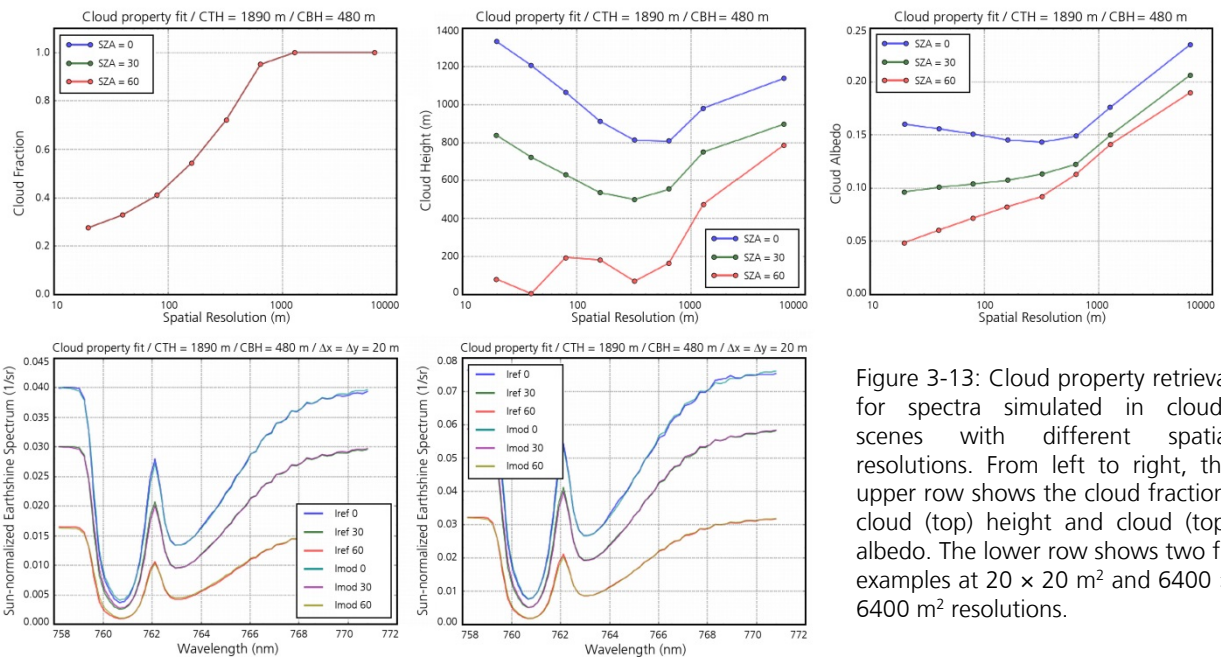
Figure 3-13: Cloud property retrieval for spectra simulated in cloudy scenes with different spatial resolutions. From left to right, the upper row shows the cloud fraction, cloud (top) height and cloud (top) albedo. The lower row shows two fit examples at 20 × 20 m² and 6400 × 6400 m² resolutions.

What can be concluded from these results is that photon path distributions contain important information to explain the results as shown in Fig. 3-12 and 3-13. The impact of 3D effects on column retrievals (O_3 and NO_2) is under further investigation.

References

Gimeno García, S., Trautmann, T., and Venema, V.: Reduction of radiation biases by incorporating the missing cloud variability via downscaling techniques: a study using the 3-D MoCaRT model. Atmos. Meas. Tech., 5, 2261-2276, 2012.

Heinze, R., Raasch, S., and Etling, D.: The structure of Kármán vortex streets in the atmospheric boundary layer derived from large eddy simulation. Meteorol. Z., 21, 221-237, 2012.

Loyola D., Thomas W., Livschitz Y., Ruppert T., Albert P., Hollmann. R.: Cloud properties derived from GOME/ERS-2 backscatter data for trace gas retrieval. IEEE Transactions on Geoscience and Remote Sensing, vol. 45, no. 9, 2747-2758, 2007.

Riechelmann, T., Noh, Y., and Raasch, S.: A new method for large-eddy simulations of clouds with Lagrangian droplets including the effects of turbulent collision. New J. Phys., 14, 065008, 2012.

Veefkind, P., Aben, I., Förster, H., et al.: TROPOMI on the ESA Sentinel-5 Precursor: A GMES mission for global observations of the atmospheric composition for climate, air quality and ozone layer applications. Remote Sensing of the Environment, 120, 70-83, DOI:10.1016/j.rse.2011.09.027, 2012.

3.6 Carbon Monoxide from SCIAMACHY Shortwave Infrared Nadir Observations: Impact of Retrieval Settings

D. Schmidt, F. Schreier, S. Gimeno García

Among the numerous parameters required by the forward model (essentially comprising atmospheric radiative transfer and an instrument model) and the inversion, the spectroscopic data characterizing the atmospheric species play a central role. A thorough knowledge of molecular spectroscopy is indispensable for modelling the radiative transfer through the atmosphere. In addition, the quality of the data used has a critical impact on the quality of the final retrieval product. Accordingly a considerable effort has been devoted to collecting, expanding and improving the data, and the most recent versions of the most widely used HITRAN and GEISA databases cover several million lines of some dozen molecules.

In contrast to the microwave, thermal infrared, or ultraviolet spectral range the shortwave and near infrared (SWIR, NIR) regions have attracted less attention for atmospheric spectroscopy, and comparatively few space missions carry sensors working in these regions. In contrast to its predecessor instrument GOME, SCIAMACHY has been equipped with three additional infrared channels for the retrieval of carbon monoxide (CO, channel 8, 4200-4415 cm^{-1}), methane (CH_4) and carbon dioxide (CO_2, both channel 6, 5640-10300 cm^{-1}). The 2.3 µm region is also used, along with the 4.7 µm region, by MOPITT for CO observations. The same region will be observed in the near future by Sentinel-5 Precursor (S5P) and GOSAT-2 scheduled for launch in 2016 and 2018, respectively.

In the framework of a recent Master Thesis the impact of retrieval settings on carbon monoxide retrieval using SCIAMACHY channel 8 near infrared spectra and the BIRRA software package has been studied. In addition to the spectroscopic data, both the fit of the wavenumber shift and the climatological a-priori information have been investigated, too.

BIRRA (Beer InfraRed Retrieval Algorithm, *Gimeno García et al. 2011*) performs a least squares fit of Earth's intensity (essentially transmission) to retrieve the molecular vertical column densities (VCD, equivalent to density scaling factors) along with some auxiliary parameters (reflectivity, etc.). BIRRA has been developed at DLR since about 2005 and its computational core modules have been integrated into the operational SCIAMACHY L1b-2 processor to retrieve carbon monoxide from channel 8 (2.3 µm) and methane from channel 6 (1.6 µm) nadir observations. To account for the special structure of the forward model, BIRRA uses a separable least squares algorithm. BIRRA evaluates derivatives w.r.t. unknowns of the state vector exactly using an implementation based on algorithmic differentiation. The

25

forward model of BIRRA is essentially based on GARLIC (Generic Atmospheric Radiation Line-by-line Infrared Code, *Schreier et al. 2014*).
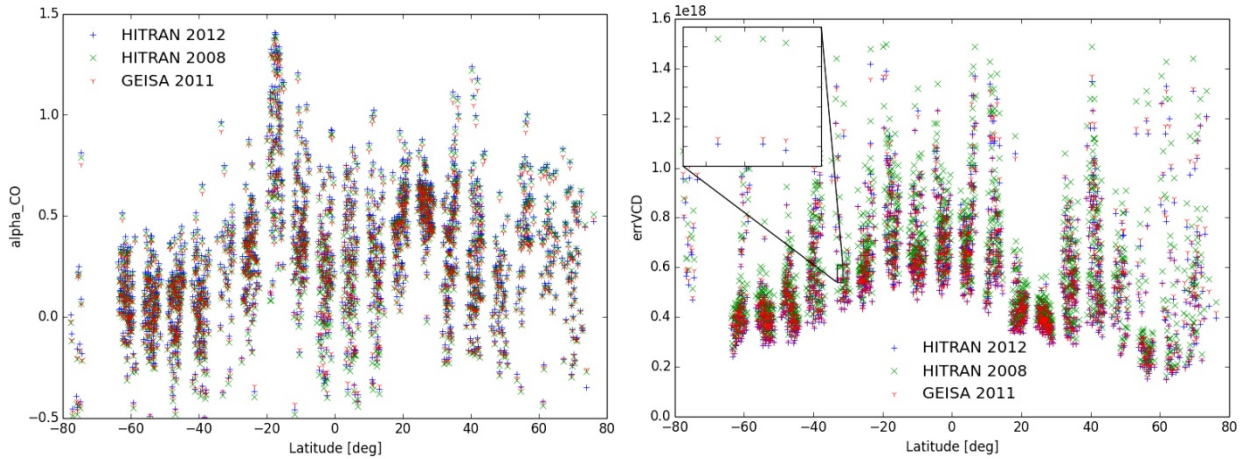
Fig. 3-14: CO scale factors (left) and errors of the VCD retrieval product (right) as a function of latitude for orbit 8663 (27 October 2003).
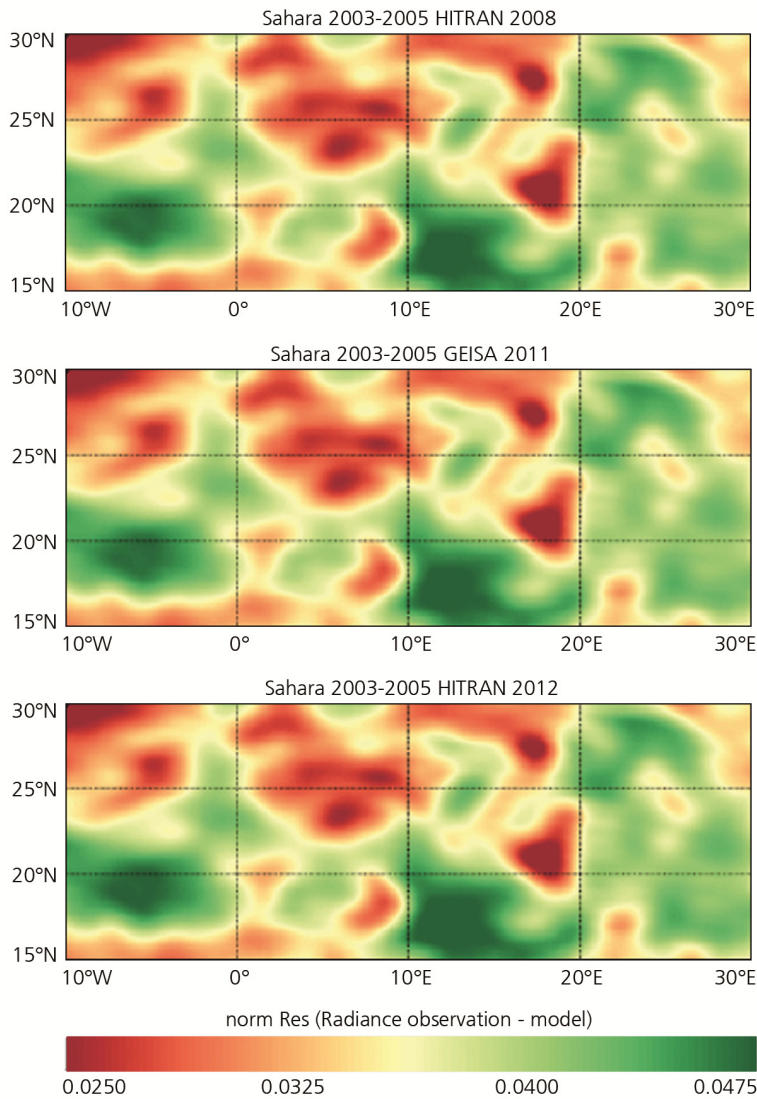
Fig. 3-15: Norm of the radiance residual vector (observed minus model radiance) versus latitude and longitude for the Sahara region 2003 - 2005.

BIRRA, like other SCIAMACHY SWIR retrievals, exploits the strongest lines of the CO R branch of the 2-0 band, i.e. our spectral window covers the interval 4283–4302 cm^{-1} comprising about 50 spectral pixels (depending on the DBPM). For the measurement vector y we use calibrated spectra normalized by a SCIAMACHY D0 Sun measured spectrum. Atmospheric data for pressure, temperature, and water vapor concentrations are taken from the NCEP reanalysis (providing four profiles per day with a 2.5° latitudinal and longitudinal resolution). Methane and carbon monoxide concentrations were taken from the AFGL dataset.

Retrievals using HITRAN 2008, HITRAN 2012, and GEISA 2009 have been performed for orbit 8663 (October 2003), characterized by a large land fraction (Russia, Arabian peninsula, and East Africa) to study any latitudinal influence. The residuals do not show big differences, and the number of "good" fits (converged, no outliers, etc.) is almost identical. Furthermore, the CO scaling factor and the error of the final VCD retrieval product are largely similar (see Fig. 3-14). Only a detailed analysis reveals slightly smaller errors of the scaling factors for HITRAN 2012.

For an analysis of the spatial and temporal evolution, observations (2003-2005) obtained over the Sahara, a region of relatively homogeneous terrain with high reflectivity and largely cloud-free, has been investigated. The residual norms (Fig. 3-15) are almost identical for all three databases, and their relative differences resemble the topography due to the correlation with surface albedo.

In summary, for the spectroscopic study – as well as for the wavenumber shift and climatological investigations (not discussed here) – the results are far from conclusive. The retrieved parameters are extremely similar for all tested retrieval settings and it is difficult to provide recommendations as to which settings yield a final product of improved quality. After careful consideration of the investigated quantities and the results, we arrived at the conclusion that other factors, such as level 1b calibration, and other retrieval settings in BIRRA are the predominant influence on the retrieval quality of the final CO product. However, the impact of retrieval settings for instruments with a better signal-to-noise ratio such as S5P remains to be examined.

References

Gimeno García, S., Schreier, F.,. Lichtenberg, G. and Slijkhuis, S.: Near infrared nadir retrieval of vertical column densities: methodology and application to SCIAMACHY. Atmos. Meas. Tech., 4, 2633-2657, 2011.

Schreier, F., Gimeno García, S., Hedelt, P., Hess, M., Mendrok, J., Vasquez, M. and Xu, J.: GARLIC – A general purpose atmospheric radiative transfer line-by-line infrared-microwave code: Implementation and evaluation. J. Quant. Spectrosc. & Radiat. Transfer, 137, 29-50, 2014.

3.7 A Novel Ozone Profile Shape Retrieval Algorithm for UV/VIS Sensors

O. Schüssler, D. Loyola

We study a novel algorithm for the retrieval of the ozone profile shape from UV/VIS nadir satellite measurements. The main idea of this method is to find a mapping between UV measurements and ozone profile shapes with the help of a machine learning technique. This would speed up the ozone profile shape retrieval.

In the first step we used the unsupervised clustering algorithm ISODATA (Iterative Self-Organizing Data Analysis Technique) to group ozone profiles into clusters according to their shapes and independent of other criteria. This way we determined a set of clusters, comprised of similar profiles shapes. For the TOMS v8 climatology (*McPeters et al. 2007*), the corresponding clusters with profiles are illustrated in Fig. 3-16 (left four columns).

Then, we selected a representative set of profiles in each cluster (see Fig. 3-16, right four columns), and used these ozone profiles, together with corresponding temperature profiles taken from a climatology, as input to the VLIDORT radiative transfer model (*Spurr 2008*). We performed simulations in the spectral range of 290-335 nm, for all feasible viewing geometries and surface parameters. This was the most time-consuming step, but it had to be done only once and off-line.

After this step was accomplished, we created a set of training examples, where each simulated measurement was labelled with the corresponding profile cluster. Finally we applied supervised machine learning algorithms for training a model for the mapping between UV measurements and ozone profile shapes.

In order to assess the generalizability of the trained model, we performed a validation using GOME-2 measurements, and compared the predicted profile shapes with the profiles retrieved from the same measurements by classical inversion algorithm. The resulting profile shapes for three validation cases can be seen in the Fig. 3-17.

It is obvious that predicted ozone profiles are very close to the retrieved ozone profiles. Therefore such predicted profiles can be used as a priori for the classical inversion algorithm, which reduces the number of iterations considerably.
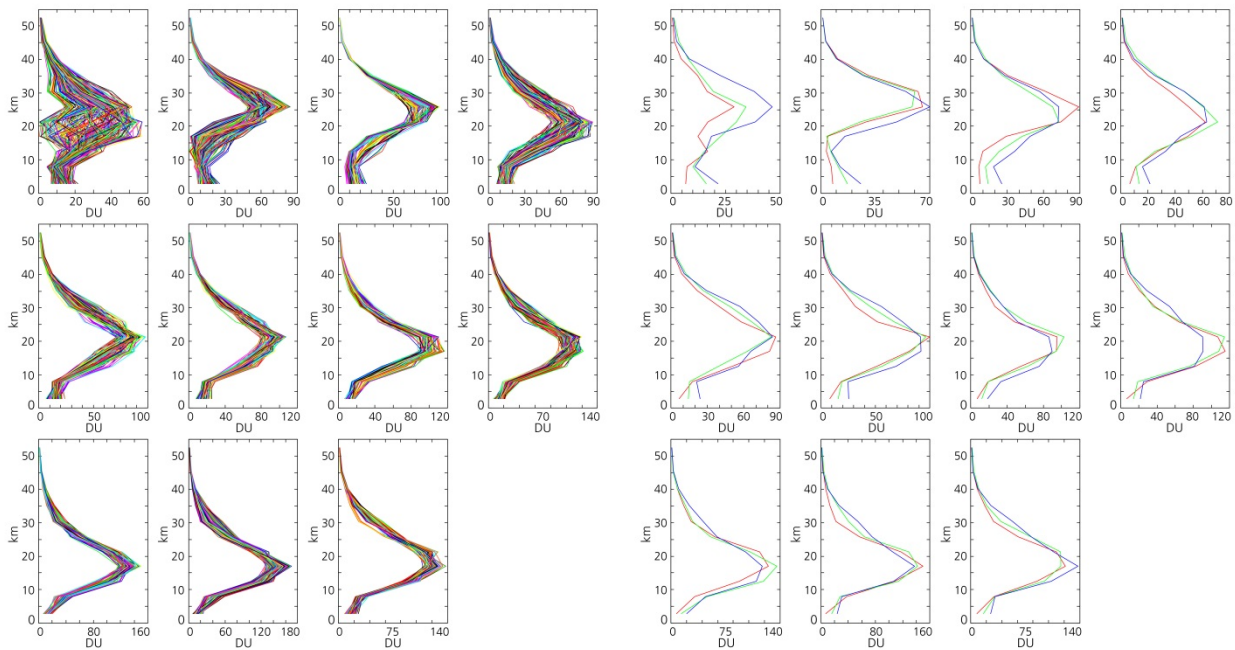
Fig. 3-16: Results of ISODATA clustering algorithm: 11 clusters (left four columns) and representative ozone profiles in each cluster, selected for further simulations (right four columns).
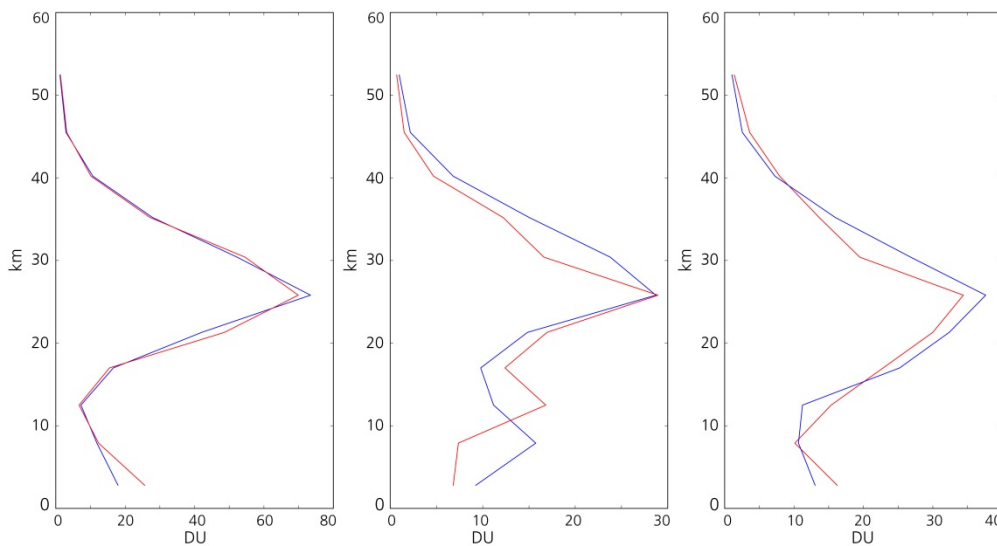
Fig. 3-17: Ozone profiles for three random cases from GOME-2 measurements on 16 October 2007: Predicted shapes (red) and shapes retrieved with classical inversion algorithm (blue).

References

McPeters, R.D., Labow, G.J., and J. A. Logan, J.A.: Ozone climatological profiles for satellite retrieval algorithms. J. Geophys. Res., 112, D05308, DOI:10.1029/2005JD006823, 2007.

Spurr, R.: LIDORT and VLIDORT: Linearized pseudo-spherical scalar and vector discrete ordinate radiative transfer models for use in remote sensing retrieval problems. In Light Scattering Reviews, 3, A. Kokhanovsky, Ed. Berlin, Germany: Springer-Verlag, 2008.

3.8 First Retrieval of CO and OH from Far Infrared Observations of TELIS

J. Xu, F. Schreier, A. Doicu, T. Trautmann

TELIS (TErahertz and submillimeter LImb Sounder) is a state-of-the-art balloon-borne cryogenic heterodyne spectrometer. The instrument uses two 1.8 THz (far infrared) and 480-650 GHz (microwave) channels and monitors the vertical distribution of stratospheric species over an altitude range of 10-32.5 km with 1.5-2 km sampling. During the winters of 2009-2011, three scientific flights onboard the MIPAS gondola took place in Kiruna, Sweden. Here, we present the first retrieval of carbon monoxide (CO) and hydroxyl radical (OH) from the TELIS data in the 1.8 THz channel.

The employed retrieval code PILS (Profile Inversion for Limb Sounding) consists of a line-by-line forward model built on GARLIC (Generic Atmospheric Radiation Line-by-line Infrared Code) and a nonlinear least squares framework coupled with adaptive multi-parameter regularization methods. In this work, the iteratively regularized Gauss-Newton method is used to solve the ill-posed inverse problem involving the reconstruction of molecular concentration profiles from the TELIS spectra. The conventional regularization parameter is defined as a decreasing sequence and iteration-dependent. The number of iteration steps plays the role of the regularization parameter and is determined by an a posteriori stopping rule based on the discrepancy principle.

In addition to the target molecule and the instrument baseline offset, a 'greybody' profile is taken into account in order to treat for the broad continuum-like contributions at lower altitudes that cannot be accurately depicted by current continuum models. Furthermore, the radiometric calibration procedure is modelled in the forward model at each iteration and the cold spectrum is simulated with one up-looking spectrum with zenith angle of 25°.

CO is the major sink of OH in most of the troposphere and the lower stratosphere. TELIS probes CO at the transition frequency of 1841.36 GHz (61.42 cm^{-1}). In the left panel of Fig. 3-18, the CO profile retrieved from TELIS data 20864 is compared to that from the MLS (Microwave Limb Sounder) data (approximately 0.5 h time difference). The difference in the solar zenith angle within 2° ensures that both instruments observed the same air mass around local noon on 24 January 2010. An excellent agreement can be seen in both profiles and the peak at 32.5 km monitored by TELIS was also successfully captured by MLS. The MLS profile overall falls within the accuracy domain of the TELIS profile and both profiles show virtually the identical shape. The error budget of the CO retrieval from TELIS data 20864 is displayed in the right panel of Fig. 3-18. At lower altitudes, the uncertainties in the temperature and pointing information are the two major error sources, with the peak appearing near 15 km. At higher altitudes, the spectroscopic parameters turn out to be the most important error source. The total retrieval error is 0.01-0.25 ppmv.
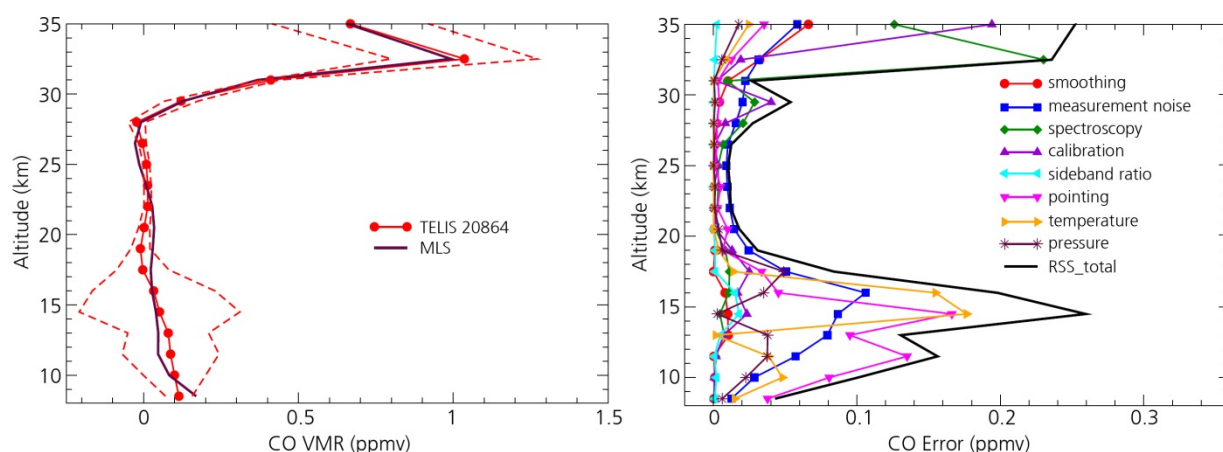
Fig. 3-18: Left: comparison of CO retrievals from TELIS and MLS on 24 January 2010. The dashed lines indicate the estimated overall accuracy of the TELIS retrieval. Right: smoothing, noise, and model parameters errors for the corresponding TELIS CO retrieval.

OH is one of the most interesting species observed in the TELIS far infrared spectra. The two OH triplets around 1834.75 (61.20 cm^{-1}) and 1837.80 GHz (61.30 cm^{-1}) were monitored by the 1.8 THz channel

during the previous flights. The 2009 flight provided observation of OH in the night up to about 35 km. Six measurements with the observer altitude above 25 km were analyzed and are shown in the left panel of Fig. 3-19. Below the highest tangent point, most profiles capture the peak around 25 km and the abundances increase with time. In the right panel of Fig. 3-19, the error budget of the OH retrieval is estimated for TELIS measurement 10890. The pointing information and the measurement noise appear to be the most noticeable errors around 23 and 25 km, respectively. The spectroscopy accuracy does not cause an obvious impact below the observer altitude (approximately 33 km). The overall retrieval error is less than 4 ppbv below 30 km and increases rapidly with the increasing altitude. Because of the large measurement noise, the precision in the OH retrievals is not highly satisfactory. Further investigations into cross-validations of the TELIS OH profiles are ongoing.
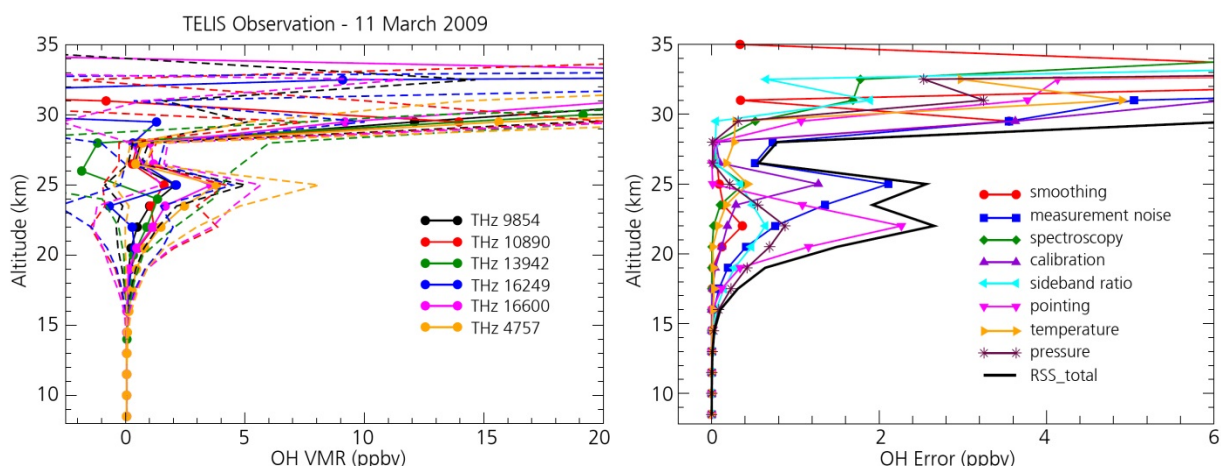

Fig. 3-19: Left: OH profiles retrieved from the TELIS balloon flight data on 11 March 2009. The dashed lines refer to the overall accuracy of OH profiles. Right: smoothing, noise, and model parameters errors for the OH retrieval in the first microwindow. The estimates correspond to TELIS's far infrared measurement 10890 during the 2009 flight.

3.9 Retrieval of Atmospheric Temperature from MTP Measurements: Weighting Functions and First Test Retrieval

J. Xu, F. Schreier, T. Trautmann

The MTP (Microwave Temperature Profiler) instrument was designed to passively measure thermal emission from molecular oxygen in the Earth's atmosphere. The instrument has completed many scientific flights on-board high-altitude research aircrafts, e.g. DLR's HALO, NASA and NCAR aircraft, and allows us to depict spatial and temporal aspects of atmospheric temperatures in the upper troposphere and lower stratosphere. MTP employs double sideband biased mixer and focuses oxygen emissions at the frequency range of 55 to 60 GHz. The HALO-MTP instrument uses local oscillator (LO) frequencies of 56.363, 57.612, and 58.363 GHz. Essentially, a measurement cycle contains a set of 30 brightness temperatures at 3 LO frequencies and at 10 viewing angles.

The retrieval code for MTP's level 2 data processing is adapted from PILS (Profile Inversion for Limb Sounding) and GARLIC (Generic Atmospheric Radiation Line-by-line Infrared Code). In particular, temperature derivatives are obtained by means of automatic differentiation. To reconstruct the vertical temperature profile from the MTP measurements, the inversion algorithm is based on a regularized least squares framework. Currently, the related instrument parameters (e.g. calibration, sideband ratio, pointing) are assumed with ideal values and will be consolidated in the future work.

Weighting functions are used as a quantitative measure that describes how different altitude regimes contribute to the measured radiation and have been widely used in the context of temperature sounding. In Fig. 3-20, the weighting functions for a LO frequency of 57.612 GHz with respect to the chosen viewing angles are plotted. The maximum lies at the bottom of the atmosphere when the instrument detects the atmosphere downwards, whereas the maximum lies between the upper troposphere and lower stratosphere when the instrument looks upwards.

To investigate the performance of temperature retrievals, we implemented the retrievals by using real TELIS data and synthetic MTP data. In the left panel of Fig. 3-21, the temperature profile retrieved from one TELIS submillimeter limb sequence, which was measured on 24 January 2010, is compared against the MIPAS-B retrieval. Aside from some discrepancies at lower altitudes due to regularization, an agreement is reached between both profiles. The right panel of Fig. 3-21 depicts the profile retrieved from one synthetic cycle data of MTP. A denser grid spacing (500 m) is used for altitude levels that are close to the aircraft where the MTP measurements contains most information. The result

Fig. 3-20: Weighting functions for LO frequency of 57.612 GHz with respect to selected viewing angles. The flight altitude was 12.5 km.

shows that the retrieval is overall reasonable despite some oscillations. This can be due to insufficient number of measurements. In the future, the retrieval reliability by using MTP data will be further investigated.
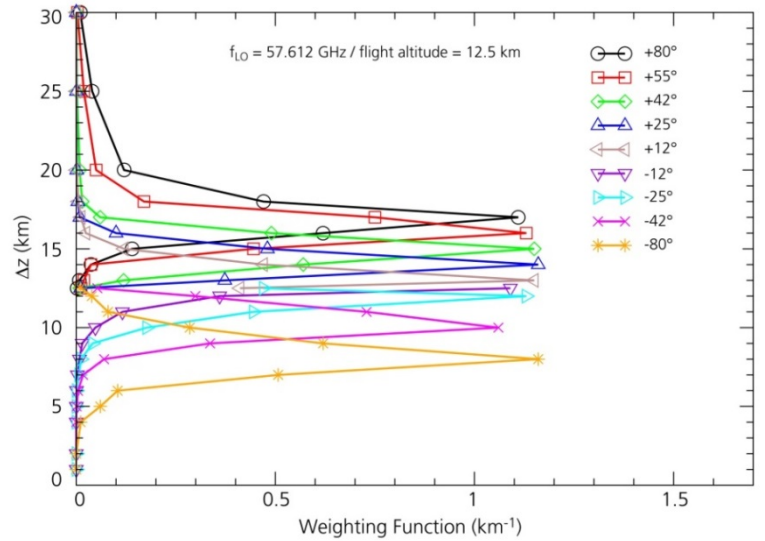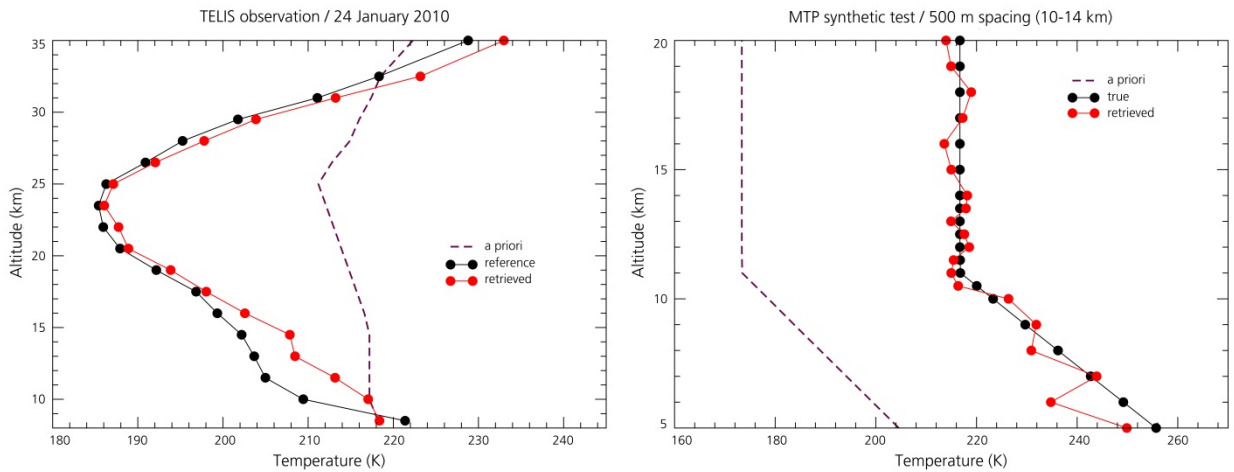

Fig. 3-21: Temperature retrieval from a limb sequence of TELIS submillimeter spectra which were measured on 24 January 2010 (left) and temperature retrieval from a cycle of synthetic MTP measurements (right).

3.10 Recent Upgrades of GARLIC: Temperature Jacobians and Parallelization

F. Schreier, S. Gimeno García, M. Vasquez, J. Xu

GARLIC, our *Generic Atmospheric Radiation Line-by-line Infrared Code*, has been developed for simulations and retrieval applications in Earth and planetary science (*Schreier et al. 2014*). Its computational core routines constitute the basis of the forward models used for various retrieval codes (see chapters 3.8 – TELIS and 3.6 – SCIAMACHY CO). In recent years GARLIC has also been used successfully in modelling exoplanet spectra (see chapter 4.3 – exoplanets), and the feasibility of exoplanet atmospheric remote sensing is currently under investigation. Recent upgrades of the code help to improve further applications of GARLIC.

Temperature Jacobians by algorithmic differentiation

Jacobians, i.e. the partial derivatives of the spectral radiance or transmission with respect to the unknowns of the retrieval, are usually required for the iterative solution of nonlinear inverse problems arising in atmospheric remote sensing. Because the implementation of analytical derivatives in a moderately complex radiative transfer code is costly, error prone, and boring, the derivatives are frequently evaluated by finite difference approximations. However, these are computationally expensive and the appropriate amount of perturbation is difficult to predict. Small perturbations might lead to cancellation errors, whereas large perturbations might give truncation errors. Even worse, the right perturbation might depend on wavenumber, i.e. for spectral regions sensitive to the variable of interest a small perturbation might be sufficient; for example, small (big) changes in ozone can be sufficient (required) in the center (wing) of the 9.6 µm band.
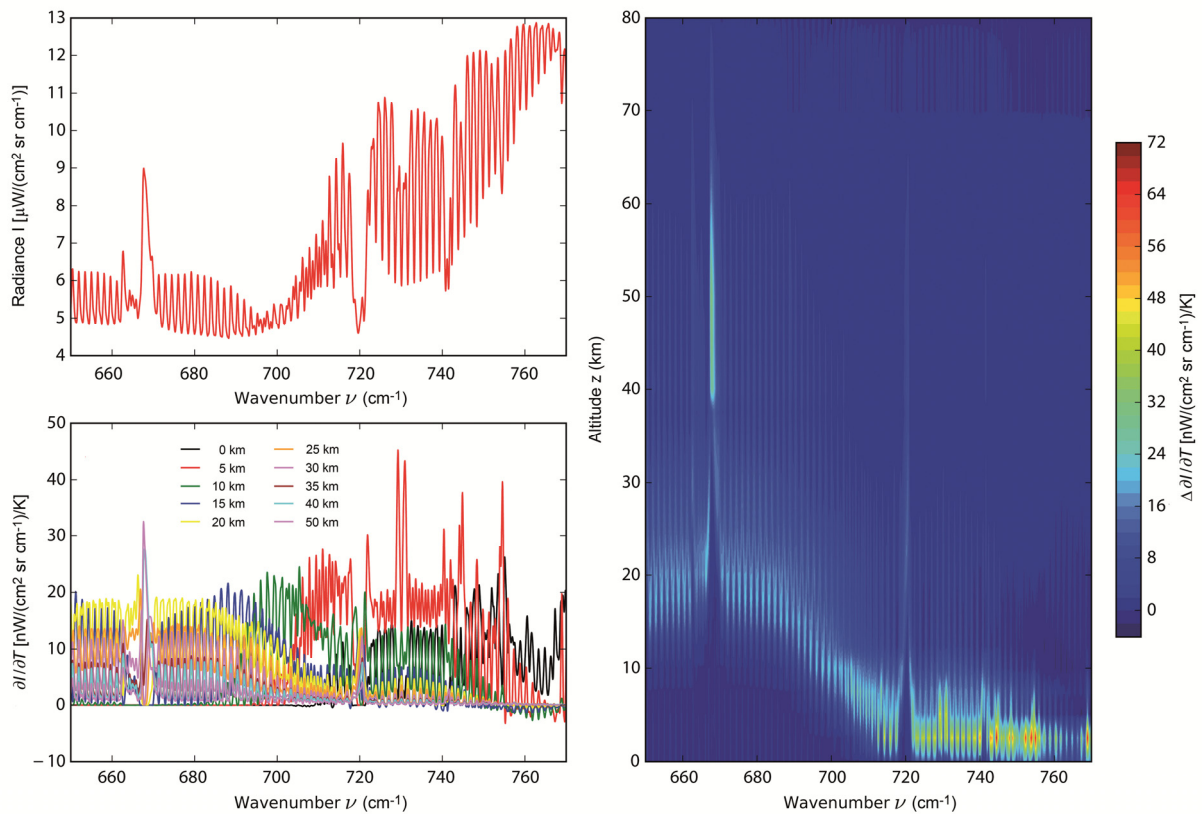
Fig. 3-22: Thermal infrared radiance seen by a downlooking observer (top left) and AD partial derivatives w.r.t. temperature at selected altitude levels (bottom left). Right: Contour plot of the AD atmospheric temperature Jacobian.

In GARLIC, derivatives of radiance and transmission w.r.t. molecular concentration have been implemented utilizing algorithmic (automatic) differentiation (AD) tools. The subroutines generated this way are part of the computational core of the PILS (Profile Inversion for Limb Sounding, *Xu et al. 2013*) and BIRRA (Beer InfraRed Retrieval Algorithm, *Gimeno García et al. 2011*) codes developed for far infrared balloon-borne limb sounding of stratospheric constituents and retrieval of vertical column densities, nb. carbon monoxide and methane, from near infrared nadir observations, respectively. More

recently we have used the source-to-source AD tool TAPENADE (version 3.9) to implement partial derivatives w.r.t. atmospheric and surface temperature. Temperature derivatives are more challenging than derivatives w.r.t. densities because temperature is affecting almost every intermediate variable. In particular, the effective line parameters (width and strength) and the absorption cross sections k are depending on T (ignoring self-broadening, the cross sections are independent of molecular densities).
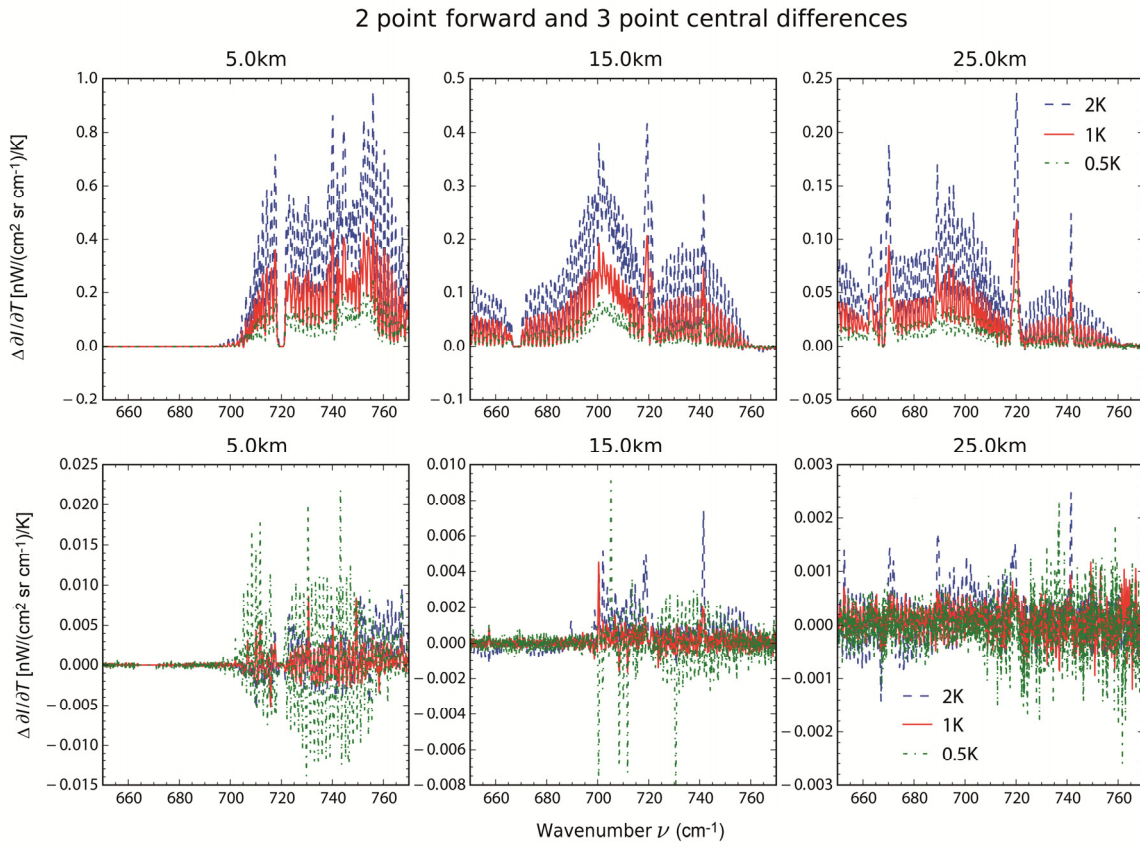
Fig. 3-23: Deviations of two-point forward difference (top) and three-point central difference (bottom) approximations to the AD Jacobian for selected altitudes.

For the verification of the extended code we have performed extensive comparisons of the AD Jacobians with the corresponding finite difference (FD) approximations. Infrared temperature sounders such as IASI or AIRS observe the CO_2 bands at 4.3 and 15 µm. For our tests we model the radiation seen by an IASI-like Fourier transform spectrometer (nadir view) for a tropical atmosphere given on 50 levels. The Jacobian is calculated for temperature assuming a coarse 24 level "retrieval grid". Fig. 3-22 depicts the temperature Jacobians provided by automatic differentiation. The bottom left plot illustrates every second column, i.e. the partial derivative w.r.t. temperature at the altitude given in the legend. The time required to calculate the full Jacobian with 22 columns is increased by only a factor 1.8 compared to the calculation of the radiance spectrum (top left) alone. The difference of two-point finite difference Jacobians to the AD Jacobian is given in Fig. 3-23 (top) for three selected altitudes, indicating serious deviations for all perturbations. Three point central differences, shown in the bottom, are computationally more expensive, but significantly closer to the exact AD Jacobian.

Parallelization
High resolution infrared (and microwave) RT modeling is computationally challenging because the contributions of numerous transitions to the molecular cross section have to be summed up "line-by-line" for several dozens of atmospheric levels on thousands to millions of wavenumber grid points. The widespread availability of multicore CPUs allows further speed-up of the code in addition to the optimization of the Voigt function algorithm and the multigrid approach (*Schreier 2006*, *Schreier 2011*). Cross sections of individual molecules and pressure/temperature levels are independent and are calculated in nested loops in GARLIC. Using the OpenMP library the loop over atmospheric levels has been parallelized. In addition the Schwarzschild or Beer radiative transfer solvers work independently for each wavenumber and can be therefore processed simultaneously. Furthermore OpenMP can be used to

evaluate the absorption coefficients in parallel. In total, this allows a significant speed-up of GARLIC's execution, and the entire thermal infrared spectra typical for a nadir viewing configuration can be calculated in a very short time on a standard desktop machine.

References

Gimeno Garcia, S., Schreier, F., Lichtenberg, G. and Slijkhuis, S.: Near infrared nadir retrieval of vertical column densities: methodology and application to SCIAMACHY. Atmos. Meas. Tech., 4, 2633-2657, 2011.

Schreier, F.: Optimized evaluation of a large sum of functions using a three-grid approach. Comp. Phys. Comm., 174, 783-802, 2006.

Schreier, F.: Optimized implementations of rational approximations for the Voigt and complex error function. J. Quant. Spectrosc. & Radiat. Transfer, 112(6), 1010-1025, 2011.

Schreier, F., Gimeno Garcia, S., Hedelt, P., Hess, M., Mendrok, J., Vasquez, M. and Xu, J.: GARLIC – A general purpose atmospheric radiative transfer line-by-line infrared-microwave code: Implementation and evaluation. J. Quant. Spectrosc. & Radiat. Transfer, 137, 29-50, 2014.

Xu, J., Schreier, F., Vogt, P., Doicu, A. and Trautmann, T.: A sensitivity study for far infrared balloon-borne limb emission sounding of stratospheric trace gases. Geosci. Instrum. Method. Data Syst. Disc., 3, 251-303, 2013.

3.11   Status of the Coupled Atmosphere/Ocean Radiative Transfer Model

D.S. Efremenko, T. Trautmann

Atmospheric correction is the process of removing the effects of the atmosphere on the reflectance values of images taken by satellite or airborne sensors. A common approach for this is to eliminate the influence of the atmosphere by using the solution of the radiative transfer equation (RTE). At the German Remote Sensing Datacenter (DFD) the ATCOR (Atmospheric/Topographic Correction for Satellite Imagery) software package was developed. Currently we are working on the project AC2020, in which our intention is to extend the ATCOR capabilities with respect to usability for water bodies. For this reason we are developing the coupled atmosphere/ocean radiative transfer model. It is based on the discrete ordinate method (DOM), which has proved to be a very efficient method for solving the RTE in the atmosphere (*Stamnes et al. 1988*). As a starting point, we chose the paper by *Jin and Stamnes* (*1994*), where the coupled RTM with a flat ocean surface was introduced. Although formulation and solution of the RTE for the atmosphere-ocean system have a lot in common with those for atmosphere only, there are some important differences. As stated in *Jin et al.* (*2006*) "the implementation of these solutions into [the] code is not trivial however" because some of the technical details are missing in the papers. Developing a coupled RTM appeared to be quite a challenging task. Below is a short overview of key points.
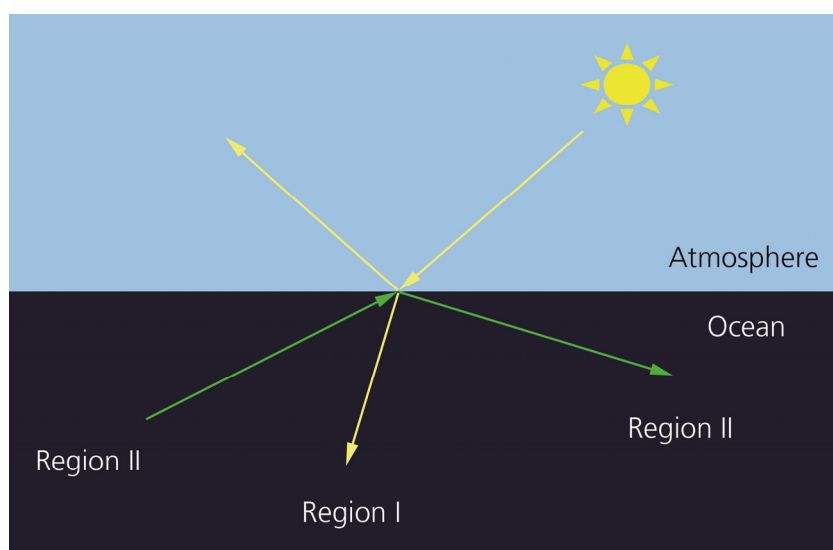

Fig.3-24: The reflection and the transmission of the solar beam inside region I and the total internal reflection inside region II.

Quadrature points and weights

To discretize the integral term in the RTE, a set of double Gauss-Legendre quadrature points and weights in the zenith direction is defined. In the ocean, there are two regions which have to be considered. Both are shown in Fig. 3-24. Region I corresponds to the refraction region and region II to the total-reflection region. All quadrature points in the atmosphere are related to those from the region II by Snell's law. For region II additional quadrature points are required. To guarantee the flux conservation at the atmosphere-ocean interface, the weights in the ocean have to be renormalized.

The source function

Usually, the RTE is considered for the diffuse part of the radiance, while the direct solar beam is treated analytically. The latter appears in the RTE as a source function. The flat surface reflects the direct solar beam contributing an additional term in the source function. However, if there is a roughness in the interface, i.e. due to winds above the water body, then the direct solar beam is scattered but not reflected and, thus, the source function is not affected.

The boundary conditions

In the RTM for atmosphere, there are three boundary conditions:

- no diffuse downwelling radiation at the top of the medium
- continuity of the radiation field at the intermediate atmospheric boundaries
- the condition at the bottom of the medium which can be expressed in terms of BDRF function

In the coupled model with flat surface, these conditions should be complemented by the following three Fresnel conditions at the air-water interface:

- the upwelling radiance in the air is the sum of the Fresnel-reflected downward atmospheric radiation and the Fresnel-transmitted upward aquatic radiation
- downwelling intensity in the water consists of the Fresnel-reflected component of aquatic origin and a Fresnel-transmitted component originated in the atmosphere
- the total internal reflection condition

The main computational difficulty is that the first two conditions encapsulate the radiances given by different number of discrete ordinates.

Reflection and transmission matrices for the air-water interface

In the case of a flat surface, the reflection and transmission matrices are just corresponding Fresnel matrices. In the case of rough surface, the reflection and transmission matrices for a rough surface are computed by taking into account:

- the slope distribution of the surface facets based on the Cox-Munk model
- the shadowing effects
- multiple scattering

We have already implemented RTMs for the flat and rough surfaces. Our next step will be the validation against models CAO-DISORT (*Spurr et al. 2007*) and others.

References

Stamnes, K., Tsay, S.C., Wiscombe, W., Jayaweera K.: Numerically stable algorithm for discrete-ordinate-method radiative transfer in multiple scattering and emitting layered media. Appl. Opt., 12, 2502-2509, 1988.

Jin, Z., Stamnes, K.: Radiative transfer in nonuniformly refracting layered media: atmosphere-ocean system. Appl. Opt., 33, 431-442, 1994.

Jin, Z., Charlock, T.P., Rutledge, K., Stamnes, K., Wang, Y.: Analytical solution of radiative transfer in the coupled atmosphere-ocean system with a rough surface. Appl. Opt. 45, 7443-7455, 2006.

Spurr, R., Stamnes, K., Eide, H., Li W., Zhang, K., Stamnes, J.: Simultaneous retrieval of aerosols and ocean properties: A classic inverse modeling approach. I. Analytic Jacobians from the linearized CAO-DISORT model. J. Quant. Spectrosc. & Radiat. Transfer, 104, 428-449, 2007.

3.12 VSHDOM — The Polarized Version of the Spherical Harmonics Discrete Ordinate Method Model

T. Trautmann, A. Doicu, D. Efremenko

One of the most efficient and widely used multi-dimensional deterministic methods to solve scalar radiative transfer in the atmospheric sciences is the Spherical Harmonics Discrete Ordinate Method (SHDOM) developed by Frank Evans, see *Evans (1998)* and the webpage http://nit.colorado.edu/shdom.html which provides the user with a download of SHDOM. Since polarized radiation plays an important role for many applications, the question arose how the model can be extended to compute the full Stokes vector $\mathbf{I} = [I, Q, U, V]^T$. In the following we briefly describe the main mathematical and technical steps of the VSHDOM implementation. Note that the new SHDOM distribution which F. Evans made available on 7 March 2014, includes the mathematical steps described in this short note and with more details in *Doicu et al. (2013)*.

The vector radiative transfer equation (VRTE) can be written in the form

$$\frac{d\mathbf{I}}{ds}(\mathbf{r}, \mathbf{\Omega}) = \sigma_{ext}(\mathbf{r})[\mathbf{I}(\mathbf{r}, \mathbf{\Omega}) - \mathbf{J}(\mathbf{r}, \mathbf{\Omega})] \tag{1}$$

where $\mathbf{r}$ is a generic point with three-dimensional coordinates, $\mathbf{\Omega}$ is the unit directional vector describing the direction in which the radiation is travelling, σ_{ext} is the extinction coefficient. $\mathbf{J}$ is the so-called source function vector

$$\begin{aligned} \mathbf{J}(\mathbf{r}, \mu, \varphi) = {} & \frac{\omega(\mathbf{r})}{4\pi} \, \mathbf{Z}(\mathbf{r}, \mu, -\mu_0, \varphi - \varphi_0) \mathbf{F}_0 e^{-\tau_{ext}^{sun}(\mathbf{r})} + [1 - \omega(\mathbf{r})]\mathbf{B}(\mathbf{r}) \\ & + \frac{\omega(\mathbf{r})}{4\pi} \int_0^{2\pi} \int_0^1 \mathbf{Z}(\mathbf{r}, \mu, \mu', \varphi - \varphi') \mathbf{I}(\mathbf{r}, \mu', \varphi') \, d\mu' \, d\varphi' \end{aligned} \tag{2}$$

which includes thermal and solar sources. $\mathbf{Z}$ is the phase matrix, ω is the single scattering albedo, and the unpolarized incoming solar and the thermal radiation vectors are given by $\mathbf{F}_0 = [F_0, 0, 0, 0]^T$ and $\mathbf{B} = [B(T), 0, 0, 0]^T$ where T is the thermodynamic temperature within the medium. The quantity $\tau_{ext}^{sun}(\mathbf{r})$ is the optical depth for the solar radiation to the generic point $\mathbf{r}$. The medium has been assumed to be macroscopically isotropic containing mirror-symmetric particles. The direction of the incident solar radiation is given by $\mathbf{\Omega}_0 = (-\mu_0, \varphi_0)$. Note that for upwelling radiation we have always $\mu > 0$, while downwelling radiation is signalled via $-\mu$ (with always being $\mu > 0$).

SHDOM treats the scalar source function expansion in the following way

$$J(\mathbf{r}, \mu, \varphi) = \sum_{m=0}^{M} \sum_{l=0}^{L} Y_{lm}(\mu, \varphi) J_{lm}(\mathbf{r}) \, , \tag{3}$$

where the functions $Y_{lm}(\mu, \varphi)$ are the classical real-valued spherical harmonics, defined on the unit sphere. For example, SHDOM expands the scalar intensity I field via

$$I(\mathbf{r}, \mu, \varphi) = \sum_{m=0}^{M} \sum_{l=0}^{L} [I_{lm}^+(\mathbf{r}) Y_{lm}^+(\mu, \varphi) + I_{lm}^-(\mathbf{r}) Y_{lm}^-(\mu, \varphi)] \, , \tag{4}$$

with the definitions

$$Y_{lm}^+(\mu, \varphi) = \gamma_{lm} \mathcal{P}_l^m(\mu) \cos(m\varphi), \quad Y_{lm}^-(\mu, \varphi) = \gamma_{lm} \mathcal{P}_l^m(\mu) \sin(m\varphi) \, , \tag{5}$$

where the $\mathcal{P}_l^m$ are the real-valued associated Legendre polynomials and the γ_{lm} are some normalization constants.

One important point, when going from the scalar SHDOM algorithm to the more complicated vector case, is to find a suitable system of expansion functions for separating the various functional dependencies of $\mathbf{I}$, $\mathbf{Z}$, and $\mathbf{J}$, see also the report by *Evans (2013)*. In the vector case, the so-called generalized spherical harmonics represent a suitable function space, partly because these particular

functions are intimately connected with the azimuthal expansion of the phase matrix $\mathbf{Z}$ given by (j is the imaginary unit)

$$\mathbf{Z}(\mu, \mu', \varphi - \varphi') = \sum_{m=-M}^{M} \mathbf{Z}_m(\mu, \mu') e^{jm(\varphi - \varphi')} , \tag{6}$$

where the complex amplitudes in (6) are determined by

$$\mathbf{Z}_m(\mu, \mu') = \sum_{n=|m|}^{N} \mathbf{T}\mathbf{P}_{nm}(\mu)\mathbf{G}_n\mathbf{P}_{nm}(\mu')\mathbf{T}^* . \tag{7}$$

The superscript $*$ denotes matrix conjugate.

The other quantities occurring in (7) are

$$\mathbf{T} = \frac{1}{\sqrt{2}} \ (\mathbf{I}_4 + j\mathbf{D}) \tag{8}$$

where $\mathbf{I}_4 = \mathrm{diag}[1,1,1,1]$ is the four-dimensional identity matrix, $\mathbf{D} = \mathrm{diag}[1,1,-1,-1]$,

$$\mathbf{P}_{nm}(\mu) = \begin{bmatrix} d_{m0}^n(\mu) & 0 & 0 & 0 \\ 0 & d_{m+}^n(\mu) & d_{m-}^n(\mu) & 0 \\ 0 & d_{m-}^n(\mu) & d_{m+}^n(\mu) & 0 \\ 0 & 0 & 0 & d_{m0}^n(\mu) \end{bmatrix}, \tag{9}$$

$$\mathbf{G}_n = \begin{bmatrix} \chi_{1n} & \zeta_{1n} & 0 & 0 \\ \zeta_{1n} & \chi_{2n} & 0 & 0 \\ 0 & 0 & \chi_{3n} & \zeta_{2n} \\ 0 & 0 & -\zeta_{2n} & \chi_{4n} \end{bmatrix} \tag{10}$$

with the normalized Wigner d-functions $d_{mm'}^n$, $d_{m\pm}^n(\mu) := -\frac{1}{2}[d_{m2}^n(\mu) \pm d_{m-2}^n(\mu)]$, and the expansion coefficients of the scattering phase matrix

$$\mathbf{F}(\Theta) = \begin{bmatrix} a_1(\Theta) & b_1(\Theta) & 0 & 0 \\ b_1(\Theta) & a_2(\Theta) & 0 & 0 \\ 0 & 0 & a_3(\Theta) & b_2(\Theta) \\ 0 & 0 & -b_2(\Theta) & a_4(\Theta) \end{bmatrix} . \tag{11}$$

For example, in terms of the Wigner d-functions one obtains

$$a_1(\Theta) = \sum_{n=0}^{N} \sqrt{\frac{2n + 1}{2}} \chi_{1n} d_{00}^n(\cos \Theta) . \tag{12}$$

Expressions for the other terms in $\mathbf{F}(\Theta)$ can be found, for example, in *Mishchenko et al. (2000)* and *Hovenier et al. (2004)*.

In view of (7), we define the complex generalized spherical harmonics by

$$\mathbf{Y}_{nm}(\mu, \varphi) = \frac{1}{\sqrt{2\pi}} \ \mathbf{T}\mathbf{P}_{nm}(\mu) e^{jm\varphi} . \tag{13}$$

The important orthogonality relation of the $\mathbf{Y}_{nm}$ functions is given by (cf. integration on the unit sphere)

$$\int_0^{2\pi} \int_{-1}^{1} \mathbf{Y}_{nm}(\mu, \varphi)\mathbf{Y}_{n'm'}^H(\mu, \varphi) d\mu \, d\varphi = \mathbf{J}_n \delta_{nn'} \delta_{mm'} , \tag{14}$$

where for $n = 0$, 1, we have $\mathbf{J}_n = \mathrm{diag}[1,0,0,1]$, while for $n > 1$, there is $\mathbf{J}_n = \mathbf{I}_4$. Above, the superscript H denotes the conjugate transpose of a complex matrix.

After these introductory comments and, for ease of notation, when leaving off the **r** dependency, we now introduce the expansions for both the phase matrix, the intensity vector as well as the source function vector in terms of the complex generalized spherical harmonics:

$$\mathbf{Z}(\mu, \mu', \varphi - \varphi') = 2\pi \sum_{m=-M}^{M} \sum_{n=|m|}^{N} \mathbf{Y}_{nm}(\mu, \varphi) \mathbf{G}_n \mathbf{Y}_{nm}^H(\mu', \varphi') , \tag{15}$$

$$\mathbf{I}(\mu, \varphi) = 2\pi \sum_{m=-M}^{M} \sum_{n=|m|}^{N} \mathbf{Y}_{nm}(\mu, \varphi) \mathbf{I}_{nm} , \tag{16}$$

$$\mathbf{J}(\mu, \varphi) = \sum_{m=-M}^{M} \sum_{n=|m|}^{N} \mathbf{Y}_{nm}(\mu, \varphi) \mathbf{J}_{nm} , \tag{17}$$

Further orthogonality relations to be used are the ones for the Wigner d-functions and for the $\mathbf{P}_{nm}$ matrices:

$$\int_{-1}^{1} d_{mm'}^n(\mu) d_{mm'}^{n'}(\mu) \, d\mu = \delta_{nn'} , \tag{18}$$

$$\int_{-1}^{1} \mathbf{P}_{nm}(\mu) \mathbf{P}_{n'm}(\mu) \, d\mu = \mathbf{J}_n \delta_{nn'} . \tag{19}$$

A key result for the VSHDOM development is the form of the complex generalized spherical harmonics expansion coefficients for the source function vector $\mathbf{J}(\mathbf{r}, \mu, \varphi)$

$$\mathbf{J}_{nm} = \frac{\omega}{2} \mathbf{G}_n \mathbf{I}_{nm} + \frac{\omega}{2} \mathbf{G}_n \mathbf{Y}_{nm}^H(-\mu_0, \varphi_0) \mathbf{F}_0 e^{-\tau_{\text{ext}}^{\text{sun}}} + (1 - \omega) \sqrt{4\pi} \mathbf{T}^* \mathbf{B} \delta_{n0} \delta_{m0} . \tag{20}$$

which can be easily derived from (1), (13) and (16).

Given the intensity vector, its expansion coefficients can be computed via

$$\mathbf{I}_{\text{nm}}(\mathbf{r}) = \int_0^{2\pi} \int_{-1}^{1} \mathbf{Y}_{nm}^H(\mu, \varphi) \mathbf{I}(\mathbf{r}, \mu, \varphi) \, d\mu \, d\varphi . \tag{21}$$

For further information on algorithmic details and on some computational results we refer the reader to *Doicu et al. (2013)*. In order to avoid complex arithmetic, we also transferred the VSHDOM algorithm to use only real-valued generalized spherical harmonics, retaining the same accuracy of the evaluation, but saving some computational effort. Fig. 3-25 illustrates the individual computations steps in VSHDOM which closely follow the steps of the original SHDOM code.

Moreover, an independent column approximation based on the discrete ordinate with matrix exponential (DOME) radiative transfer model (*Doicu and Trautmann 2009*) has been implemented in VSHDOM having the following features:

- The direct solar beam is computed in an inhomogeneous atmosphere at all grid points.
- The Stokes vector at all grid points and in all discrete ordinate directions is determined by DOME.
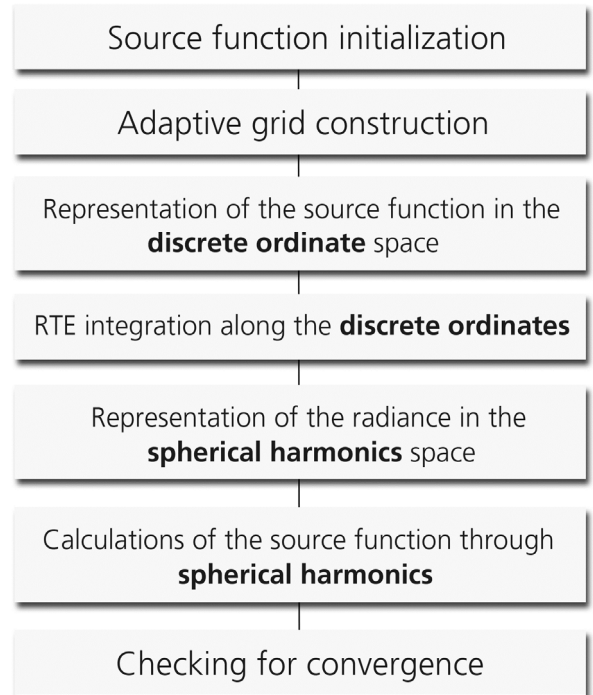- The expansion coefficients of the Stokes vector are computed using the real-valued

Fig. 3-25: Illustration of various computational steps in the original SHDOM code which are also the basis for the extended VSHDOM model.

generalized spherical harmonics, while the expansion coefficients of the source vector are calculated by using (20) or its real-valued counterpart.
- The Stokes vector at a specific viewing direction is computed in the inhomogeneous atmosphere by using the integral form of the radiative transfer equation.

In summary, it can be concluded that the multi-dimensional scalar Spherical Harmonics Discrete Ordinate Method (SHDOM) has been extended to the vector case version VSHDOM. VSHDOM uses complex and real generalized spherical harmonics in the energetic representation of the Stokes vector, **I**, and retains some powerful features of the scalar model, such as e.g.,

- the combination of the generalized spherical harmonic and the discrete ordinate representations of the radiance field,
- the use of a linear short characteristic method for computing the corner-point values of the Stokes vector,
- and the application of the adaptive grid technique.

Future work will include the next logical but difficult step, namely to develop a linearized version of VSHDOM which is required for retrieval applications.

References

Doicu, A., and Trautmann, T.: Discrete-ordinate method with matrix exponential for a pseudo-spherical atmosphere: vector case. J. Quant. Spectrosc. & Radiat. Transfer, 110, 159-172, 2009.

Doicu, A., Efremenko, D., and Trautmann, T.: A multi-dimensional vector spherical harmonics discrete ordinate method for atmospheric radiative transfer. J. Quant. Spectrosc. & Radiat. Transfer, DOI 10.1016/j.jqsrt.2012.12.009, 2013.

Evans, K.F.: The spherical harmonic discrete ordinate method for three-dimensional atmospheric radiative transfer. Journal of the Atmospheric Sciences, 55, 429-446, 1998.

Evans, K.F.: Progress Report for "Three-dimensional polarized radiative transfer modeling with an upgraded SHDOM", Period: June 10, 2012 – June 9, 2013. Award NNX11AJ94G to the University of Colorado, Boulder, May 6, 2013.

Hovenier, J.W., van der Mee, C., and Domke, H.: Transfer of Polarized Light in Planetary Atmospheres: Basic Concepts and Practical Methods. Kluwer Academic Publishers, Dordrecht, London, 2004.

Mishchenko, M., Hovenier, J.W., and Travis, L.D. (Eds.): Light Scattering by Nonspherical Particles: Theory, Measurements, and Applications. Academic Press, San Diego, London, 2000.

3.13 Studying the "Independent Scattering" Assumption for Double Slits and Bispheres

T. Rother, K. Schmidt

The assumption of independent scattering is of some importance in a variety of different scattering scenarios (*van de Hulst 1981*). This applies not only to the realm of remote sensing (see, e.g. *Doherty et al. 1999*) but also in technical and medical diagnostics such as, e.g., the characterization of granular materials by using Terahertz extinction spectroscopy (see, e.g. *Born et al. 2014*). This assumption is related to an ensemble of scattering particles within an illuminated volume element. Its justification requires the consideration of two different effects. These are the interference of the scattered fields produced by, and the scattering interaction between different particles of the ensemble. The well-known double slit experiment provides a unique possibility to study exclusively the former effect since both slits are usually located in a common plane. Therefore, no interaction between the slits must be considered. However, for bispheres we have to take both the interference effect as well as the interaction contribution into account. The following considerations are restricted to the simple scattering configuration of a monolayer of double slits and bispheres both oriented perpendicularly with respect to the incident plane wave. Although it is a very special scattering configuration it can actually be met in some applications.

When starting with the double slit, Fig. 3-26 illustrates the scattering configuration.
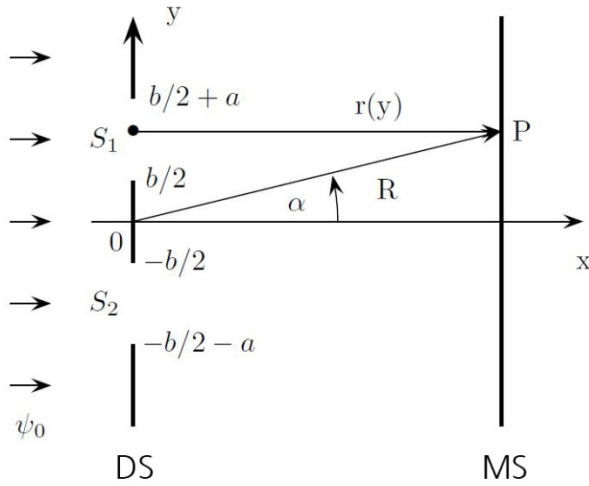
Fig. 3-26: Scattering of a plane wave ψ_0 perpendicularly incident from the left on a double slit (DS). The measurement screen (MS) is placed in the far field behind the double slit. Both slits S_1 and S_2 are symmetrically placed with respect to the *x*-axis (slit distance *b*), infinitely extended into the *z*-direction, and characterized by the same slit width *a*.

For our purposes it is worthwhile to express the differential scattering cross section of the double slit in terms of the corresponding scattering cross section of the single slit. Within the Fraunhofer diffraction approach we thus get

$$I_{DS}(\alpha) = 4 \cdot I_S(\alpha) \cdot \cos^2 \Gamma_+$$

$$I_S(\alpha) = \left(\frac{k\,a}{2\pi}\right)^2 \cdot \frac{\sin^2 \Gamma_a}{\Gamma_a^2}$$

is the differential scattering cross section of the single slit. Γ_+ is the sum of Γ_a and Γ_b, with

$$\Gamma_{a/b} = \frac{k\,a/b}{2} \cdot \sin \alpha$$

The prefactor "4" in the first expression is of importance for the following discussion. A typical scattering result is presented in Fig. 3-27.

It can be seen that $4 \cdot I_S(\alpha)$ forms the envelope of the double slit, modified by the term $\cos^2 \Gamma_+$. Moreover, the intensity maxima of the double slit are always identical with $4 \cdot I_S(\alpha)$. Now, regarding the independent scattering assumption, it is assumed that averaging over different slit distances of the double slit will

40

produce a differential scattering cross section comparable to the red line in Fig. 3-27, i.e. to an intensity distribution that is twice of the single slit! However this does not apply to the near forward direction as clearly shown by Fig. 3-28.

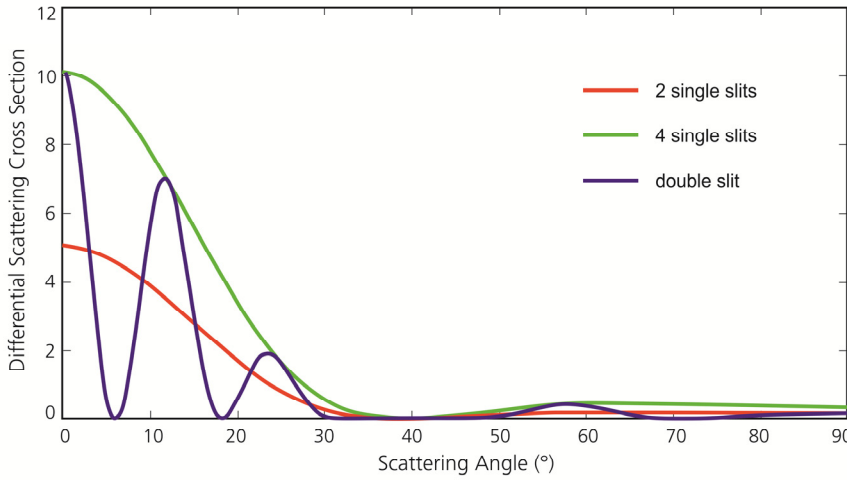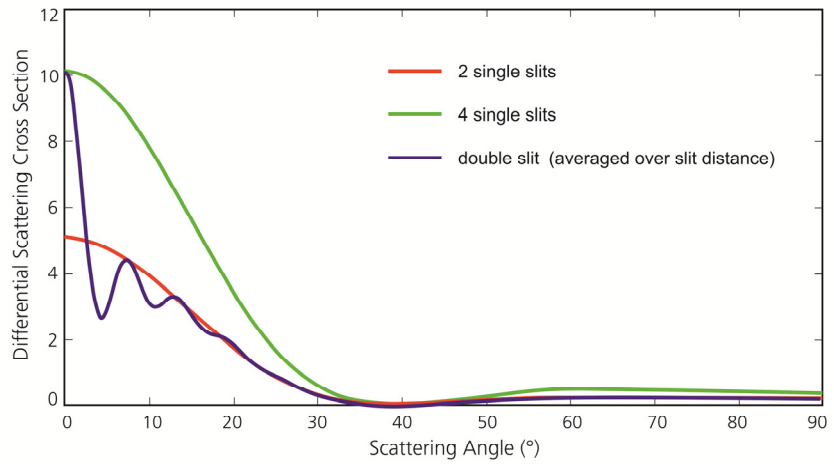Fig. 3-27: Sum of the differential scattering cross sections of two and 4 single slits in comparison to the result of the double slit. Size parameter: *ka=10,* slit distance: *b=2a.*

Fig. 3-28: The differential scattering cross section of the double slit was obtained by an averaging procedure over 50 different slit distances.

On the other hand, for scattering angles α with 15° ≤ α ≤ 90° the independent scattering assumption for the double slit is justified if averaged over different slit distances.

Next, we replace the two slits S_1 and S_2 in Fig. 3-26 by two dielectric but non-absorbing spheres. Fig. 3-29 displays the scattered intensity for a fixed distance between the spheres at a plane wave incidence. Note that the program *mstm* by *Mackowski and Mishchenko* (*2011*) is based on a T-matrix approach. The T-matrix is obtained by an iterative solution of an interaction equation system. The parameter *max_number_iterations* confines the maximum number of the iterations to be used in the program. Setting this parameter to zero results in a solution where no scattering interactions between the spheres but only interference effects are taken into account. This is represented by the blue line in Fig. 3-29, labelled "mstm (without interaction)". It corresponds directly to the blue line in Fig. 3-27. Analogously to Fig. 3-27, "4 times Mie theory" forms the envelope of the bisphere result without the interaction in the forward and also in the backscattered region. And again, the intensity maxima of the latter are always identical to "4 times Mie theory". Taking the scattering interaction between the spheres into account leads to a modification of this behavior. The result of averaging over the sphere distance Δx is shown in Fig. 3-30.

It is obvious that the scattering behavior of the bisphere can be well described by that of two independent spheres within the scattering angle range of about 5° to 175°. But this does not apply to the near forward and backward direction. Moreover, scattering interactions between the spheres in the ensemble can be approximately neglected in that special case.
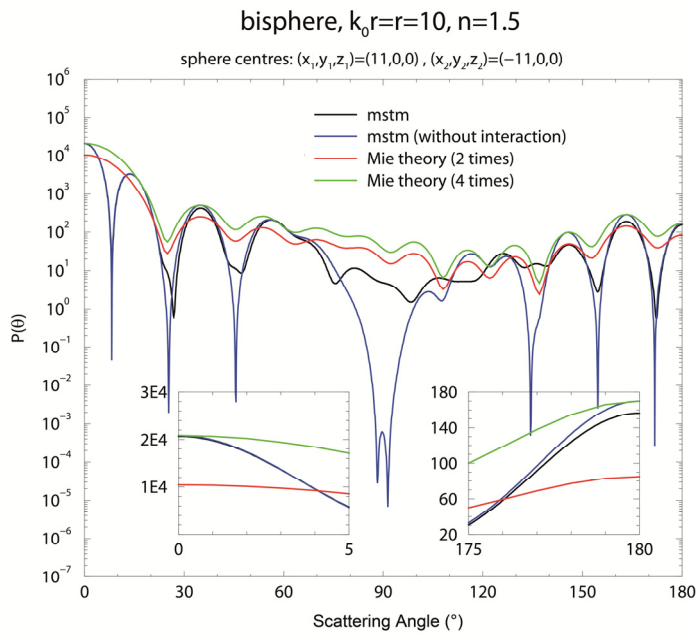
bisphere, k₀r=r=10, n=1.5

Fig. 3-29: Sum of the phase functions of two and 4 single spheres, obtained by Mie theory, in comparison to the results of the bisphere with and without the scattering interaction, obtained by the program mstm (*Mackowski and Mishchenko 2011*). Size parameter of each sphere: $k_0r=r=10$ with $\lambda=2\pi$, r – radius of each sphere, λ – wavelength, real refractive index of each sphere: n=1.5. Both spheres centred in Cartesian coordinates according to: $(x_1,y_1,z_1)=(11,0,0)$ and $(x_2,y_2,z_2)=(-11,0,0)$.

Fig. 3-30: Same as Fig. 3-29, but with an averaging over 301 sphere distances $\Delta x = 0,1,2,\ldots,300$.

bisphere, k₀r=r=10, n=1.5

Conclusion

In scattering measurements that are based on coherent incident fields (such as Lidar and Radar measurements or the initially mentioned Terahertz spectroscopy) the violation of the independent scattering assumption in the near forward and backward direction has to be considered as a potential source of errors in the scattering data analysis. However, the discussed interference effects can be neglected if incoherent incident fields are considered, such as, e.g., in passive satellite remote sensing with the sunlight as the primary source. Moreover, regarding the scattering interaction of bispheres, we may state that this effect plays a minor role in the considered scattering configuration if averaging over different distances is performed. The scattering behavior is clearly dominated by the interference effect.

References

Doherty, S.L., Anderson, T.L. and Charlson, R.J.: Measurement of the lidar ratio for atmospheric aerosols with a 180° backscatter nephelometer. Appl. Optics 38, 9, 1999.

Born, P., Holldack, K. and Sperl, M.: Particle characterization using THz spectroscopy. arXiv: 1407.6592, 2014.

van de Hulst, H.C.: Light Scattering by Small Particles, Dover Pub., New York, 1981.

Mackowski, D.W. and Mishchenko, M.I.: A multiple sphere T-matrix Fortran code for use on parallel computer clusters. J. Quant. Spectrosc. & Radiat. Transfer, 112, 2182, 2011.
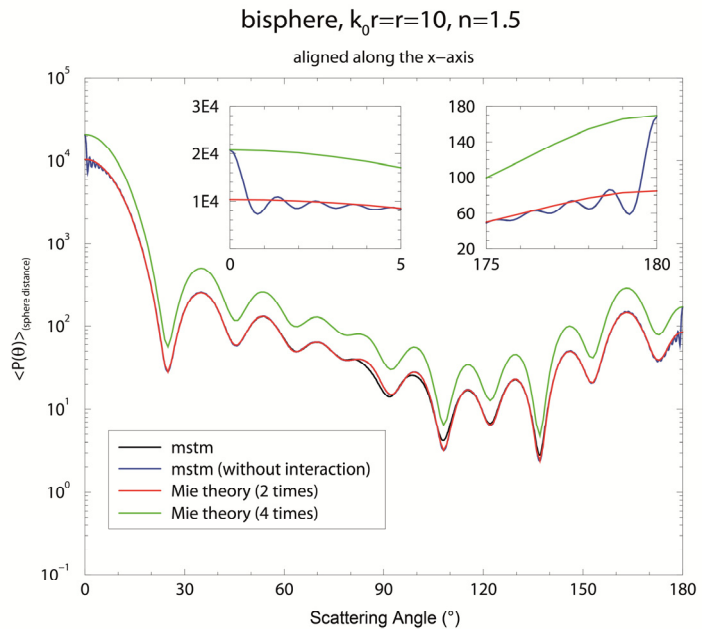
3.14 Methods for Electromagnetic Scattering by Large Axisymmetric Particles with Extreme Geometries – An Overview

A. Doicu, Y. Eremin, D.S. Efremenko, T. Trautmann

In atmospheric radiative transfer and remote sensing, accurate computations of electromagnetic scattering by large particles with extreme geometries are often required. A first method which serves this purpose is the discrete sources method. The approximate solution to the scattering problem is constructed as a finite linear combination of fields of elementary sources. The discrete sources are placed on a certain support, and the unknown amplitudes of the discrete sources are determined from the boundary conditions. As discrete sources localized, distributed and multiple spherical vector wave functions (SVWF), magnetic and electric dipoles, and systems of vector Mie potentials with singularities distributed on auxiliary closed and open surfaces can be used (*Doicu et al. 2000*).

The null-field method (otherwise known as the extended boundary condition method) is also suitable for analyzing the electromagnetic scattering by large and highly aspherical particles. The method was initially proposed by *Watermann* (*1965*). In the framework of the null-field method, the transition matrix relating the expansion coefficients of the scattered and incident field is derived as

$$\mathbf{T} = -\mathbf{Q}^{11} \, (\mathbf{Q}^{31})^{-1}$$

where the matrix $\mathbf{Q}^{31}$ is obtained by imposing the null-field condition inside a spherical surface enclosed in the particle, and the matrix $\mathbf{Q}^{11}$ is obtained from the Huygens principle. The elements of the $\mathbf{Q}$ matrices are expressed as integrals of products of SVWFs over the particle surface. Despite its wide range of applicability, the method suffers from numerical problems regarding convergence and loss of accuracy. The reason is that for large and/or strongly deformed particles, the matrix $\mathbf{Q}^{31}$ becomes severely ill conditioned, and the inversion process is negatively influenced by round-off errors.

A number of methods have been proposed to improve the numerical stability in computations for large particles with extreme geometries. We distinguish the following categories of methods:

- Methods dealing with the numerical stability of the inversion process: The orthogonalization approach which exploits the unitarity property of the T-matrix, the Gauss elimination method with back substitution, the block matrix inversion method, and the perturbation approach for the Q-matrix inversion fall into this category.
- Methods dealing with an accurate computation of the Q-matrix elements: *Somerville et al.* (*2012*) found that in the case of spheroids, the numerical computation of the integrals of the $\mathbf{Q}^{31}$-matrix elements may suffer a significant loss of precision due to exact cancellations of large parts of the integrand.
- Methods dealing with an accurate computation and inversion of the matrix $\mathbf{Q}^{31}$ by using extended- and the multiple-precision floating-point variables.
- Methods leading to better conditioned systems of equations: These methods rely on formal modifications of the single spherical coordinate-based null-field method and include the iterative version of the null-field method, the use of sub-boundary bases for surface fields approximation, the application of the spheroidal coordinate formalism, and the null-field method with discrete sources. In *Doicu et al.* (*2006*) only distributed spherical vector wave functions with origins located on the axis of symmetry of the particle or in the complex plane have been considered, and convergent results for prolate axisymmetric particles with a size parameter of about 100, and oblate axisymmetric particles with a size parameter of about 30 have been reported.

Presently, it seems that a hybrid method consisting in a combination of the null-field method and invariant imbedding method is one of the most efficient tools for analyzing the electromagnetic scattering by large particles. The invariant imbedding method initially proposed by *Johnson* (*1988*) relies on a volume integral equation and iteratively computes the T-matrix by growing the scattering volume incrementally in a shell-by-shell manner. The null-field method is used to initialize the iterative procedure involved in the invariant imbedding method, or equivalently, to compute the T-matrix of a partial volume of the particle whose surface is the initial position in the invariant imbedding iteration. The invariant imbedding method is not very efficient because a large number of spherical shells have to be considered for discretizing large sized particle volumes. However, for axisymmetric particles, the

parallelization of the code based on the Message Passing Interface (MPI) technology leads to reasonable computational times. In this case, the calculations of the T-matrices corresponding to different azimuthal modes are distributed to different processors.

We analyzed the applicability of the discrete sources method and the null-field method with discrete sources to electromagnetic scattering by large and strongly deformed axisymmetric particles. As discrete sources localized, distributed and multiples spherical vector wave functions are considered. In addition, we also analyzed the applicability of the discrete sources method with distributed SVWFs and the null-field method with localized, distributed and multiple SVWF to electromagnetic scattering by large axisymmetric particles with extreme geometries. The conclusions of our analysis can be summarized as follows:

- For prolate particles, a distribution of the discrete sources on the axis of symmetry of the particle guarantees the convergence of the computational schemes.
- For oblate particles, the procedure of analytic continuation of the spherical vector wave functions onto the complex plane have to be considered. In this case, the null-field method is very efficient and increases the stability of the computational scheme. It should be regarded as an improvement of the conventional null-field method for large particles with extreme geometries. An inconvenience of the method is the multiple-precision implementation of the inversion algorithm, which increases the computational time by a factor of 2 as compared to an extended-precision implementation. The applicability of the (regularized) total least squares method, dealing with errors in the matrix $\mathbf{Q}^{31}$, and of an inversion algorithm using multiple precision floating-point format and a multiplicative correction will be analyzed in the future.

References

Doicu, A., Eremin, Y., Wriedt, T.: Acoustic and Electromagnetic Scattering Analysis Using Discrete Sources. London: Academic Press, 2000.

Waterman, P.C.: Matrix formulation of electromagnetic scattering. Proc. 1965 IEEE, 53, 805-812, 1965.

Somerville, W.R.C., Auguie, B., Le Ru, E.C.: Severe loss of precision in calculations of T -matrix integrals. J. Quant. Spectrosc. & Radiat. Transfer, 113, 524–535, 2012.

Doicu, A., Wriedt, T., Eremin, Y.: Light Scattering by Systems of Particles. Springer, Berlin, Heidelberg, New York, 2006.

Johnson, B.R.: Invariant imbedding T-matrix approach to electromagnetic scattering. Appl. Opt., 27, 4861–4873, 1988.

3.15   Implementation of Radiative Transfer Solvers on GPUs

D.S. Efremenko, D. Loyola, A. Doicu, R.J.D. Spurr

The future atmospheric composition Sentinel missions will generate two orders of magnitude more data than the current missions and the operational processing of such big data is a big challenge. The trace gas retrieval from remote sensing data usually requires high-performance radiative transfer model (RTM) simulations and the RTM are usually the bottleneck for the operational processing of the satellite data. Originally designed for computer graphics, graphical processor unit (GPU) based platforms have attracted increasing attention in many fields with highly intensive computations. The main goals of our work were to design RTM code for GPU architecture and to investigate the possible advantages of GPU computations over conventional CPU-based multicore parallelization techniques in terms of performance enhancement.

The radiative transfer equation (RTE) in a one-dimensional medium is well-known. The discrete ordinate method (DOM) for solving the RTE is numerically stable *(Stamnes et al. 1988)* for arbitrary optical thicknesses in a multi-layer stratified medium, and the method is used in a number of RT software packages such as SCIATRAN, LIDORT, DISORT, PSTAR and others. An important parameter controlling the computational time and the accuracy of computations is the number of streams in the polar hemisphere N_{do}. RTMs are called "multi-stream" if $N_{do} \geq 2$, and "two-stream" if $N_{do} = 1$.

The computations for different pixels are independent and can be computed in parallel. To perform the parallel computations, we used the CUDA (Compute Unified Device Architecture) framework. The CUDA kernel is exploited to parallel-process all tasks using threads, instead of using a "for" loop to go through all the tasks in turn. A crucial issue regarding performance is memory management. Several approaches have been analyzed for the kernel implementation to maximize the occupancy of GPU. They exploit features of different types of GPU memory. For instance, the registers is the fastest memory, however the number of 32-bit registers per multiprocessor is about 64000. In contrast, the global memory size is about several gigabytes, but the access latency is 2 orders of magnitude higher than that of registers. The optimal memory organization depends on the size of arrays and specific features of the problem to be solved. Also we considered the parallelization at the level of matrix operations (i.e., some threads perform a matrix multiplication). Such technique is based on the Dynamic Parallelism concept: a child CUDA kernel can be called from within a parent CUDA kernel and then optionally synchronize on the completion of that child CUDA kernel. We have used asynchronous host/device data transfer by making use of so called "pinned" memory. Also, from the perspective of the CPU, the CUDA kernel launch is non-blocking. Thence, CPU can perform computations overlapped with the execution on the GPU.

All results are generated from an Intel Xeon CPU E5-1620 3.60GHz with 8 CPUs and the NVIDIA device Tesla K20c with 2496 cores. The single scattering correction and two-stream subroutines are implemented with separate kernels. For both, allocation in the pinned memory (PM) and asynchronous data transfer (ADT) are used. Speed-ups for the single scattering and two stream codes (when compared to the single-threaded CPU codes) are 18 and 53, respectively. The single scattering correction subroutine achieves about an 80% performance improvement when ADT is used. The single scattering correction does not have intensive computations – reading the data from global memory is a bottleneck of the kernel performance. On the other hand, the two-stream code involves many more operations and the duration of the task of addressing to the global memory is not a significant part of the total kernel execution time. This is why the two-stream speed-up is higher than that for the single scattering code.

For total ozone retrieval $N_{do} = 4$–8 discrete ordinates per hemisphere are chosen for simulations of scattered sunlight in the UV spectral range. The dimensions of matrices involved in the computations are mostly $N_{do} \times N_{do}$. Our numerical simulations regarding basic matrix operations evidence that for matrix sizes 8×8 the highest performance is achieved when all arrays required for the RTM solver are placed into registers. Speed-up factors are plotted as functions of the number of discrete ordinates in Fig. 3-31. The speed-up for $N_{do} = 16$ is less than that for $N_{do} = 4$. With a low number of discrete ordinates, the kernel consumes a small number of registers, and so a large number of kernels can run simultaneously and the occupancy of the GPU is high.
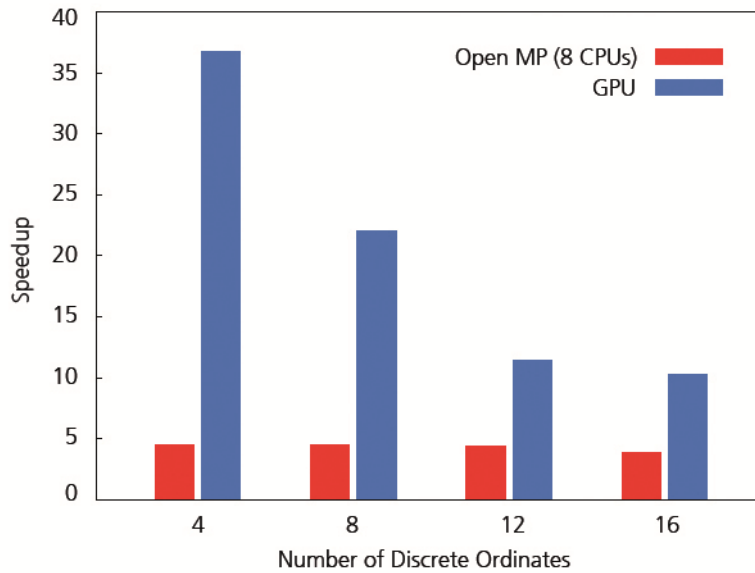
Fig.3-31: Speed-up of the GPU-implemented DOM with the matrix operator technique compared to sequential CPU code execution.

The CUDA implementation of the multi-stream model shows a speed-up of almost 22 compared to sequential CPU execution for computations involving 8 discrete ordinates, and a value of ~35 for 4 discrete ordinates.

The trade-off between development efforts and achievable performance should be taken into account, as it is challenging to develop additional functionality to code optimized for GPU platforms. Based on current limitations regarding the use of double-precision arithmetic, register memory size and data transfer latency, it must be said that as of today, GPU-based programming cannot provide a comprehensive substitute for conventional CPU-based RTM codes in the UV spectral range. However, the combined use of GPUs and CPUs can yield significant performance enhancement. The details of implementation of the discrete ordinate method on GPUs can be found in *Efremenko et al. (2014)*.

References

Stamnes, K., Tsay, S.C., Wiscombe, W., Jayaweera, K.: Numerically stable algorithm for discrete-ordinate-method radiative transfer in multiple scattering and emitting layered media. Appl. Opt., 12, 2502-2509, 1988.

Efremenko, D.S., Loyola, D.G., Doicu, A., Spurr, R.J.D.: Multi-core-CPU and GPU-accelerated radiative transfer models based on the discrete ordinate method. Computer Physics Communications, 185(12), 3079-3089, 2014.

4. Atmospheric Remote Sensing – Applications

4.1 The WMO Ozone Assessment 2014 – The Ozone Hole will Close in the Second Half of the 21st Century

D. Loyola, M. Coldewey-Egbers, M. Gottwald

The World Meteorological Organization (WMO) issues on a 4-year basis the *Scientific Assessment of Ozone Depletion*, a report for decision-makers compiling our current knowledge about the status and the future of the ozone layer. A wide range of experts, including scientists from our department and DLR's Institute of Atmospheric Physics (IPA), contributed to the report.

Spaceborne measurements of stratospheric ozone
One of the basic information required for understanding the evolution of stratospheric ozone stems from spaceborne trace gas measurements. Since 1995, when GOME, the first European sensor for atmospheric sounding, was lifted into space onboard the ERS-2 platform, we are actively involved in retrieving trace gas concentrations from passive UV-VIS-NIR-SWIR instruments. GOME delivered data between 1995 and 2011. It was complemented from 2002 to 2012 by the German-Dutch-Belgian spectrograph SCIAMACHY on ENVISAT. Currently two GOME-2 sensors, enhanced versions of GOME, orbit the Earth on sun-synchronous polar orbits. The first is part of MetOp-A, launched in 2006, the second of MetOp-B, launched in 2012. We also have access to the earlier record of spaceborne measurements which date back until 1979, the year which saw the first TOMS instrument aboard the Nimbus 7 satellite. Thus our analyses are based on 20 years of data from European sensors with 16 more years delivered by NASA instruments (Fig. 4-1).

Comparison between different European and North American satellite measurements as well as ground-based instruments show an excellent agreement (*Weber et al. 2014*). The homogenized GOME-type total ozone-essential climate variable (GTO-ECV) dataset generated at IMF in cooperation with BIRA and RTS in the framework of the ESA Climate Change Initiative reached an unprecedented agreement with the latest NASA SBUV data, the average differences in total ozone between these two satellite dataset vary between only –0.3% and 0.8% (*Chiou et al. 2014*).

The GOME-2 sensors are presently our workhorse. They are operated in tandem configuration with both measuring vertical and horizontal trace gas distributions providing a global coverage on a daily basis. A third GOME-2 spectrograph is planned to be launched in 2018. Shortly afterwards, from about 2020 on, the EU Copernicus missions Sentinel 4 (S4) and Sentinel 5 (S5) shall form the backbone of European spaceborne atmospheric sounding in the coming decade. In order to prepare for the very high data volumes offered by these programs, ESA will "insert" the Sentinel 5 Precursor (S5P) mission in 2016. It will permit to develop the retrieval and processing capabilities required for the much higher data volumes of the atmospheric Sentinel missions. Due to its paramount spatial resolution, S5P and S5 will permit to trace air pollution even on the level of urban quarters while S4, with its hourly measurements over Europe, will provide insights into the dynamics of trace gas sources and sinks.

Chemistry-climate models and satellite observations
Predictions how the ozone layer will evolve require reliable computer models simulating the physical, dynamic and chemical processes in the atmosphere. Such models, derived at the DLR Institute of Atmospheric Physics, are validated when their results are confronted with the actual ozone measurements. This comparison provides indications about the quality of the applied model and thus allows to judge how well the results describe the future evolution of the ozone layer. On one side the current model simulations reach back until the period in the past century when stratospheric ozone depletion did not yet exist. At the other end they can predict ozone concentration up to the end of the current century. Recent collaborative work between IMF and IPA has already demonstrated that trace gas measurements and model predictions are in good agreement (see, e.g., annual report 2011).

Climate change and ozone layer
The present stable size of the ozone hole in Antarctic winter shows that the reduction of chlorofluorocarbons (CFCs) as agreed in the Montreal Protocol from 1987 begins to ban ozone depleting substances from the stratosphere over Antarctica. This will lead to shrinking ozone holes during the corresponding season and finally a recovery of the ozone layer. However, in addition to the

reduction of chlorofluorocarbons, climate change will increasingly impact stratospheric ozone. It could even lead to a so-called "over-recovery" in some regions. "Over-recovery" means that after the complete disappearance of CFCs, ozone concentrations in some regions could increase to levels that are even higher than they were before the first noted occurrence of the ozone hole in the early 1980s. This is due to changes in the amount of climate relevant trace gases, especially carbon dioxide (CO_2), methane (CH_4) and nitrous oxide (N_2O). It is predicted that increasing concentrations of CO_2 and CH_4 will strengthen the global ozone layer, whereas increasing N_2O concentrations will lead to ozone reduction. In sum, these effects will lead to a thicker ozone layer outside tropical regions from the middle of this century. In the tropics, by contrast, the ozone layer will become thinner in the second half of the 21st century. This is because, in addition to chemical processes, scientists expect climate change to alter vertical airstreams, significantly influencing ozone distribution.
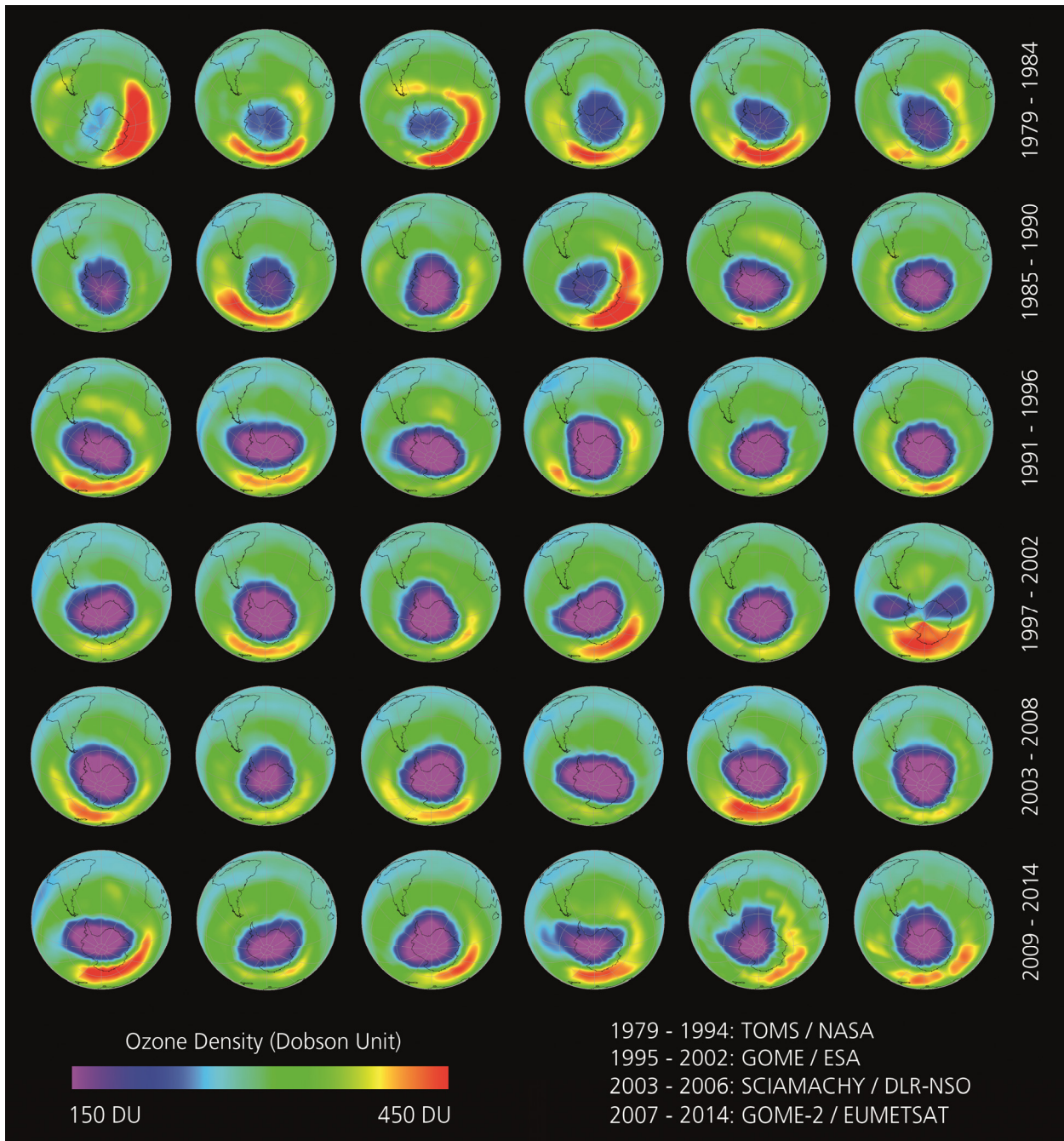

Fig. 4-1: Evolution of the Antarctic ozone hole in early October from 1979 (top left) to 2014 (bottom right). The measurements have been executed by the instruments and missions as indicated.

Regional and global trend analysis using the GTO-ECV data covering almost two decades show that the obvious increase of the total ozone in the tropics (Fig. 4-2 left panel) is a likely manifestation of a long-term change in El Niño Southern Oscillation intensity over the last two decades. However detecting mid- and longterm trends requires more time (Fig. 4-2 right panel). The expected mid-latitude onset of ozone recovery is still not significant and would need additional five years of observations to be unequivocally detectable (*Coldewey-Egbers et al. 2014*).

The status of the ozone layer, not only over Antarctica, seems to evolve in a rather interesting fashion in response to anthropogenic activities (banning of CFCs, emission of greenhouse gases) in the coming decades. Our spaceborne measurements can shed light on this.
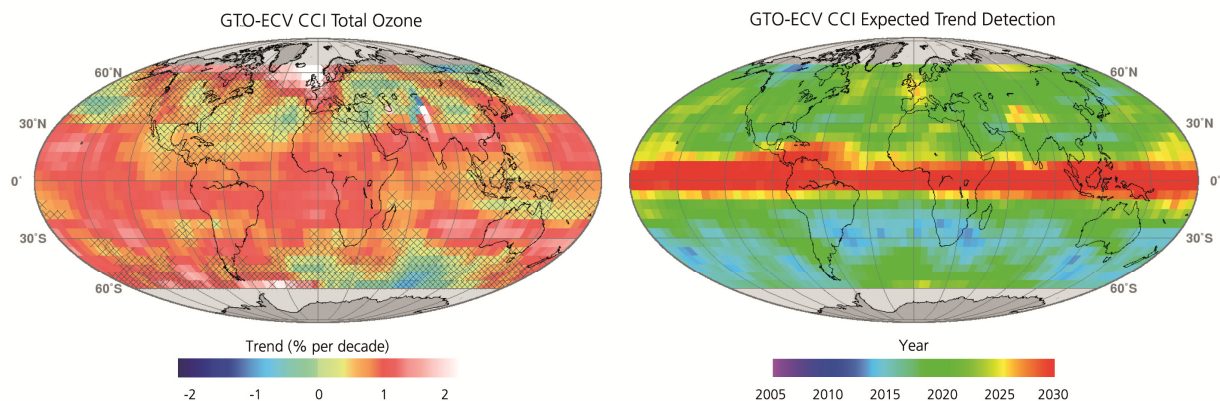
Fig. 4-2: Total ozone trend estimates 1995-2013 from satellite data GTO-ECV (left) with grey crosses denoting that the coefficients are not significant at the 95% confidence level, and estimated year of expected ozone trend detection (right). The images are from Coldewey-Egbers et al. (2014).

References

Chiou, E.W., Bhartia, P.K., McPeters, R.D., Loyola, D.G., Coldewey-Egbers, M., Fioletov, V.E., Van Roozendael, M., Spurr, R., Lerot, C., and Frith, S.M.: Comparison of profile total ozone from SBUV (v8.6) with GOME-type and ground-based total ozone for a 16-year period (1996 to 2011). Atmos. Meas. Tech., 7, 1681-1692, 2014.

Coldewey-Egbers, M., Loyola, D., Braesicke, P., Dameris, M., Van Roozendael, M., Lerot, C., Zimmer, W.: A new health check of the ozone layer at global and regional scales. Geophysical Research Letters, DOI: 10.1002/2014GL060212, 2014.

Weber, M., Steinbrecht, W., van der A, R., Coldewey-Egbers, M., Fioletov, V.E., Frith, S.M., Long, C.S., Loyola, D., Wild, J.D.: [Global Climate] Stratospheric ozone. In *State of the Climate in 2013* (Blunden, J., Arndt, D.S., Eds.), Bull. Amer. Meteor. Soc., 95, S38-S39, 2014.

4.2　The Eruption of the Bardarbunga Volcano in Iceland

P. Hedelt, P. Valks, D. Loyola

The Bardarbunga (Bárðarbunga) volcano is a stratovolcano under the Vatnajökull glacier, located in one of Iceland's remotest areas. After increased seismic activity in the second half of August 2014, it erupted on 31 August through fissure vents at the flanks of the volcano in the Holuhraun lava-field. The eruption has emitted large volumes of sulphur dioxide (SO_2) and impacted the air quality in Iceland. No significant amount of volcanic ash was produced such that air traffic remained unhampered, except for the immediate vicinity of the volcano. Currently, the activity of the volcano is continuing unabatedly. Even an explosive eruption of Bardarbunga cannot be ruled out. In that case large quantities of ash could be produced with potentially far-reaching consequences for the European air traffic.

Since 1 September 2014, GOME-2 aboard MetOp-A & B detected continuous emission of SO_2 with a total vertical column reaching partly more than 40 DU (Dobson Units). The SO_2 clouds were mainly transported eastwards over Scandinavia and Russia (Fig. 4-3). Some of them, however, spread out over Greenland and even reached North America. On 22 September 2014 a SO_2 cloud was moving over Germany and Austria and could be detected at the meteorological observatories located at Schneefernerhaus and Hohenpeissenberg (Fig. 4-4). Assuming that the SO_2 plume height was about 4 km, the GOME-2 measurements were in very good agreement with MAX-DOAS and Brewer measurements at Hohenpeissenberg at the same time (Fig. 4-5).
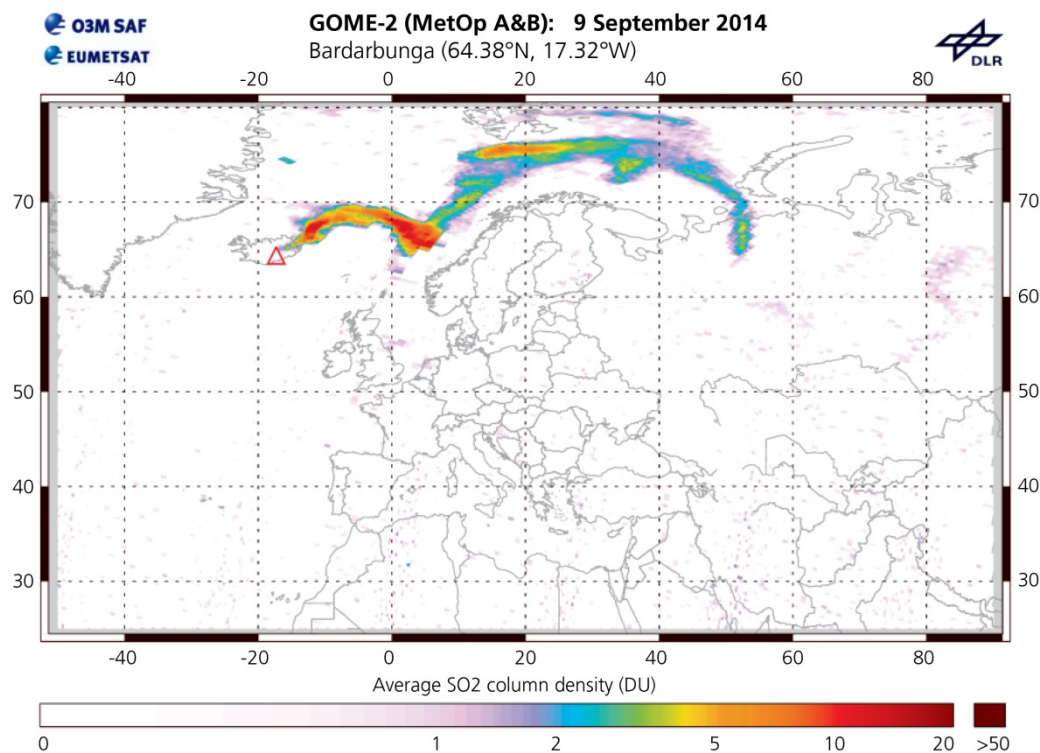
Fig. 4-3: GOME-2 SO_2 measurements above Europe regridded on a 0.1° × 0.1° grid (11 km × 11 km).

Under the leadership of IMF, DLR-EOC provides operational trace gas measurements, including total SO_2 columns in the framework of EUMETSAT's Satellite Application Facility on Ozone and Atmospheric Chemistry Monitoring (O3M-SAF). This occurs in near-realtime, i.e. within 2 hours of sensing. Users of the SO_2 product include the Volcanic Ash Advisory Centres (VAACs) for the purpose of issuing aviation warnings. Our SO_2 measurements serve as a proxy for the presence of volcanic ash. An increased awareness exists since the eruption of Iceland's Eyjafjallajökull volcano in April 2010 when air traffic over Central Europe came to a standstill. Studying and understanding the emission of SO_2 and associated ash in a volcanic eruption is of paramount importance for ensuring safe air transport but also minimizing the effects on air traffic.

GOME-2 (MetOp A&B): 22 September 2014
Hohenpeissenberg (47.48°N, 11.10°E)

SO2 column density (DU) - assumed plume height 15 km
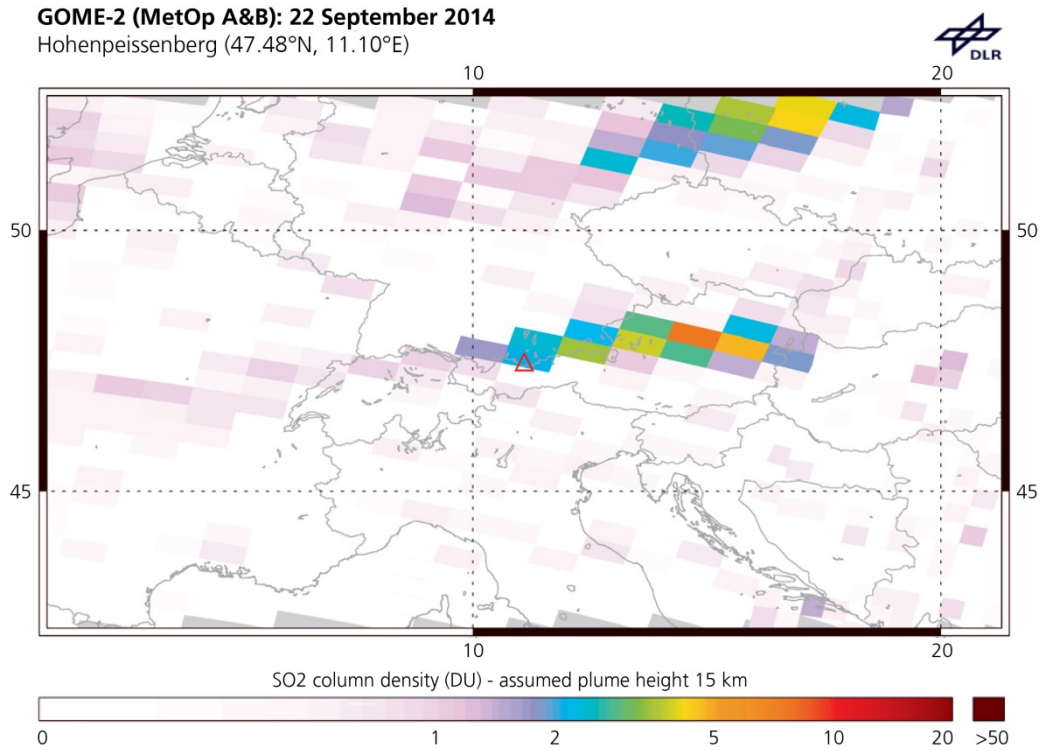
Fig. 4-4: GOME-2 measurement on 22 September 2014 showing an SO₂ cloud from the Bardarbunga eruption moving over southern Germany and Austria. The red triangle indicates the location of the meteorological observatory Hohenpeissenberg where measurements were taken.
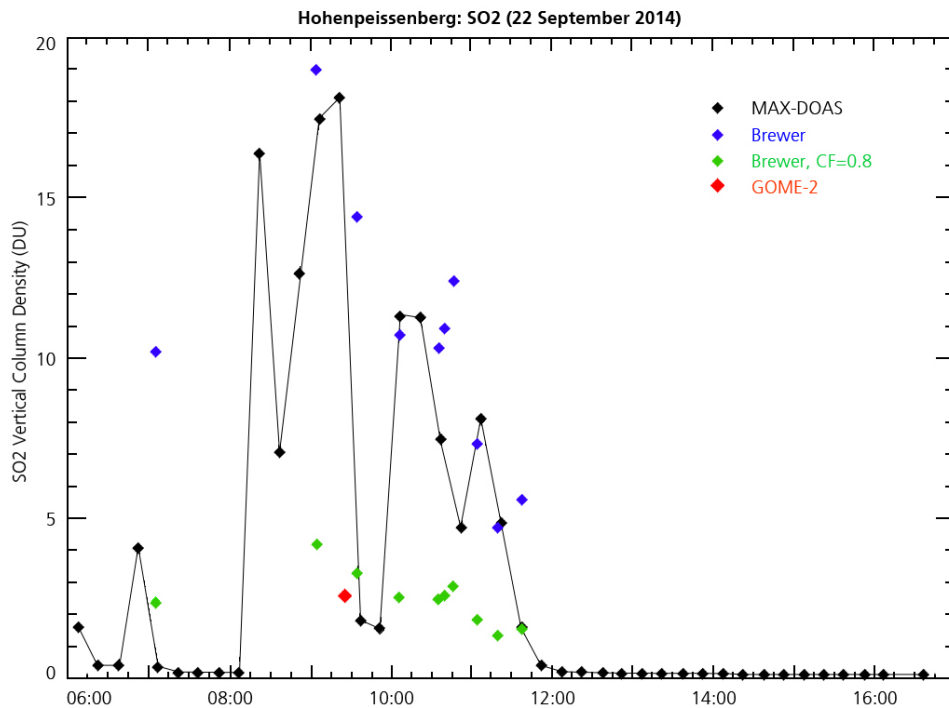
Fig. 4-5: Comparison of measurements of the SO₂ cloud over Germany on 22 September 2014. Results from the MAX-DOAS and Brewer instruments at Hohenpeissenberg are shown along with the GOME-2 SO₂ measurement at this location (red triangle in Fig. 4-4). The GOME-2 measurement has been calculated assuming an SO₂ plume located at 4 km. In order to compare ground-based measurements with the satellite-borne GOME-2 measurement the Brewer data has been weighted by the cloud-fraction over Hohenpeissenberg (CF=0.8) and a background SO₂ noise of 0.5 DU (green symbol).

4.3 A Study Based on Jacobians Matrices of the Atmospheres of M and G Earth-like Planets

M. Vasquez, F. Schreier, T. Trautmann

Correlation matrices of the Jacobians have been analyzed for Earth-like planets around G and M stars for various molecules, atmospheric temperatures and pressure (Fig. 4-6). The results of the spectra between 500 cm^{-1} and 1000 cm^{-1} show a high correlation between CO_2 and H_2O, since the Jacobians with respect to variations in CO_2 and H_2O content follow a similar pattern at regions outside the deep CO_2 absorption band at about 650 cm^{-1}. This is also the case of H_2O and surface temperature. However, an inspection of the Jacobians with respect to surface temperature shows that this one is orders of magnitude smaller and that emission spectra about the 15 μm CO_2 absorption band are not appropriate for surface temperature retrievals.

Higher correlations in the Jacobians of the atmospheric parameters have been found in the M star planets than in the G planet. These main differences arise from the temperature profile with missing inversion in the stratosphere of the M star planet. Nevertheless, a different spectral range may show different findings.
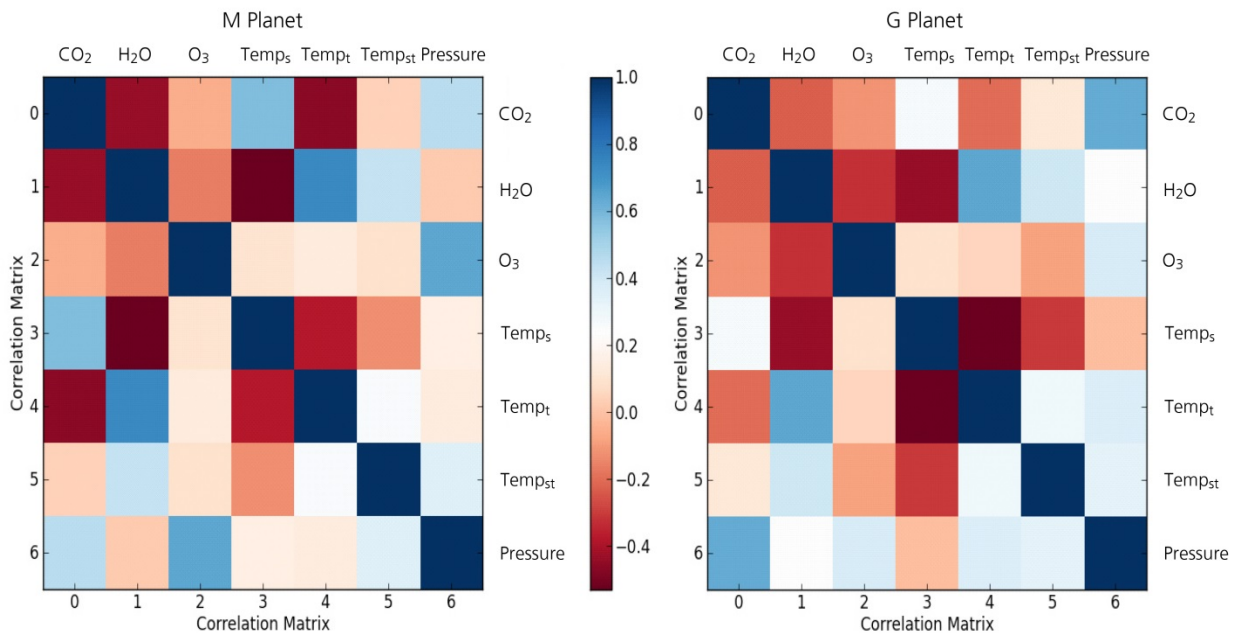

Fig. 4-6: Correlation matrices of the Jacobians of Earth-like planets around G and M stars for pressure, molecular species and surface (Temp$_s$), tropospheric (Temp$_t$), and stratospheric temperatures (Temp$_{st}$).

The inversion of atmospheric parameters from spectral observations is a nonlinear and ill-posed problem, and some sort of regularization is required in order to obtain a solution x with physical meaning. Note that the ill-posedness of a discrete equation is reflected by a large condition number $c(K)$ of the Jacobian matrix $K = dF/dx$, where $c(K) = \sigma_{max}/\sigma_{min}$, with σ_{max} and σ_{min} as the largest and smallest singular values of K, respectively. For this reason, a singular value decomposition analysis of the Jacobian matrix including different combination of parameters to be retrieved has been performed (Fig. 4-7).

A sensitivity study has also been conducted in order to assess the feasibility of retrieving CO_2 and H_2O molecular concentrations from an observed spectrum with a 1% noise level. Results indicate that from a measured spectrum with the mentioned noise level, it is possible to retrieve variations of 30 ppm and 10% CO_2 and H_2O. The perturbation values for the different atmospheric constituents are taken into account in the total amount of each molecular specie.

For some cases, the approximation of the Jacobians by finite differences is accurate enough. However, this approximation is sensitive to the perturbation step and it can lead to deviations to the actual Jacobians. For this reason, analytical Jacobians are preferred wherever they exist.
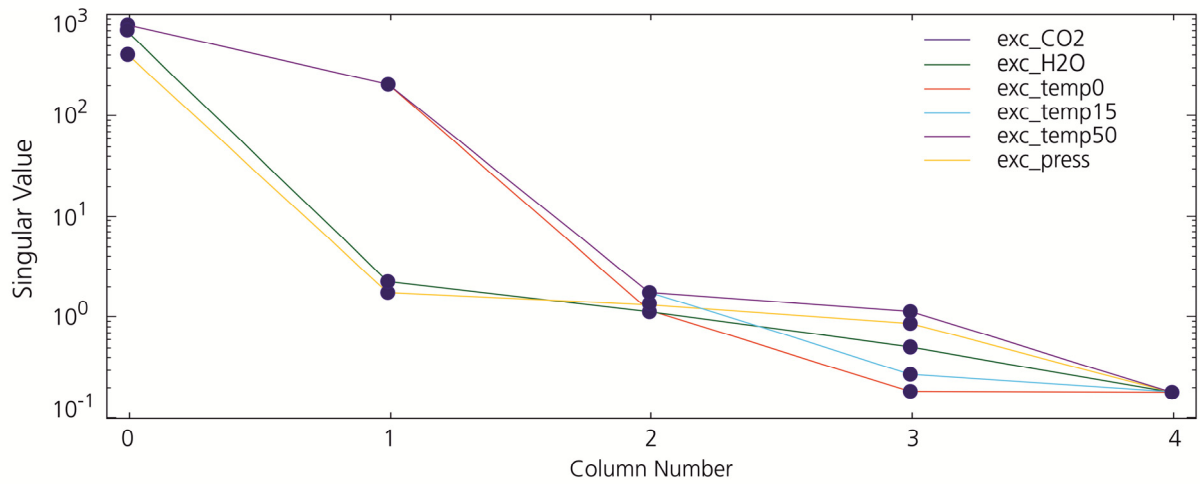
Fig. 4-7: Singular value decomposition for the Jacobian matrices of the G star planet.

Comparisons between numerical and analytical Jacobians have also been made for the G star planet. The numerical and analytical Jacobians for the ground temperature show a good agreement (Fig. 4-8). Correlation matrices between different atmospheric temperatures (at surface, troposphere, and stratosphere) calculated by analytical and numerical means demonstrate that correlations agree within a 1% percent difference. For correlations between surface and stratospheric temperatures the percent difference becomes larger with a value of 11%.
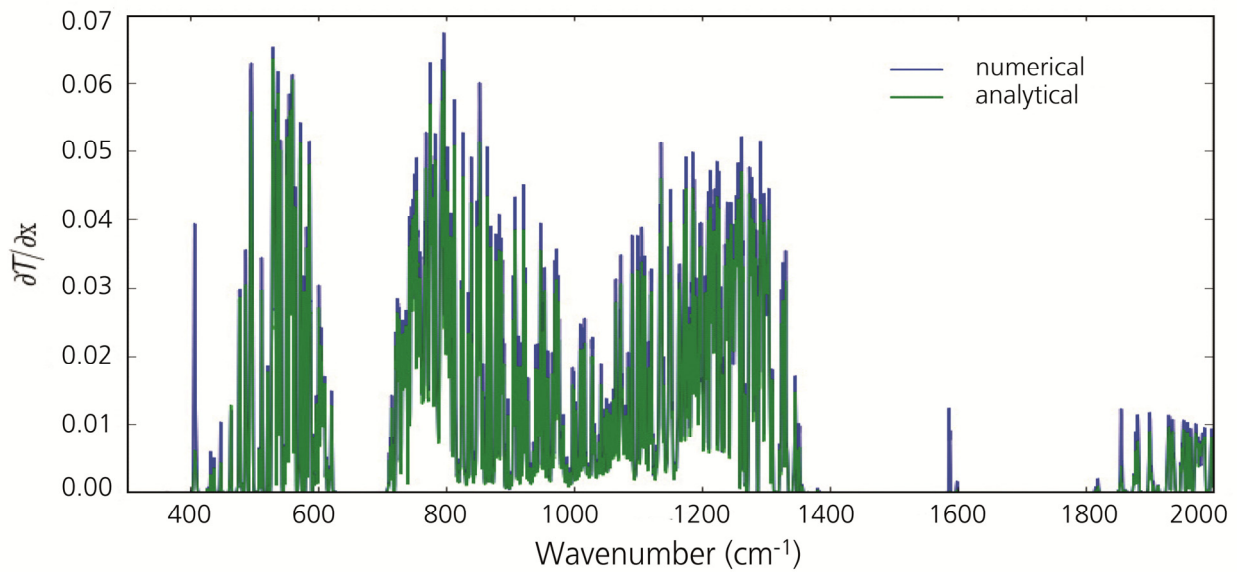
Fig. 4-8: Analytical and numerical Jacobian matrices for surface temperature.

The future step in this study is directed to use the modelled and observed spectra to obtain the true atmospheric properties applying the knowledge gained behind this sensitivity study. This is done through an inverse model that allows repetitive interactions between the spectra until a solution is found, i.e. an estimate of the true state of the atmosphere.

4.4 Mapping the Chemical Universe of Biomolecules for Astrobiology

M. Meringer, M. Ilardo (UCPH), J.T. Goodwin (Emory University), H.J. Cleaves (ELSI)

Understanding the origins of life is a central question of Astrobiology. Computer methods offer unique means to approach this challenge. There is strong evidence that biomolecules underwent a process of chemical evolution before life originated, and then a protracted period of biological evolution formed the universal genetic code shared by all extant terrestrial biology. The universal genetic code serves as an interface between informational biopolymers, ribonucleic acid (RNA) and deoxyribonucleic acid (DNA), and functional biopolymers, the proteins. The monomeric building blocks of proteins are amino acids; those of RNA are nucleotides, or deoxynucleotides in the case of DNA. In order to obtain a better understanding of the selection rules which guided chemical and early biochemical evolution, our approach is to computationally generate exhaustive sets of biomolecule analogues, to calculate their physico-chemical properties, and to simulate adaptive processes that might have led to the biochemical foundations of life as we know it.

Comprehensive libraries of amino acids had already been generated previously as part of a cooperative project with the University of Hawaii's NASA Astrobiology Institute (UHNAI) on "Creating a Reference Set of Amino Acids Structures for Use in Multiple Astrobiology Investigations" (see annual report 2012). We continued these research activities during four weeks' on-site collaboration at Tokyo Tech's Earth Life Science Institute (ELSI). We focused on two main directions:

- Extending the studies on the amino acid alphabet by analyzing the amino acid libraries prepared in *Meringer et al.* (*2013*).
- Enumerating alternative nucleotide structures by extending the methods used in *Meringer et al.* (*2013*) and analyses of the obtained libraries.

It is believed that size, hydrophobicity and charge are the three physico-chemical properties of amino acids most likely responsible for their selection during the evolution of the genetic code. An analysis of the first two of these properties had already been conducted as part of a master's thesis (*Ilardo 2013*) at UHNAI. During our collaboration at ELSI we acquired suitable software to calculate amino acid charge in terms of acid dissociation constants (pK_a values) of its functional groups. In this way we mapped a 1913-membered amino acid library into 3-dimensional space (Fig. 4-9). Subsequent statistical analysis confirmed that the set of the 20 genetically encoded amino acids covers this chemical space almost optimally in terms of range and evenness of these three physico-chemical properties. However, in contrast to previous results using much smaller comparison sets, now for the first time 20-membered sets being better than the encoded amino acids were found. This raises questions as to whether potential alien biochemistries using such alternative amino acid alphabets could outperform terrestrial life, e.g. in terms of protein folding capabilities. The results of these studies are under review at Nature Scientific Reports (*Ilardo et al. submitted*).
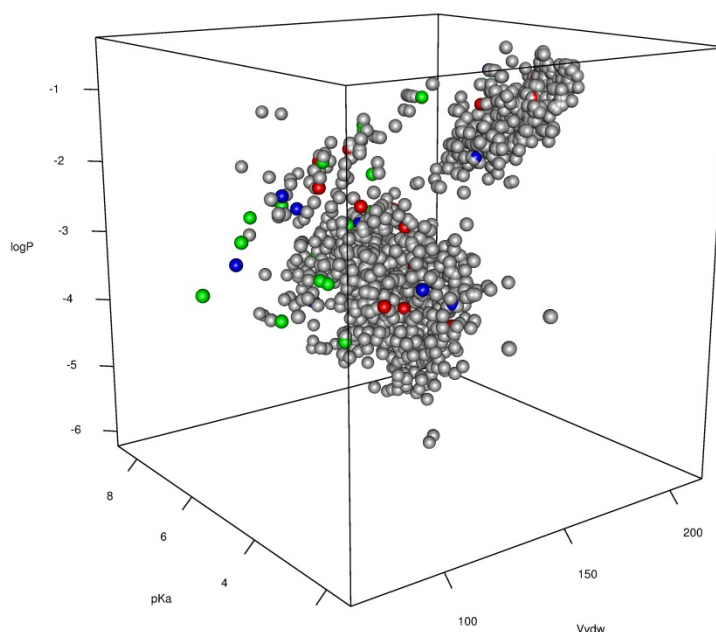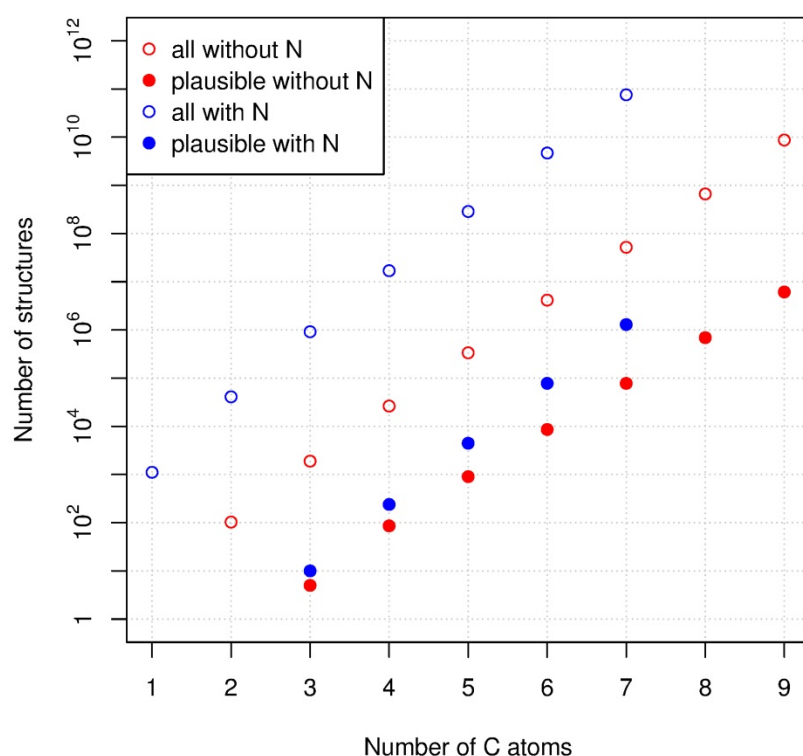

Fig. 4-9: Chemical space of amino acids, represented by size, hydrophobicity and charge in terms of Van der Waals volume V_{vdw}, partition coefficient logP and logarithmic dissociation constant pK_a. Green spheres represent the 20 coded amino acids, blue and red spheres show two of the rare better sets. The top-right cluster is formed by somewhat larger-sized aromatic compounds.

Another focus of our collaboration was the definition and generation of nucleotide analogue libraries. RNA plays a central role as the intermediary carrier of genetic information in transcription and translation. Given fundamental structural constraints, such as the ability to form complementary base-pairs and to be linked into a linear covalent polymer, a variety of structural isomers of RNA could potentially function as genetic platforms. Using structure generation software (*Meringer 2010*), all of the potential structural isomers of the natural ribosides ($C_5H_9O_4B$, where B is a nucleobase) that can potentially serve as building blocks of nucleic acids were enumerated. Database queries showed that only very few of these computed isomers had been described previously. Together with extensive studies about which physico-chemical properties might have led to the selection of β-ribofuranosylnucleosides over a multitude of alternative structures during evolution, these results have been submitted to Astrobiology (*Cleaves et al. submitted*). The structural space of nucleotides beyond $C_5H_9O_4B$ is the object of ongoing studies (Fig. 4-10).

Fig. 4-10: Numbers of nucleotide analogue structures as a function of the number of carbon atoms in the molecule. Enumeration is based on the formula spaces $C_{nH5-(2n+1)}O_{2-4}B$ in absence of N and $CnH5-(2n+3)N1-2O0-4B$ with N. As was observed in the amino acid libraries, there is an exponential growth in the number of structures with increasing number of C atoms, and a considerable discrepancy (by a factor of 103-105) in the corresponding numbers of mathematically possible and chemically plausible structures.

References

Cleaves, H.J., Meringer, M., Goodwin, J.T.: 227 Views of RNA: Is RNA Unique in Its Chemical Isomer Space? Submitted to Astrobiology.

Ilardo, M.: Natural Selection and the Amino Acid Alphabet, Master's Thesis, University of Hawaii, 2013.

Ilardo, M., Meringer, M., Freeland, S.J., Rasulev, B., Cleaves, H.J.: Extraordinarily Adaptive Properties of the Genetically Encoded Amino Acids, Submitted to Nature Scientific Reports.

Meringer, M.: Structure Enumeration and Sampling, Handbook of Chemoinformatics Algorithms, Edited by J.-L. Faulon and A. Bender, Chapman & Hall: 233-267, 2010.

Meringer, M., Cleaves, H.J. and Freeland, S.J.: Beyond Terrestrial Biology: Charting the Chemical Universe of α-Amino Acid Structures, J. Chem. Inf. Model. 53(11): 2851-2862, 2013.

5. Documentation

5.1 Books and Book Contributions

Ferrucci, F., Theys, N., Clarisse, L., Hirn, B., Laneve, G., Valks, P., Van Der A, R., Tait, S., Di Bartola, C., Brenot, H.: Operational integration of space borne measurements of Lava discharge rates and Sulphur Dioxide concentrations for Global Volcano Monitoring. In: Early Warning for Geological Disasters: Scientific Methods and Current Practice, Advanced Technologies in Earth Sciences. Springer, 307-331, ISBN 978-3-642-12232-3, 2014

5.2 Journal Papers

Alam, K., Trautmann, T., Blaschke, T., Subhan, Fazli: Changes in aerosol optical properties due to dust storms in the Middle East and Southwest Asia. Remote Sensing of Environment, 143, 216-227, Elsevier, DOI: 10.1016/j.rse.2013.12.021, 2014

Brenot, H., Theys, N., Clarisse, L., van Geffen, J., van Gent, J., Van Roozendael, M., van der A, R., Hurtmans, D., Coheur, P.-F., Clerbaux, C., Valks, P., Prata, F., Rasson, O., Sievers, K., and Zehner, C.: Support to Aviation Control Service (SACS): an online service for near real time satellite monitoring of volcanic plumes. Nat. Hazards Earth Syst. Sci. 14, 1099-1123, 2014

Chiou, E.W., Bhartia, P.K., McPeters, R.D., Loyola, D.G., Coldewey-Egbers, M., Fioletov, V.E., Van Roozendael, M., Spurr, R., Lerot, C., Frith, S.M.: Comparison of profile total ozone from SBUV (v8.6) with GOME-type and ground-based total ozone for a 16-year period (1996 to 2011). Atmospheric Measurement Techniques, 7, 1681-1692, DOI: 10.5194/amt-7-1681-2014, 2014

Coldewey-Egbers, M., Loyola, D., Braesicke, P., Dameris, M., Van Roozendael, M., Lerot, C., Zimmer, W.: A new health check of the ozone layer at global and regional scales. Geophysical Research Letters, 41, 4363-4372, DOI: 10.1002/2014GL060212, 2014

Doicu, A., Efremenko, D., Loyola, D., Trautmann, T.: Approximate models for broken clouds in stochastic radiative transfer theory. Journal of Quantitative Spectroscopy and Radiative Transfer, 145, 74-87, Elsevier, DOI: 10.1016/j.jqsrt.2014.04.025, 2014

Doicu, A., Efremenko, D., Loyola, D., Trautmann, T.: Discrete ordinate method with matrix exponential for stochastic radiative transfer in broken clouds. Journal of Quantitative Spectroscopy and Radiative Transfer, 138, 1-16, Elsevier, DOI: 10.1016/j.jqsrt.2014.01.011, 2014

Efremenko, D., Loyola, D., Doicu, A., Spurr, R.: Multi-core-CPU and GPU-accelerated radiative transfer models based on the discrete ordinate method. Computer Physics Communications, 185 (12), 3079-3089, Elsevier, DOI: 10.1016/j.cpc.2014.07.018, 2014

Efremenko, D., Loyola, D., Spurr, R., Doicu, A.: Acceleration of radiative transfer model calculations for the retrieval of trace gases under cloudy conditions. Journal of Quantitative Spectroscopy and Radiative Transfer, 135, 58-65, Elsevier, DOI: dx.doi.org/10.1016/j.jqsrt.2013.11.014, 2014

Efremenko, D., Doicu, A., Loyola, D., Trautmann, T.: Optical property dimensionality reduction techniques for accelerated radiative transfer performance: Application to remote sensing total ozone retrievals. Journal of Quantitative Spectroscopy and Radiative Transfer, 133, 128-135, Elsevier, DOI: 10.1016/j.jqsrt.2013.07.023, 2014

Grossi, M., Valks, P., Loyola, D., Aberle, B., Slijkhuis, S., Wagner, T., Beirle, S., Lang, R.: Total column water vapour measurements from GOME-2 MetOp-A and MetOp-B. Atmospheric Measurement Techniques Discussions, 7, 3021-3073, DOI: doi:10.5194/amtd-7-3021-2014, 2014

Hao, N., Koukouli, M., Inness, A., Valks, P., Loyola, D., Zimmer, W., Balis, D., Zyrichidou, I., Van Roozendael, M., Lerot, C., Spurr, R.: GOME-2 total ozone columns from MetOp-A/MetOp-B and

assimilation in the MACC system. Atmospheric Measurement Techniques, 7, 2937-2951, Copernicus Publications, DOI: 10.5194/amt-7-2937-2014, 2014

Kalakoski, N., Kujanpää, J., Sofieva, V., Tamminen, J., Grossi, M., Valks, P.: Comparison of GOME-2/MetOp total column water vapour with ground-based and in situ measurements. Atmospheric Measurement Techniques Discussions, 7, 12517-12543, DOI: doi:10.5194/amtd-7-12517-2014, 2014

Lerot, C., Van Roozendael, M., Spurr, R., Loyola, D., Coldewey-Egbers, M., Kochenova, S., van Gent, J., Koukouli, ML., Balis, D., Lambert, J.-C., Granville, J., Zehner, C.: Homogenized total ozone data records from the European sensors GOME/ERS-2, SCIAMACHY/Envisat, and GOME-2/MetOp-A. Journal of Geophysical Research: Atmospheres, 119 (3), 1639-1662, DOI: 10.1002/2013JD020831, 2014

Schreier, F., Gimeno-García, S., Hedelt, P., Hess, M., Mendrok, J., Vasquez, M., Xu, J.: GARLIC - A General Purpose Atmospheric Radiative Transfer Line-by-Line Infrared Code: Implementation and Evaluation. Journal of Quantitative Spectroscopy and Radiative Transfer, 137, 29-50, Elsevier, DOI: 10.1016/j.jqsrt.2013.11.018, 2014

Schüssler, O., Loyola, D., Doicu, A., Spurr, R.: Information Content in the Oxygen A-Band for the Retrieval of Macrophysical Cloud Parameters. IEEE Transactions on Geoscience and Remote Sensing, 52 (6), 3246-3255, IEEE Geoscience and Remote Sensing Society, DOI: 10.1109/TGRS.2013.2271986, 2014

Spinetti, C., Salerno, G., Caltabiano, T., Carboni, E., Clarisse, L., Corradini, S., Hedelt, P., Koukouli, M.E., Merucci, L., Siddans, R.,Tampellini, L., Theys, N., Valks, P. and C. Zehner, C.: Volcanic SO2 by UV-TIR satellite retrievals: validation by using ground-based network at Mt. Etna. Annals of Geophysics, Fast Track 2, 57, DOI: 10.4401/ag-6641, 2014

Valks, P., Hao, N., Gimeno García, S., Loyola, D., Dameris, M., Jöckel, P., Delcloo, A.: Tropical tropospheric ozone column retrieval for GOME-2. Atmospheric Measurement Techniques, 7, 2513-2530, DOI: 10.5194/amt-7-2513-2014, 2014

Weber, M., Steinbrecht, W., van der A, R., Coldewey-Egbers, M., Fioletov, V.E., Frith, S., Long, C., Loyola, D., Wild, J.D.: [Global Climate] Stratospheric ozone. In State of the Climate in 2013 (Blunden, J., Arndt, D.S., Eds.), Bull. Amer. Meteor. Soc., 95, S38-S39, 2014

5.3 Conference Proceeding Papers and Presentations

Coldewey-Egbers, M., Loyola, D., Braesicke, P., Dameris, M., Van Roozendael, M., Lerot, C., and Zimmer, W.: Global spatially resolved total ozone variability and trend patterns obtained from comprehensive European satellite date sets. EUMETSAT Meteorological Satellite Conference, Geneva, Switzerland, 2014

Efremenko, D., Doicu, A., Loyola, D., Trautmann, T.: Fast and accurate techniques of treating the radiative transfer problem under cloudy conditions. COSPAR 40th Scientific Assembly, Moscow, Russia, 2014

Efremenko, D., Loyola, D., Doicu, A., Spurr, R.: Multi-core-CPU and GPU-accelerated radiative transfer models used for trace gas retrieval. In: Proceedings of the 2014 conference on Big Data from Space (BiDS'14), 259-262, Publications Office of the European Union, Big Data From Space (BiDS'14), Frascati, Italy, DOI: 10.2788/1823. ISBN 978-92-79-43252-1, 2014

Gimeno García, S., Loyola, D., Romahn, F., Lutz, R.: Retrieval of Cloud Height and Cloud Albedo from GOME-2 using the new ROCINN algorithm. EUMETSAT Meteorological Satellite Conference, Geneva, Switzerland, 2014

Gimeno García, S., Trautmann, T., Heinze, R., Loyola, D., Rohman, F., Hedelt, P., Schüssler, Olena, Schreier, F.: Effects of cloud variability on TROPOMI molecular and cloud property products. COSPAR 40th Scientific Assembly, Moscow, Russia, 2014

Godolt, M., Gebauer, S., Grenfell, J.L., Hedelt, P., Kitzmann, D., Kunze, M., Langematz, U., von Paris, P., Patzer, B., Rauer, H., Stracke, B.: Influence of the central star type on the atmospheres of habitable exoplanets. Towards Other Earths II, Porto, Portugal, 2014

Gottwald, M.: Mars - unser Roter Nachbar. Public lecture, Munich, Germany, 2014

Gottwald, M.: DLR's Earth Observation Center and Spaceborne Remote Sensing of Impact Structures. Geoscience Colloquium, Albert-Ludwigs-Universität, Freiburg, Germany, 2014

Gottwald, M.: The TanDEM-X Radar Mission and terrestial impact structures. Seminar for Meteorite and Impact Research, Museum für Naturkunde / Humboldt-Universität, Berlin, Germany, 2014

Gottwald, M., Fritz, T., Breit, H., Schättler, B., Harris, A.: The TanDEM-X Digital Elevation Model and Terrestrial Impact Craters. COSPAR 40th Scientific Assembly, Moscow, Russia, 2014

Gottwald, M.: Einschlagskrater - Zeugen kosmischer Kollisionen. Public lecture, Munich, Germany, 2014

Grenfell, J.L., Tabataba-Vakili, F., Grießmeier, J.M., von Paris, P., Patzer, B., Lammer, H., Stracke, B., Gebauer, S., Schreier, F., Rauer, H.: Response of Biomarkers to NOx induced from Stellar Cosmic Rays for Earth-like Planets in the HZ of M-Dwarf Stars. Search for Life beyond the Solar System, Tucson, Arizona, USA, 2014

Hamidouche, M., Trautmann, T., Gottwald, M., Lichtenberg, G.: Long Term Monitoring of the new MERLIN Lidar Instrument. Copernicus, EGU General Assembly 2014, Vienna, Austria, 2014

Hamidouche, M., Trautmann, T., Gottwald, M., Lichtenberg, G.: The new MERLIN Lidar Instrument: Science & Long Term Monitoring. Earth Science and Climate Change, San Francisco, CA, USA, 2014

Hamidouche, M.: Infrared Astronomy and SOFIA. CCG Seminar Infrarottechnik Grundlagen, Trends, moderne Anwendungen. Wessling, Germany, 2014

Hao, N, Koukouli, M., Inness, A., Valks, P., Loyola, D., Zimmer, W., Balis, D., Zyrichidou, I., Van Roozendael, M, Lerot, C., Spurr, R.: GOME-2 total ozone columns from MetOp-A/MetOp-B and assimilation in the MACC system. EUMETSAT Meteorological Satellite Conference, Geneva, Switzerland, 2014

Hao, N., Van Roozendael, M., Ding, A.J., Zhou, B., Hendrick, F., Shen, Y.C., Wang, T., Valks, P.: Retrieval of tropospheric NO2 vertical column densities and aerosol optical properties from MAXDOAS measurements in Yangtze River Delta, China. Copernicus, EGU General Assembly 2014, Vienna, Austria, 2014

Hao, N., Valks, P., Hedelt, P., Grossi, M., Zimmer, W., Loyola, D.: Improvement of retrieval algorithm for GOME-type instrument. Dragon 3 Mid-term Results Symposium, Chengdu, China, 2014

Hess, M., Koepke, P., Schreier, F., Trautmann, T.: The aerosol model OPAC - contents and new software. GEISA Workshop 2014: Towards a new vision of spectroscopic databases, Paris, France, 2014

Lutz, R., Loyola, D., Gimeno García, S., Lang, R.: Cloud fraction determination from GOME-2 on MetOp-A/B using the OCRA algorithm. EUMETSAT Meteorological Satellite Conference, Geneva, Switzerland, 2014

Lutz, R., Loyola, D., Gimeno García, S.: Cloud fraction determination for OMI using the OCRA algorithm. OMI Science Team Meeting 18, Utrecht, Netherlands, 2014

Meringer, M.: Chemoinformatics for Astrobiology: The Generation of Structural Formulas and Its Applications. ELSI Seminar, Tokyo, Japan, 2014

Meringer, M., Cleaves, H.J., Freeland, S.J.: Generation of Virtual Amino Acid Libraries for Multiple Applications in Astrobiology. The 2nd ELSI International Symposium, Tokyo, Japan, 2014

Schmidt, D., Gimeno García, S., Schreier, F.: Impact of Spectroscopic Line Parameters on Carbon Monoxide Column Density Retrievals from Shortwave Infrared Nadir Observations. 2nd Stakeholder Workshop on Traceability of Spectral Reference Line Data, Braunschweig, Germany, 2014

Schreier, F., Gimeno García, S., Milz, M., Kottayil, A.: ARTS - GARLIC - KOPRA – A LbL Model Intercomparison. Open ARTS Community Workshop 2014, Kristineberg Marine Research Station, Sweden, 2014

Schreier, F.: Atmosphärische Fernerkundung, Strahlungstransport und Inversion. CCG Seminar Infrarottechnik Grundlagen, Trends, moderne Anwendungen. Wessling, Germany, 2014

Valks, P., Hao, N., Hedelt, P., Loyola, D., and Inness, A.: Operational GOME-2 trace gas column observations for MACC-II. MACC-II Open Science Conference, Brussels, Belgium, 2014

Valks, P., N. Hao, N., Begoin, M., Heue, K.-P., Loyola, D., Pinardi, G., De Smedt, I., Van Roozendael, M., Delcloo, A.: Tropospheric trace gas column observations from GOME-2 for air quality applications. EUMETSAT Meteorological Satellite Conference, Geneva, Switzerland, 2014

Vasquez, M., Schreier, F., Gimeno-García, S., Hedelt, P., Trautmann, T.: Inverse problems in space remote sensing: A sensitivity study on the atmospheres of Earth-like exoplanets. European Planetary Science Congress 2014, Cascais, Portugal, 2014

5.4   Attended Conferences

MACC-II Open Science Conference, Brussels, Belgium, 27-30 January 2014

OMI Science Team Meeting 18, Utrecht, The Netherlands, 11-13 March 2014

The 2nd ELSI International Symposium, Tokyo, Japan, 24-26 March 2014

ELSI Seminar, Tokyo, Japan, 8 April 2014

Dragon 3 Mid-term Results Symposium, Chengdu, China, 26-29 April 2014

European Geosciences Union General Assembly, Vienna, Austria, 27 April - 2 May 2014

GEISA Workshop 2014: Towards a new vision of spectroscopic databases, Paris, France, 3-4 June 2014

Open ARTS Community Workshop 2014, Kristineberg Marine Research Station, Sweden, 9-11 June 2014

Earth Science and Climate Change, San Francisco, CA, USA, 28-30 July 2014

COSPAR 40th Scientific Assembly, Moscow, Russia, 2-10 August 2014

European Planetary Science Congress 2014, Cascais, Portugal, 8-12 September 2014

EUMETSAT Meteorological Satellite Conference, Geneva, Switzerland, 22-26 September 2014

GEWEX Water Vapour Assessment (G-VAP) Workshop, Institute for Space Sciences, Free University of Berlin, Berlin, Germany, 9-10 October 2014

2nd Stakeholder Workshop on Traceability of Spectral Reference Line Data, Braunschweig, Germany, 9-10 October 2014

Big Data From Space (BiDS'14), Frascati, Italy, 12-14 November 2014

5.5   Academic Degrees

Gimeno García, S.: Simulation of solar radiative transfer and comparison with spectro-radiometric measurements. Dissertation, Faculty of Physics and Earth Science, University of Leipzig. (Supervisor: Prof. Dr. T. Trautmann)

Schmidt, D.: Carbon Monoxide from SCIAMACHY Near Infrared Nadir Spectra: Impact of Retrieval Settings. Master of Science Thesis, Earth Oriented Space Science and Technology ESPACE, Technical University of Munich, October 2014. (Supervisors: Dr. F. Schreier and PD Dr. A. Doicu, Technical University of Munich)

Schüssler, O.: Combined Inversion Methods for UV/VIS Nadir Sounding. Dissertation, Civil Engineering and Surveying, Technical University of Munich. (Supervisors: Prof. Dr. Richard Bamler, PD Dr. A. Doicu and Dr. D. Loyola)

Song, L.: Retrieval and validation of aerosol and NO_2 profiles over Nanjing using Mini-MAX-DOAS instrument. Master of Science Thesis, Earth Oriented Space Science and Technology ESPACE, Technical University of Munich, November 2014. (Supervisors: Dr. Hao and PD Dr. A. Doicu)

Wang, Z.: MAX-DOAS observations of trace gases and aerosol from the Environmental Research Station Schneefernerhaus. Dissertation. (Supervisor: Dr. P. Valks)

Xu, J.: Inversion for Limb Infrared Atmospheric Sounding. Dissertation, Civil Engineering and Surveying, Technical University of Munich. (Supervisors: Prof. Dr. Richard Bamler, Dr. F. Schreier, and Prof. Dr. T. Trautmann)

5.6   Seminar Talks

K.-P. Heue: DOAS Measurements from Aircraft, 30 April 2014

M. Hamidouche: Interstellar Scintillation, 20 May 2014

M. Begoin: Ozone Depletion Events and Bromine Explosions - Transport processes in the polar boundary layer, 1 July 2014

P. Hedelt: Exoplanet Detectability and Spectral Features, 9 July 2014

D. Schmidt: Carbon Monoxide from SCIAMACHY Near Infrared Nadir Observations: Impact of Retrieval Settings, 6 October 2014

M. Vasquez: The GalileoMobile BraBo Expedition: A Journey Through the Amazons, 13 October 2014

P. von Paris (LAB Bordeaux): Characterization of (Non)Transiting Exoplanets with Optical Phase Curves, 22 October 2014

L. Song: Validation of Satellite Observations of NO_2 and Aerosol over China using Mini MAX-DOAS Instrument, 24 October 2014

Abbreviations and Acronyms

1D	1-dimensional
3D	3-dimensional
AAI	Aerosol Absorbing Index
AD	Algorithmic Differentiation
ADT	Asynchronous Data Transfer
AIRS	Atmospheric Infrared Sounder
ATCOR	Atmospheric & Topographic Correction
ATP	Atmosphärenprozessoren
BIRA	Belgisch Instituut voor Ruimte-Aëronomie
BIRRA	Beer Infrared Retrieval Algorithm
CAO-DISORT	Coupled Atmosphere-Ocean Discrete Ordinate Radiative Transfer
CBH	Cloud Base Height
CCD	Convective-Cloud-Differential
CDOP	Continuous Development and Operations Phase
CFC	Chlorofluorocarbon
CFR	Cloud Fraction
CPU	Central Processing Unit
CTH	Cloud Top Height
CTI	Configurable Transfer Item
CUDA	Compute Unified Device Architecture
DBPM	Dead and Bad Pixel Mask
DFD	Deutsches Fernerkundungsdatenzentrum
DLR	Deutsches Zentrum für Luft- und Raumfahrt
DNA	Deoxyribonucleic Acid
DOAS	Differential Optical Absorption Spectroscopy
DOM	Discrete Ordinate Method
DOME	Discrete Ordinate with Matrix Exponential
DU	Dobson Unit
ECMWF	European Centre for Medium-Range Weather Forecasts
ECV	Essential Climate Variable
ELSI	Earth-Life Science Institute
ENVISAT	Environmental Satellite
EOC	Earth Observation Center
ERS	European Remote Sensing Satellite
ESA	European Space Agency
EUMETSAT	European Organisation for the Exploitation of Meteorological Satellites
FD	Finite Difference
FPN	Fixed Pattern Noise
GARLIC	Generic Atmospheric Radiation Line-by-Line Infrared Code
GDP	GOME Data Processor
GEISA	Gestion et Etude des Informations Spectroscopiques Atmosphériques
GMES	Global Monitoring for Environment and Security
GOME	Global Ozone Monitoring Experiment
GOSAT	Greenhouse Gases Observing Satellite
GPU	Graphical Processor Unit
GTO	GOME-type Total Ozone
GWA	Global Atmosphere Watch
HALO	High Altitude and Long Range Research Aircraft
HITRAN	High Resolution Transmission
HK	Housekeeping
IASI	Infrared Atmospheric Sounding Interferometer
IMF	Institut für Methodik der Fernerkundung
IPA	Institut für Physik der Atmosphäre
ISODATA	Iterative Self-Organizing Data Analysis Technique

IUP-IFE	Institut für Umweltphysik / Institut für Fernerkundung
LIDORT	Linearized Discrete Ordinate Radiative Transfer
LO	Local Oscillator
LWC	Liquid Water Content
MB	Megabyte
MACC	Monitoring Atmospheric Composition and Climate
MAX-DOAS	Multi-Axis DOAS
MetOp	Meteorological Operational Polar Satellites of EUMETSAT
MLS	Microwave Limb Sounder
MoCaRT	Monte Carlo Radiative Transfer
MOPITT	Measurements of Pollution in the Troposphere
MPI	Message Passing Interface
MTP	Microwave Temperature Profiler
NASA	National Aeronautics and Space Administration
NCEP	National Centers for Environmental Prediction
NIR	Near-Infrared
NRT	Near-realtime
O3M	Ozone Monitoring
OCRA	Optical Cloud Recognition Algorithm
OMI	Ozone Monitoring Instrument
ORR	Operational Readiness Review
PALM	Parallelized Large-Eddy-Simulation Model
PBL	Planetary Boundary Layer
PDGS	Payload Data Ground Segment
PILS	Profile Inversion for Limb Sounding
PM	Pinned Memory
PMD	Polarization Measurement Device
PSTAR	vector version of System for Transfer of Atmospheric Radiation
RNA	Ribonucleic Acid
ROCINN	Retrieval of Cloud Information using Neural Networks
ROLO	Robotic Lunar Observatory
RT	Radiative Transfer
RTE	Radiative Transfer Equation
RTM	Radiative Transfer Model
RTS	RT Solutions
S5	Sentinel 5
S5P	Sentinel 5 Precursor
SAA	South Atlantic Anomaly
SACS	Support to Aviation Control Service
SAF	Satellite Application Facility
SBUV	Solar Backscatter Ultraviolet
SCD	Slant Column Density
SCIAMACHY	Scanning Imaging Absorption Spectrometer for Atmospheric Chartography
SCIATRAN	radiative transfer model for SCIAMACHY
SHDOM	Spherical Harmonic Discrete Ordinate Method
SOST	SCIAMACHY Operations Support Team
SQWG	SCIAMACHY Quality Working Group
SRON	Netherlands Institute for Space Research
STK	Satellite Toolkit
SVWF	Spherical Vector Wave Function
SWIR	Shortwave Infrared
SZA	Sun Zenith Angle
TELIS	TeraHertz Limb Sounder
TOC	Total Ozone Column
TOMS	Total Ozone Mapping Spectrometer
TROPOMI	Tropospheric Ozone Monitoring Instrument

UCPH	University of Copenhagen
UHNAI	University of Hawaii NASA Astrobiology Institute
UPAS	Universal Processor for UV/VIS Atmospheric Spectrometers
USGS	Unites States Geological Survey
UV	Ultraviolet
VAAC	Volcanic Ash Advisory Center
VCD	Vertical Column Density
VIS	Visible
VLIDORT	Vectorized Linear Discrete Ordinate Radiative Transfer
VRTE	Vector Radiative Transfer Equation
VSHDOM	Vector SHDOM
WMO	World Meteorological Organization
WOUDC	World Ozone and Ultraviolet Radiation Data Centre

DLR at a Glance

DLR is the national aeronautics and space research center of the Federal Republic of Germany. Its extensive research and development work in aeronautics, space, energy, transport and security is integrated into national and international cooperative ventures. In addition to its own research, as Germany's Space Agency DLR has been given responsibility by the federal government for the planning and implementation of the German space program. DLR is also the umbrella organization for the nation's largest project management agency.

Approximately 8000 people are employed at 16 locations in Germany: Cologne (headquarters), Augsburg, Berlin, Bonn, Braunschweig, Bremen, Göttingen, Hamburg, Jülich, Lampoldshausen, Neustrelitz, Oberpfaffenhofen, Stade, Stuttgart, Trauen and Weilheim. DLR has also offices in Brussels, Paris, Tokyo and Washington, D.C.

Remote Sensing Technology Institute
Institut für Methodik der Fernerkundung

DLR's Remote Sensing Technology Institute (IMF) is located in Oberpfaffenhofen, Berlin-Adlershof, Bremen and Neustrelitz.

IMF carries out research and development for retrieving geoinformation from remote sensing data. It conducts basic research on physical principles of remote sensing and develops algorithms, techniques, and operational processing systems for synthetic aperture radar, optical remote sensing, and spectrometric sounding of the atmosphere. The processing systems are in operational use for national, European, and international Earth observation missions.

For preparation and in support of space missions, IMF operates a suite of optical airborne sensors and laboratories. The institute contributes its expertise to novel sensor and mission concepts.

The German Remote Sensing Data Center (DFD) and IMF form DLR's Earth Observation Center (EOC).

**Deutsches Zentrum
für Luft- und Raumfahrt** e.V.
in der Helmholtz-Gemeinschaft

Institut für Methodik der Fernerkundung
Oberpfaffenhofen
82234 Weßling

www.dlr.de/eoc